

AD-A135 462

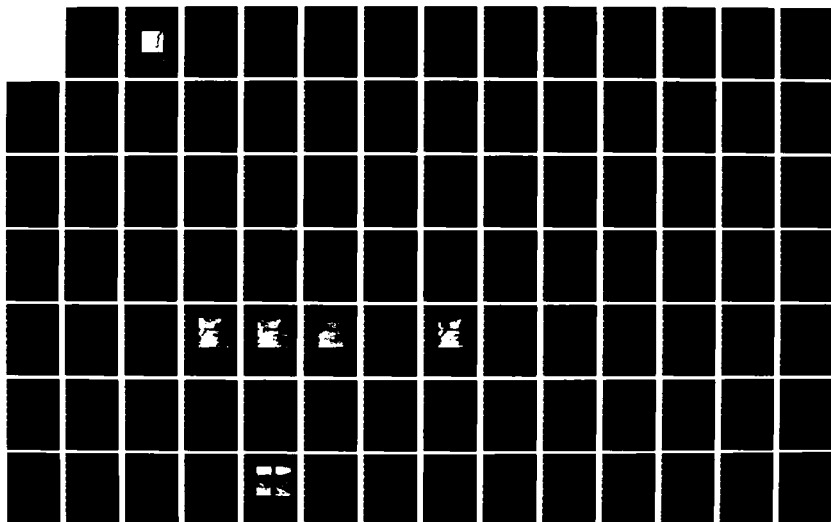
SWIRLS AND PLUMES OR APPLICATION OF STATISTICAL METHODS 1/3
TO SATELLITE-DERIVED (U) SCRIPPS INSTITUTION OF
OCEANOGRAPHY LA JOLLA CA K A KELLY AUG 83

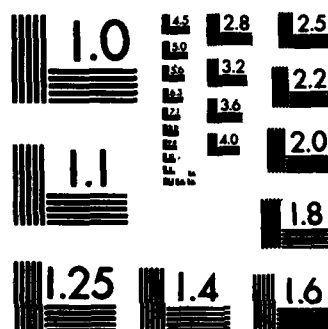
UNCLASSIFIED

SIO-REF-83-15 N00014-80-C-0440

F/G 8/10

NL





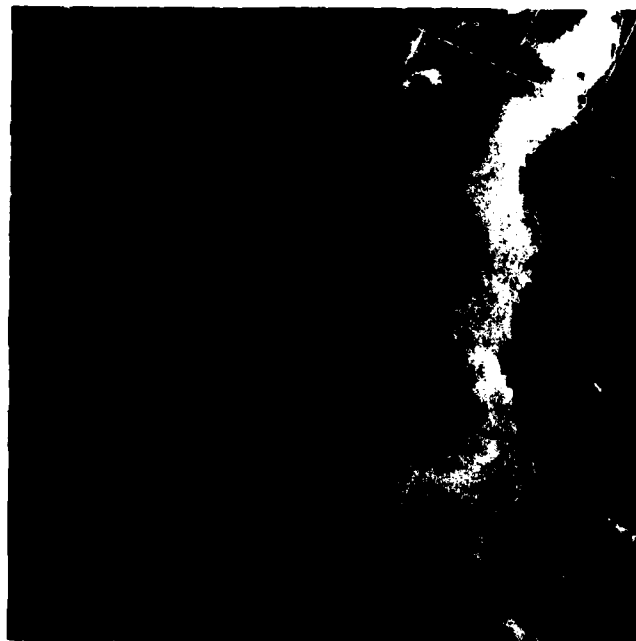
MICROCOPY RESOLUTION TEST CHART
NATIONAL BUREAU OF STANDARDS-1963-A

AD-A135462

(12)

SWIRLS AND PLUMES
OR
APPLICATION OF STATISTICAL METHODS TO
SATELLITE-DERIVED SEA SURFACE TEMPERATURES

Contract N00014-80-C-0440
University of California, San Diego



KATHRYN ANN KELLY

DTIC
S
DEC 07 1983
E

DTIC FILE COPY

CODE TECHNICAL REPORT NO. 18

SIO REFERENCE NO. 83-15

AUGUST 1983

This document has been approved
for public release and sale; its
distribution is unlimited.

83 00 19 00

UNIVERSITY OF CALIFORNIA

San Diego

Swirls and Plumes

or

Application of Statistical Methods to

Satellite-Derived Sea Surface Temperatures

A dissertation submitted in partial satisfaction of the

requirements for the degree Doctor of Philosophy

in Oceanography

by

Kathryn Ann Kelly

Committee in charge:

Professor Myrl C. Hendershott, Chairperson

Professor Russ E. Davis

Professor Clinton D. Winant

Professor Robert L. Parker

Professor Daniel B. Olfe

1983

The dissertation of Kathryn Ann Kelly is approved, and it is acceptable in quality and form for publication on microfilm:

Clinton D. Unwin
Daniel B. Olfe
James E. Domb
R. C. Parker
Myrl Henderson Chairperson
 University of California, San Diego

1983

Accession For	
NTIS GRA&I	<input checked="" type="checkbox"/>
DTIC TAB	<input type="checkbox"/>
Unannounced	<input type="checkbox"/>
Justification	<i>per</i>
By	
Distribution/	
Availability Codes	
Dist	Avail and/or Special
A-1	

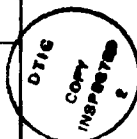


Table of Contents:

	Page
List of Figures	vi
List of Tables	xv
Glossary	xviii
Comments on the Notation	xix
Acknowledgments	xx
Vita, Publications and Fields of Study	xxii
Abstract	xxiii
I INTRODUCTION	1
1.1 The California Current	3
1.2 Shelf Circulation	7
1.3 Data from Weather Satellites	10
1.4 Coastal Ocean Dynamics Experiment	12
II DATA DESCRIPTION	16
2.1 Data Collection	16
2.2 Preliminary Processing	19
2.3 Sources of Error	20
2.4 Patchiness	22
III CLOUD DETECTION	26
3.1 The Effect of Clouds on the Data	26
3.2 Cloud Detection Methods	27
3.3 A Method for Flagging Cloud-Contaminated Data	28
3.4 Algorithm 1	30
3.5 Algorithm 2	31
IV CORRECTION FOR ATMOSPHERIC EFFECTS AND SYSTEMATIC ERRORS	38
4.1 Multi-channel Atmospheric Correction Theory	39
4.2 Noise Removal	43
4.3 Comparison of Satellite and Thermistor Data	45
4.4 Comparison of Consecutive SST Maps	49
4.5 Relating Map Errors to Point Errors	56
4.6 Using Maps to Study Atmospheric Correction	57
4.7 Conclusions	59
V SPATIAL AND TEMPORAL VARIABILITY	74
5.1 Problems in Defining Statistics	74
5.2 Reducing the Amount of Data	76
5.3 Decorrelation Time	78
5.4 Mean and Variance	80
5.5 Wavenumber Spectra	83

VI	COMPARISON OF SATELLITE IMAGES WITH OTHER CODE DATA;.....	93
6.1	Hydrographic Data	93
6.2	Current Meter Records	96
6.3	Doppler Log and Surface Drifters	98
VII	WINDS, TOPOGRAPHY AND SST;.....	106
7.1	Empirical Orthogonal Functions	108
7.2	Computing EOF's Using Singular Value Decomposition	109
7.3	Missing Data	111
7.4	SST Bias for Certain Wind Conditions	112
7.5	Computing SST EOF's by Separate Regions	113
7.6	Amplitudes for Partial Images	116
7.7	Misfit	118
7.8	EOF's for Wind and Sea-Level Height	119
7.9	The Empirical Modes for Winds, SST and SLH	120
7.10	The Time-Varying Amplitudes	125
7.11	Conclusions	130
VIII	VELOCITY ESTIMATION;.....	154
8.1	The Inverse Problem	155
8.2	Estimation Using a Simple Model	156
8.3	A Two-Step Method for Velocity Estimation	161
8.4	Velocity Estimates and Suggestions for Improving the Method	164
	REFERENCES	174
	APPENDIX A, EXAMPLE OF CLOUD FLAGGING PROCEDURE;.....	179
	APPENDIX B, REMOVING NOISE FROM CHANNEL 3;	188
	APPENDIX C, LEAST SQUARES ESTIMATION;.....	195
	APPENDIX D, INTERPOLATION OF IMAGES;.....	201
	APPENDIX E, COMPUTING EOF'S USING SVD;.....	207

List of Figures

	Page
Figure 1.1 Northern California Bathymetry	15
<p>The large square outlines the area covered by the satellite images which was much larger than the area covered by the CODE moored array and most of the other measurements.</p>	
Figure 2.1 Area Covered by a Typical NOAA-6 Pass	24
<p>The lines mark one-minute intervals on the region scanned in ten minutes on an ascending pass. The north-south line is the satellite's subtrack. The smaller region is the area covered in the CODE images.</p>	
Figure 2.2 Satellite Data Available for CODE-1 (1981)	25
<p>Each image is designated by its year day, calendar date and degree of cloud contamination. The numbers above certain images give their page numbers in the data report (Kelly, 1982).</p>	
Figure 3.1 Channel 3 of a Typical Image	33
<p>Light shades correspond to low temperatures and dark shades to high temperatures. The warm area along the right side of the image is the coastline of northern California. The light shades in the center and left parts of the image are clouds.</p>	
Figure 3.2 Channel 4 of the Image in Figure 3.1	34
<p>Same as Figure 3.1, except channel 4.</p>	
Figure 3.3 Channel 3 Minus Channel 4	35
<p>The difference of the images in Figures 3.1 and 3.2. There are no ocean features visible in the difference image. Clouds appear as very dark (warm) or very light (cold) areas.</p>	
Figure 3.4 Flow Chart for Cloud Detection	36
<p>Input, computations and output of the two algorithms.</p>	

Figure 3.5 Channel 4 Image with Cloud Mask	37
--	----

The mask computed with the cloud detection algorithms applied to the image in Figure 3.2. The masked areas are white.

Figure 4.1 Channel 3 Before and After Noise Removal	62
---	----

A portion of the image in Figure 3.1 is shown a) before the instrument noise was removed as described in Appendix B and b) after the noise was removed. The white area in the center of the figures is a cloud.

Figure 4.2 Comparison of Satellite and Thermistor SST	63
---	----

Temperatures from channel 3, channel 4 and in situ thermistors plotted versus the day of the observation. Symbols indicate the actual measurements and the data type (morning or evening). Measurements are connected by straight lines. Note the close correlation of channels 3 and 4.

Figure 4.3 Channel 4, Cos(Theta) and Wind Speed	64
---	----

For a series of images in July, mean channel 4 temperatures, the cosine of the satellite viewing angle and the wind speed are plotted versus the day of the observations. The viewing angle, θ , is defined in Figure 4.4. Note the correlation between mean temperature and the viewing angle.

Figure 4.4. Satellite Viewing Angle Geometry	65
--	----

The viewing geometry of the sun, the satellite and the region scanned is defined for a) evening and b) morning. The viewing angle, θ , is the angle between the satellite and a line normal to the surface and is positive in the figure. The angle, ϕ , defines the sun-satellite-sea surface geometry (after Bernstein, 1982).

Figure 5.1 Correlation and Variance for Image Pairs	86
---	----

To find the spatial resolution comparable to the fixed temporal resolution of 12 hours, several images were averaged over successively larger boxes. The variance of the images and the correlation between pairs of images is plotted against the box size. The correlation maximum at 10 pixels corresponds to the spatial resolution.

Figure 5.2 Structure Function for July Images 87

The spatially-averaged structure function for various time lags for two cases which bound the actual function. The case for which there is no variation in the mean gives the function only for temperature patterns changing in time. The other case allows the mean to change but also includes spatially-constant errors.

Figure 5.3 Mean Sea Surface Temperature 88

Computed by weighting more than fifty images which were grouped into 18 independent measurements based on a decorrelation time of four days. The coastline is shown in black. The mean was not computed for the white area at the left which had fewer than nine independent measurements. Values less than 8.5 C are white; values greater than 14 C are black. For locations refer to Figure 1.1.

Figure 5.4 Variance in Sea Surface Temperature 89

Computed as in Figure 5.3, after the mean was removed. Values less than 0.6 C² are white; values greater than 3.2 C² are black. The white area in the lower left corner has low variance; variance for the upper left corner was not computed. Note high variance regions at upper right (near Crescent City) and lower right (San Francisco Bay).

Figure 5.5 Mean and Variance in Cross-Shore Direction 90

Profiles of the a) mean and b) variance from Figures 5.3 and 5.4. Symbols denote profiles which have been averaged in the longshore direction. Solid lines are the profiles through the center of the CODE array. The CODE array had a typical temperature profile, but unusually low variance.

Figure 5.6 Longshore Wavenumber Spectra 91

One-dimensional spectra in the longshore direction for regions which were increasingly farther from the coast. Region A (adjacent to the coast) is plotted with the correct y-axis. Other plots are offset for clarity. The data used for the spectra were well-correlated making error estimates large. Error estimates are not shown.

Figure 5.7 Wavenumber Spectra for Pairs of Images	92
Spectra for images separated by six or seven days. Mean wind speeds for the second image in each case (dotted lines) were 50% greater than for the first image (solid line). Note the decrease in energy at high wavenumbers. Changes at low wavenumbers are not significant.	
Figure 6.1 CODE-1 Mooring Locations	101
Sites C1, C3, C5, M3 and R3 had current meters densely spaced in the vertical. Winds were recorded at sites C3, C5, R3 and S4. Thermistors used in the comparisons in Chapter 4 were located at C5, R3 and S4.	
Figure 6.2 Doppler Velocities and Satellite Image	102
Comparison of a) doppler acoustic log velocities computed by J. M. Kosro from measurements on days 116-118 with b) satellite image for the same area on day 117. The cross marks the tail of the velocity vector and the location of the measurement. The points in the coastline at the right are Pt. Arena and Pt. Reyes. Note the relatively large offshore velocities corresponding to the cold plume southwest of Pt. Arena.	
Figure 6.3 Doppler Velocities and Satellite Image	103
Comparison of a) doppler velocities from Kosro for days 141-143 with b) satellite image on day 140 for the same area. Note that the cyclonic eddy northwest of Pt. Arena evident in the velocities corresponds to a well-defined cold region which appears to have cyclonic rotation. A larger warm anti-cyclonic eddy southwest of Pt. Arena is paired with this cold eddy, but has a weaker temperature signature.	
Figure 6.4 Drifter Tracks and Satellite Image	104
Comparison of a) the trajectories of surface drifters tracked by R. E. Davis from release on day 122 to day 126 with b) the satellite image for the same area on day 121. Release locations are denoted by triangles. Locations were recorded about every six hours and are connected by straight lines. In successive images the warm area northwest of Pt. Arena contracted to form a single cold plume at the point. The single drifter which moved rapidly offshore was caught in this plume.	

Figure 6.5 Drifter Tracks and Satellite Image 105

Comparison of a) surface drifter tracks from Davis for days 185-189 with b) satellite image for the same area. Release locations for the drifters are denoted by triangles. The cold eddy northwest of Pt. Arena had a southward drift speed of about 10 km/day, which places it at the circular drifter track on the release day (185). Note that all drifters south of Pt. Arena were swept offshore in the cold plume north of Pt. Reyes, which is just visible at the right edge of the image. This plume extended about 250 km offshore.

Figure 7.1 Locations of Wind and SLH Measurements 133

In addition to wind measurements in the CODE array coastal winds and sea-level height measurements were collected at coastal stations from Crescent City to Point Conception.

Figure 7.2 Mean Wind Speed Vs. Variance 134

Images were biased toward certain wind conditions. A scatter plot of the mean and variance for a two-day period is shown in a) for the entire wind record (100 days) and in b) for each image. The symbols show how many pixels, out of a maximum of 8335, were cloud-free. Categories 1 and 3 were undersampled.

Figure 7.3 Misfit of Images to First Four EOF's 135

For each image the rms misfit to the first four EOF's is plotted against the fraction of the region which coincided with the cloud-free data. The symbols show whether the image was used as a base image, as a supplementary image in a composite, or not used for the EOF calculation. Only a few images, which were not used to compute the EOF's, had noticeably higher misfit.

Figure 7.4 Mean Wind Stress 136

For each location shown in Figure 7.1 the mean wind stress for the record was computed. The "+" gives the location of the measurement and the tail of the stress vector. The mean of each record was subtracted before the EOF's were computed.

Figure 7.5 Cumulative Variance in EOFs for All Variables	137
--	-----

For each EOF decomposition the cumulative percent of variance is plotted against the number of functions. For example, the first SST function for region C described 85 % of the total variance and the first two functions combined described about 90 % of the variance.

Figure 7.6a SST EOF 2 for Region A	138
--	-----

Second empirical orthogonal function of sea-surface temperature for part of the area shown in Figure 7.1. Light shades are negative (cold) anomalies and dark shades are positive (warm) anomalies. The medium gray area, which for reference has a value of zero, was not included in region A. The dark line at the right is the coastline.

Figure 7.6b SST EOF 3 for Region A	139
--	-----

Same as Figure 7.6a, except third function for region A.

Figure 7.6c SST EOF 2 for Region B	140
--	-----

Same as Figure 7.6a, except second function for region B.

Figure 7.6d SST EOF 3 for Region B	141
--	-----

Same as Figure 7.6a, except third function for region B.

Figure 7.6e SST EOF 2 for Region C	142
--	-----

Same as Figure 7.6a, except second function for region C.

Figure 7.6f SST EOF 1 for Regions A, B and C	143
--	-----

Same as Figure 7.6a, except first function for combined regions A, B and C.

Figure 7.6g SST EOF 2 for Regions A, B and C	144
--	-----

Same as Figure 7.6a, except second function for combined regions A, B and C.

Figure 7.7 Wind EOF's 1 - 4	145
-----------------------------------	-----

Empirical orthogonal functions for wind stress for the locations shown in Figure 7.1. The horizontal direction has been expanded to make the individual vectors visible. The "+" marks the location of the stress anomaly and the tail of the vector.

Figure 7.8 Sea Level Height, Mean and EOF's 1 - 3	146
---	-----

Mean and empirical orthogonal functions of coastal sea level from tide gauges at locations shown in Figure 7.1. The triangle marks the mean value or anomaly at the gauge location, which is identified by its latitude. The mean was removed before the EOF's were computed.

Figure 7.9a Amplitudes for SST EOF 1	147
--	-----

Time-varying amplitudes for the first sea-surface temperature EOF for each region and the combined regions. The triangles denote computed amplitudes for images which covered at least half of the region. Region A amplitudes are shown with the correct y-axis; other amplitudes are offset for clarity. Positive amplitudes give the positive and negative anomalies as described in Figure 7.6. Negative amplitudes reverse the signs of the anomalies.

Figure 7.9b Amplitudes for SST EOF 2	148
--	-----

Same as Figure 7.9a, except for second EOF.

Figure 7.9c Amplitudes for SST EOF 3	149
--	-----

Same as Figure 7.9a, except for third EOF.

Figure 7.10 Amplitudes for Wind EOF's 1 - 4	150
---	-----

Time-varying amplitudes for the wind stress EOF's. The amplitudes for the first function are shown with the correct y-axis; other amplitudes are offset for clarity. Positive amplitudes give the wind stress anomalies as shown in Figure 7.7; negative amplitudes reverse the vectors. For example, a positive amplitude for the first function gives wind stress anomalies toward the southeast. A negative amplitude gives wind stress anomalies toward the northwest.

Figure 7.11 Amplitudes for SLH EOF's 1 - 3	151
--	-----

Time-varying amplitudes for sea-level height EOF's.
The amplitudes for the first function are plotted with the correct y-axis; others are offset for clarity. Positive amplitudes give the anomalies with the sense shown in Figure 7.8. Negative amplitudes reverse the sign of the anomaly.

Figure 8.1 Image Used for Velocity Estimates	169
--	-----

The SST map for day 189 from which the gradient of temperature was computed. The difference between this map and a map for 12 hours later was used to approximate the derivative of temperature with respect to time.

Figure 8.2 Displacement of Small Features	170
---	-----

Several small features could be followed from the first image to the second image. The "+" marks the location of a feature in the first image and is the tail of the displacement vector.

Figure 8.3 Cross-Isotherm Velocity	171
--	-----

From the conservation of temperature equation, cross-isotherm velocities were computed. The "+" marks the location of the computed velocity and the tail of the velocity vector. Maximum velocities were about 5 cm/s. The weights for the equations, as described in the text, were $w_1=1$ and $w_3=1$.

Figure 8.4 Effect of Stronger Boundary Condition	172
--	-----

Same as Figure 8.3, except with larger weight for the boundary condition ($w_3=100$). Note that the velocities at the coastline are either zero or parallel to the edge.

Figure 8.5 Total Velocity Field	173
---------------------------------------	-----

Velocity estimate which includes components both parallel and perpendicular to the isotherms. The three equations used to compute the estimate were equally-weighted: $w_1=1$, $w_2=1$, $w_3=1$, as described in the text. Maximum velocities were about 40 cm/s. Agreement with doppler-log velocities was good except near the coast.

Figure A.1 Coded Mask from Algorithm 1	183
Coded cloud mask for the image in Figure 3.2. The 0's on the right are from the land mask. Codes 4, 5 and 6 represent clear ocean areas. Coding system is described in the text.	
Figure A.2 Rough Mask from Algorithm 1	184
The clear ocean codes (4, 5 and 6) in Figure A.1 were changed to 1's. All other codes, which were not already 0, were changed to 0. Only subsets corresponding to 1's were examined by Algorithm 2.	
Figure A.3 Mean Channel 4 Temperatures	185
Subset mean temperature as a function of distance from the left side of the mask. The temperatures for the three triangles, which define a parabola just below the cluster of mean values, were input variables for Algorithm 2.	
Figure A.4 Edited Mask from Algorithm 2	186
The code 9 indicates subsets which were classified as clouds by Algorithm 2. Codes 2-8 are subsets which could not be classified automatically; their validity must be determined by the operator. The codes are described in the text.	
Figure B.1 Channel 3 Noise Removal	194
One dimensional illustration of the noise removal technique discussed in the text. The difference of the channels is clipped to reduce contributions from clouds before it is high-passed to isolate the noise signal.	

List of Tables

	Page
Table 4.1 Predictive Skill for CODE Data	66
<p>Skill of each channel separately and together for predicting the thermistor temperatures in the CODE array. The variable must contribute more to the prediction skill than the artificial skill for the variable to be a good predictor. The addition of channel 3 to the prediction using channel 4 alone is not significant because the additional prediction skill is only half the additional artificial skill. Channel 3 has some predictive skill because it is well-correlated with channel 4: the correlation coefficient is 0.67.</p>	
Table 4.2 Predictive Skill for Bernstein's Data	67
<p>Skill of each channel separately and together for predicting the <u>in situ</u> temperatures in Bernstein's data. The addition of channel 4 to the prediction using channel 3 alone is not significant because the additional prediction skill is much less than the additional artificial skill. Channel 4 has some predictive skill because it is well-correlated with channel 3: the correlation coefficient is 0.96. Note that the variance in the sea-surface temperatures to be predicted, T_s, is much larger for Bernstein's data than for the CODE data, as shown in Table 4.1.</p>	
Table 4.3 Mean Differences for Image Pairs	68
<p>Differences in the mean value for each channel between the images whose year days are given in the first two columns. Images followed by an A are morning data. The days are based on GMT so that, e.g., image 127 precedes image 127A. The mean difference was computed over the common clear area; the size of the common area is given in pixels. Each pixel is approximately 1 km^2.</p>	
Table 4.4 Statistics of Image Differences	69
<p>The mean differences in Table 4.3 were grouped according to the type of data, morning or evening, and mean values for the mean differences were computed for each channel. Note that the mean difference between pairs is larger for channel 3 than for channel 4 for all data types.</p>	

Table 4.5 Distance of Image from Satellite Subtrack	70
---	----

For each image, designated by its year day, the approximate distance of the center of the image from the satellite subtrack is shown in degrees longitude, east or west of the subtrack. The viewing angle, θ , is defined in Figure 4.4. Channel 3 of many images recorded in the morning had a hazy appearance with no recognizable ocean features, while the channel 4 image was relatively cloud-free. Note that the morning images which were hazy correspond to a negative viewing angle, or the CODE region was to the east of the subtrack, the sun side, as shown in Figure 4.4.

Table 4.6 Estimation of Time-Varying Means Using Powers of the Viewing Angle	72
--	----

Variations in the mean temperature of each channel with changes in the viewing angle, θ , were regressed against powers of the viewing angle. The results are shown as estimation skill for each power of θ . The pair of estimators with the highest individual skill were tested together for skill. No pair of estimators showed a significant increase in skill over the best individual estimator.

Table 4.7 Effect of Viewing-Angle Corrections on Estimation Skill for Point Measurements	73
--	----

Estimation skill for channels 3 and 4 for predicting thermistor temperatures, with and without viewing-angle corrections. The total artificial skill for each estimator is shown for comparison with the computed skill; the artificial skill includes a term for the viewing-angle corrections, where the corrections were used. Conclusions are discussed in the text.

Table 7.1 Wind Bias Statistics	152
--------------------------------------	-----

Wind conditions for each day in representative wind records were defined by their mean and variance over the previous two days. A comparison of the percentage of days in each category with the percentage of images in each category shows that the images are biased toward categories 2 and 4. The number of images in each category is also shown.

Table 7.2 Statistics of Spatial Regions for EOF's	153
---	-----

The sea surface temperature EOF's were computed over three non-overlapping spatial regions. The number of points in each region and the number of images from each wind category (defined by Table 7.1) is shown for each region.

Table A.1	187
-----------------	-----

Variable names and definitions for the two cloud-detection algorithms. Those variables designated fixed (F) retained the same value for all the images; those which varied (V) had different values for each image. The values listed are those used in the example described in the text and in the figures. All values and data were in hundredths of a degree C. because the data were stored as integers.

Glossary

AVHRR	Advanced Very High Resolution Radiometer
CalCOFI	California Cooperative Oceanic Fisheries Investigation
channel 3	The 3.7 μm channel of the AVHRR
channel 4	The 11 μm channel of the AVHRR
CZCS	Coastal Zone Color Scanner
CODE	Coastal Ocean Dynamics Experiment
CZCS	Coastal Zone Color Scanner
EOF	Empirical orthogonal function
ephemeris	The parameters which define the orbit of a satellite
NEDT	Noise equivalent differential temperature
NESS	National Environmental Satellite Service, a division of NOAA
NDBO	National Data Buoy Office
NOAA	National Oceanic and Atmospheric Administration
NOAA-6	One of a series of NOAA operational weather satellites
pixel	An element of an array which is displayed as an image
rms	root mean square
scatterometer	An instrument which uses radio frequencies to measure wind vectors
SLH	Sea-level height
SSOF	Scripps Satellite Oceanography Facility
SST	Sea surface temperature
SVD	Singular value decomposition
T-S	Temperature-salinity

COMMENTS ON THE NOTATION

Vector and matrix notation are used throughout the text in place of the usual summation or component notation. I find that matrix algebra, by hiding the details of the operations, clarifies the relationships between variables. To assist the reader in following the discussion, Appendices C, D and E contain the essential equations of basic statistical methods, written in vector notation. The original source of the equations, which uses summation notation, is referenced in each appendix. I hope the reader will appreciate the simplicity of the matrix algebra.

The following notation is generally followed:

- A capital letters for matrices
- x underlined letters for (column) vectors
- x^T transpose of a vector (or matrix)
- α Greek letters for scalars or coefficients

ACKNOWLEDGMENTS

The types of assistance I received in my research were as numerous as the contributors. I regret that I cannot name everyone who encouraged me, directed my research or just listened to my problems.

My first thanks go to my advisor, Myrl Hendershott, who ignored the prevailing arguments about skin depth for the AVHRR because the patterns in the satellite images looked real. He endured numerous committee meetings for my benefit, while helping me to get back on the track when my countless computer programs threatened to displace science in my research.

The only way I know to describe Russ Davis' assistance is to say he taught me to think. He helped me derive methods from first principles; numerous paragraphs should reference "(R. E. Davis, personal communication)."

Clinton Winant first suggested that I look at satellite data for CODE and he was my link with that exciting project.

Bob Parker was an inspiration primarily through the classes he taught. I borrowed both Bob's notation and his subroutines.

The sheer volume of data would have precluded this research if it were not for the assistance of Freeman Gilbert at a critical moment. He taught me to think in megabytes.

My husband, Peter Shaw, who should be both first and last in this list, helped me in ways too numerous and personal to mention here. He deserves a gold star for writing the subroutine to display gray shades on the minicomputer we used. The figures in this thesis would have been impossible without that subroutine and without PLOTXY, an incredibly user-friendly plotting package written by my good friend, Loren Shure, and Bob Parker. Thanks also to Paul Henkart for programming assistance on several occasions.

I am grateful to my family and my friends who always knew I could make it, even when I didn't. Special credit is due the supervisor of the shop where I worked before I finished my undergraduate degree, for telling me to go back to school, and to Jorg Imberger for refusing to accept my arguments for not getting a Ph. D.

Many friends among the students and faculty at Scripps encouraged me in this work. I would especially like to thank all the women who have chosen to study oceanography and geophysics for making it easier to be a woman in science.

This research was supported by the Office of Naval Research, Coastal Sciences Division, through contract N00014-75-C-300 with the University of California, San Diego; I appreciate their continuing

interest in the analysis of satellite data. Satellite images were collected and partially processed at the Scripps Satellite Oceanography Facility, which was supported by the Office of Naval Research, Ocean Sciences Division, through contract N00014-80-C-0440 and by the National Science Foundation, through grant NSF/OCE78-19888.)

VITA

January 14, 1948 - Born - Buffalo, New York

1977 - B.S., University of California, Berkeley
1977-1978 - Assistant Engineer, Brown Caldwell, Walnut
Creek, California
1978-1983 - Research Assistant, Department of Scripps
Institution of Oceanography,
University of California, San Diego
1983 - Doctor of Philosophy
University of California, San Diego
1983 - Green Scholar, Institute of Geophysics and
Planetary Physics, La Jolla, California

PUBLICATIONS

"Infrared Satellite Data from the First Coastal Ocean Dynamics Experiment: March-July 1981," Scripps Inst. of Oceanogr., Ref. 82-15, La Jolla, Ca., 1982.

FIELDS OF STUDY

Major Field: Oceanography

Studies in Dynamical Oceanography
Professor Richard L. Salmon

Studies in Linear and Non-linear Waves
Professors Myrl C. Hendershott,
John W. Miles, and Robert T. Guza

Studies in Observational Methods
Professor Russ E. Davis

Studies in Applied Mathematics
Professor Sinai Rand

Studies in Numerical Methods
Professor Robert L. Parker

Studies in Dynamic Meteorology
Professor Richard C. J. Somerville

ABSTRACT OF THE DISSERTATION

Swirls and Plumes

or

**Application of Statistical Methods to
Satellite-Derived Sea Surface Temperatures**

by

Kathryn Ann Kelly

Doctor of Philosophy in Oceanography

University of California, San Diego, 1983

Professor Myrl C. Hendershott, Chairperson

Satellite images, with their large areal coverage at short sampling interval, bridge the spatial and temporal gap between hydrographic surveys and moored instruments. However, calibration problems, cloud contamination, the large quantity of data and difficulty in obtaining satellite data have frequently limited its use to only qualitative or semi-quantitative descriptions of surface properties. The acquisition of a satellite receiving station at Scripps Institution of Oceanography, combined with an intensive experiment (Coastal Ocean Dynamics Experiment) created the opportunity to analyze a series of infrared images of the California Current. Fifty-eight images were collected during an exceptionally-clear four month period in 1981, coincident with other measurements on the shelf and slope from current meters, hydrography, surface drifters, doppler acoustic log, wind recorders and tide gauges. The goals of the analysis were to develop a method for removing unusable

data and systematic errors, to extract a quantitative description of SST patterns off northern California, to compare the satellite sea-surface temperatures with in situ measurements, to investigate the relationship between SST, wind and topography, and to estimate surface velocities from a series of images.

The images were first converted to a series of SST maps. The nearly-automatic method developed for flagging land and cloud-contaminated portions of an image was based on a comparison of the two infrared channels and on the statistical properties of subsets of the image. Satellite-derived SST's were compared point-by-point with in situ temperatures and from image-to-image to check for errors. The largest source of error for the $11\mu\text{m}$ channel came from the viewing geometry of the satellite with respect to the sea surface; errors for the $3.7\mu\text{m}$ channel were correlated with the sun angle. Viewing geometry errors accounted for 50 % of the variance between successive images. Both comparisons of point measurements and of entire images showed that two channels did not give significantly better SST's than a single channel. The SST maps from the $11\mu\text{m}$ channel, after correction for viewing geometry, showed a mean temperature change of 2°C . within two weeks; mean temperature changes over a slightly longer interval agreed well with the changes in temperatures from the hydrographic surveys.

The relationship between SST's, wind and topography was investigated using empirical orthogonal functions (EOF's). Both the mean SST and the third mode (in order of variance) reflected the complicated coastline, slope and shelf topography, but not that of the deep ocean. The second mode had a predominately longshore structure which was nearly

duplicated in the second wind mode; comparison of the time-varying amplitudes showed the SST mode to be locally-generated coastal upwelling. The appearance of cold areas near capes was correlated with the strength of upwelling-favorable winds. There was evidence that spatial variations in wind strength may cause cold water to separate from the coast in plumes as strong winds gradually cease.

The close relationship between SST patterns and near-surface velocities suggested a simple model for computing quantitative velocity estimates from satellite data alone, based on the thermal wind relationship and the conservation of temperature. For the CODE case of strong winds and barotropic current fluctuations, the model was in good agreement with velocities computed from the doppler-log. This analysis suggested that, for regions with a simple temperature-salinity relationship and for which surface temperature gradients extend deep into the water column, reasonable surface velocity maps can be computed from satellite data. The accuracy of the estimates could be both verified and improved by using concurrent in situ measurements.

CHAPTER 1

INTRODUCTION

The California Current System has been studied extensively on two different temporal and spatial scales. This separation is due as much to the difficulty in obtaining data over widely-varying scales as to the belief that these scales have different governing dynamics. Large-scale studies of the California Current have been based primarily on data collected from ships; the resolution in time is limited by how long it takes a ship to travel from one sampling station to the next and the time between ship surveys. The resolution in space is limited by practical considerations: ship time is expensive and the numerous measurements taken at each station are time-consuming. Instruments which make "continuous" measurements while the ship is moving greatly improve the spatial resolution along the ship track, although the time elapsed between measurements taken at a given distance is still the same. These ship-based surveys, particularly those conducted by the California Cooperative Fisheries Investigation (CalCOFI), are the basis of most of what is known about seasonal and mean properties of the California Current beyond the continental shelf.

At smaller spatial scales and shorter temporal scales the currents on the continental shelf have been studied primarily using moored current meters. The shelf on the west coast of North America is narrow; off northern California it is only 15-20 km wide. Recent advances in current meter design have made velocity measurements quite accurate even in the presence of substantial wave motion. Because of the difficulty and expense of maintaining each mooring most experiments

have consisted of a few moorings, confined to the shelf and inner slope, which were maintained for periods of several months. Analyses of these measurements have focused on the 'event scale,' which is coincident with an atmospheric event of a few days or more duration, or on seasonal transitions (e.g., Huyer, Sobey and Smith, 1979). Questions of spatial variability cannot be answered with so few measurements so models of shelf dynamics have usually assumed a predominately two-dimensional flow in the vertical and cross-shore directions where the largest velocities are longshore.

The continental slope marks a physical as well as conceptual boundary between deep ocean and shelf models. Varying topography of the slope creates problems for either regime. All models begin with the momentum and continuity equations which are

$$\underline{u}_t + \underline{u} \cdot \bar{\nabla} \underline{u} + 2 \, \underline{\Omega} \times \underline{u} = -\frac{\bar{\nabla} p}{\rho} + \nu \bar{\nabla}^2 \underline{u} \quad (1.1)$$

$$\bar{\nabla} \cdot \underline{u} = 0 \quad (1.2)$$

Nearly all models neglect the second term in 1.1, the advection term, and use scaling arguments to show that w is small where

$$\underline{u} = (u, v, w)$$

Further simplifications include vertically integrating 1.1 to obtain a transport equation on either the shelf or in deep water, neglecting the time derivative for long temporal scales, assuming different balances

for the u and v directions on the shelf, and in the deep ocean taking the curl of the momentum equation to obtain a vorticity equation. The relationship between the deep ocean and the boundary has been more a source of speculation than a subject for measurement or simulation, undoubtedly because of the different scales and models of interest.

In the last decade satellite measurements of the ocean have become available to oceanographers. The satellite data cover a large area with good spatial resolution in a few minutes; however, they only measure surface quantities. The only satellite-derived measurements consistently recorded at present are the visible and infrared images from the NOAA weather satellites and the visible images from the aging Coastal Zone Color Scanner (CZCS), which is carried by the satellite NIMBUS-7. Other measurements which can be made from satellites include wind vectors using a scatterometer and sea-level using an altimeter. A discussion of the types of measurements that can be made with satellites and the instruments used to make them is contained in the notes by Stewart (1983). At present there are no data with comparable time and space scales with which to compare the NOAA images or the CZCS images.

1.1 The California Current

CalCOFI has intensely sampled the same grid for more than 30 years with an emphasis on those water properties affecting the fishing industry. From these measurements maps of various properties have been constructed and maps of dynamic height have been computed (Wyllie, 1966). These maps have numerous meanders and occasionally features which are clearly eddies, but frequently at the resolution of the grid

spacing. These measurements are used to determine seasonal and interannual variability on spatial scales of 100 km or larger.

Hickey reviewed the data available for the California Current System to find seasonal variations and their possible causes (1979), her results with respect to the California Current off northern California are summarized here. If the time-derivative of velocity and the nonlinear terms are neglected, the curl of equation 1.1 is taken, and the resulting vorticity equation is integrated vertically, one obtains the Sverdrup balance

$$M_y = -\frac{1}{\beta} \left(\frac{\partial \tau^x}{\partial y} - \frac{\partial \tau^y}{\partial x} \right) = -\frac{1}{\beta} (\underline{k} \cdot \text{curl } \underline{\tau}) \quad (1.3)$$

where the following relationships were used to derive 1.3:

$$\underline{\tau} = \rho \nu \frac{\partial \underline{u}}{\partial z} \quad (1.4)$$

where $\underline{\tau}$ is the wind stress at the surface, ν is the dynamic vertical eddy diffusivity,

$$\beta = \frac{\partial f}{\partial y}$$

where f is the Coriolis parameter

$$f = 2 \Omega \sin \phi \quad (1.5)$$

and ϕ is the latitude, and M_y is the poleward mass transport

$$M_y = \int_{-D}^0 \rho v dz \quad (1.6)$$

Hickey concluded that the balance in 1.3 between mass transport and the curl of the wind stress held for the California Current beyond the shelf. She surmised that the California Current has three southward maxima: a nearshore maximum driven by the longshore component of wind stress and two offshore maxima, which are driven by the curl of the wind stress. The nearshore maximum is strongest during the spring and early summer, while the offshore region is strongest during the late summer and early fall. In the vicinity of Cape Mendocino one offshore maximum is about 400 km offshore and the other about 800 km offshore (see Figure 1.1). Hickey suggested that large-scale flow separation in the vicinity of headlands may be responsible for anomalous countercurrents in the late summer and fall, south of 40° N. Hickey pointed out that the coastline topography may determine the local curl of the wind stress and may also be responsible for countercurrents, but that it would be difficult to separate these effects. Hickey concluded that there is a nearshore northward mean flow south of Cape Mendocino which is particularly strong near San Francisco Bay and which may be related to the positive curl τ near the coast.

Chelton (1980) studied the relationship between low frequency sea-level variability and sea-level pressure in the California Current using statistical methods. From tide gauge measurements he found that sea level height (SLH) was dominated by variations with periods longer than a year and found evidence of northward propagation of SLH anomalies at phase speeds of about 50 cm s⁻¹. At periods of less than one year

variations in SLH were forced directly by atmospheric pressure: SLH responded rapidly to direct pressure forcing and slowly (2-3 months) to pressure in the form of geostrophic winds over the entire North Pacific. Chelton found that local longshore wind stress was important only from Washington to northern California. A SLH mode which could not be explained by sea level pressure was a simple longshore trend in SLH with a node between Crescent City and San Francisco (see Figure 1.1).

Chelton used the CalCOFI data to investigate quasi-geostrophic currents as a source of SLH variability. Sea-level height computed by vertically integrating density profiles is known as steric height. Chelton found that most of the variability in steric height was in the upper 200 m of the ocean and that measurements from the surface relative to 500 m depth could quantify it. Local winds can generate SLH variations by two different mechanisms; in both cases the Coriolis term in equation 1.1 forces a transport of the surface water to the right of the wind (in the northern hemisphere). By the first mechanism, a positive wind stress curl forces a surface Ekman divergence, lowering sea level; (cold) water from below the surface is pumped up to replace the surface water. The second mechanism, coastal upwelling, can occur only at a boundary, but does not require a wind stress curl. Longshore winds cause a divergence or convergence of surface water at the coastal boundary which causes a cross-shore slope of the sea surface. Near the boundary water moves vertically causing density surfaces to tilt. In coastal upwelling the sea surface tilts down toward the coast and density surfaces tilt up as cold water moves to the surface; conversely in downwelling, water piles up, causing higher sea level and warmer water

near the coast. Scaling arguments suggest that the longshore wind stress, which is responsible for coastal upwelling, is more important than the curl of the wind stress in the coastal region; but it is not clear how wide this region is. Chelton's analysis showed that the dominant mode of steric height was an onshore/offshore flow reversal at about 100 km from the coast; which coincided with the location of maximum curl of the wind stress; this mode resembled the expected response to the wind stress curl from the Ekman pumping model. He found a steric height mode which resembled coastal upwelling, but found no steric height response to local winds. Chelton found that the coastal upwelling mode was incoherent on scales larger than 200 km and he concluded that, because the grid spacing for the winds exceeded this length scale, he was unable to resolve this response.

1.2 Shelf Circulation

On much smaller scales numerous experiments have been conducted to study the shelf circulation off Oregon and California. Current meters on a few moorings have been used to obtain long time series of currents inside the shelf break. From these observations some simple models of shelf dynamics have evolved which are summarized in the review paper by Winant (1980) and are presented here briefly. Motions at periods longer than tides and shorter than a month are generally forced by the atmosphere. On the larger spatial scales and time scales of a month or more, wind could be expected to contribute to the vorticity of the water column as shown in equation 1.3; on time scales of days there would be important contributions to the momentum of the water by direct

wind forcing. The shelf acts as a boundary layer for the deeper ocean and could also be forced by eddies or currents. A third driving force is the runoff of large river systems as discussed by Hendershott and Rizzoli (1976) for the Adriatic. Northern California has several rivers which drain into the California Current, the largest of these is the combined outflow of the Sacramento and San Joaquin Rivers out of the San Francisco Bay.

Starting with equations 1.1 and 1.2, and neglecting the non-linear advection term, vertical stresses, horizontal gradients of the stress vector, $\underline{\tau}$, and variations in the Coriolis parameter, f , Winant obtains

$$u_t - fv = -\frac{p_x}{\rho} + \frac{\tau_z^x}{\rho} \quad (1.7a)$$

$$v_t + fu = -\frac{p_y}{\rho} + \frac{\tau_z^y}{\rho} \quad (1.7b)$$

$$w_t = -\frac{p_z}{\rho} - g \quad (1.7c)$$

where the equation has been written in components. These equations can be integrated from the bottom to the surface to produce mass transport equations for the shelf

$$U_t - fV = -H^{-1} \int_0^H \frac{p_x}{\rho} dz + \frac{(\tau_s^x - \tau_b^x)}{\rho H} \quad (1.8a)$$

$$V_t + fU = -H^{-1} \int_0^H \frac{p_y}{\rho} dz + \frac{(\tau_s^y - \tau_b^y)}{\rho H} \quad (1.8b)$$

where

$$U, V = \int_0^H \frac{u, v}{H} dz$$

The presence of the coastal boundary imposes different dynamics in the longshore and cross-shore directions. The basis for different dynamics can be seen in several ways. Measured longshore velocities, v , are much larger than cross-shore velocities; the geometry of the narrow shelf suggests a different balance because the time required to adjust to forcing is proportional to the length scales. One model, described by Winant, suggests that cross-shore accelerations are small, that the cross-shelf momentum equation, 1.7a, is in geostrophic balance (i.e., the second term balances the third), and that the longshore equation, 1.7b, is a balance between local wind stress, longshore pressure gradient and longshore acceleration.

Another possible explanation for motion on the shelf is the "continental shelf wave," which is discussed in the review paper by Allen (1980). The shelf wave is a long, free wave generated non-locally for which the shelf acts as a wave guide. For a long straight shelf one could expect linear waves to propagate long distances, provided non-linear terms are small. In the presence of numerous capes and canyons, however, the meanings of longshore and cross-shore lose significance.

Even for a stretch of straight coastline, nearby capes may influence shelf motions through a longshore pressure gradient, a disruption of predominately longshore winds, strong cross-shore velocities or large vertical velocities due to intense upwelling. As Winant observed, if local winds can account for most of the measured currents, then there is no clear evidence for the presence of such waves. In addition, if the current field is dominated by topographic effects, then long, linear waves will not propagate far. The limited spatial coverage of current meter observations has not permitted an analysis of the effect of topography on nearby currents.

1.3 Data from Weather Satellites

Although weather satellites were designed to collect images for weather prediction, to estimate cloud cover and winds and to follow storms, the TIROS-N series of NOAA satellites carry an infrared radiometer which can detect variations in temperature of 0.1° C. A large set of infrared images is available from the TIROS-N series of NOAA weather satellites. In the form of sea-surface temperature maps, these images are well-suited for analyses of spatial variability, for supplementing in situ measurements in space and time, and for studying areas in which few conventional measurements are available.

R. V. Legeckis of NOAA has long exploited the advantages of the satellite data: the nearly-instantaneous coverage of a large area and the long series of images. Legeckis has conducted several studies using the infrared images, including a study of the seaward deflection of the Gulf Stream (1979), using successive images to follow waves along the

Gulf Stream and to study the statistics of the location of the strong frontal boundary.

A study of the California Current off Point Conception by R. L. Bernstein established that the SST patterns recorded by the satellite radiometer corresponded to the meanders observed on a CalCOFI survey (Bernstein, Breaker and Whritner, 1977). The evolution of a large warm intrusion was followed over a month, ship surveys and air expendable bathythermographs (AXBT) showed evidence of the intrusion at depths of up to 250 m below the surface. Bernstein, et al., suggested that satellite data could supplement the CalCOFI surveys whose 80 km grid spacing and one-month sampling intervals were inadequate to resolve synoptic events. Bernstein was instrumental in establishing the Scripps Satellite Oceanography Facility (SSOF) which opened in 1979.

In the California Current both the infrared and the visible images show high variability over the continental slope. Temperature features extend from the coast at right angles to the mean currents into the deep ocean with apparent disregard for annual mean flows or for assumptions about longshore variability or rapid depth changes. Because of the mismatch of sampling scales between satellite images and other measured quantities the dynamics of these features are difficult to analyze. The problem is further complicated by the nature of the measured quantity, infrared radiance, which at best can only yield sea-surface temperature (SST). Temperature appears in equation 1.1 only through its implicit relationship to density.

1.4 Coastal Ocean Dynamics Experiment

The Coastal Ocean Dynamics Experiment (CODE) was a two-year experiment designed to study the response of the shelf to wind stress. CODE was conducted jointly by scientists from Scripps Institution of Oceanography, Woods Hole Oceanographic Institution, Oregon State University, and the University of New Hampshire. One of the purposes of CODE was to estimate the sizes of the terms in equation 1.1 based on measurements. A site in northern California was selected for its strong winds and simple topography. The CODE site is shown in Figure 1.1 along with the bathymetry of northern California. Central to the experiment was a large array of current meters and several hydrographic surveys. Other measurements included winds within the array, bottom pressure, doppler-log velocities, surface drifters, wind measurements and SST from aircraft, CODAR surface velocities and SST from satellite. To check for the influence of non-local events some measurements were taken at coastal stations from Crescent City to Point Conception.

My responsibility in this experiment was the collection, processing and analysis of infrared images from the satellite NOAA-6 during the first year of CODE. The relationship between the areal coverage of the satellite data and the CODE array is shown in Figure 1.1. The goals of the study described here were to treat the images as a time-series of measurements, to extract a quantitative description of the California Current off northern California, to examine the relationship between the SST patterns and in situ measurements to see how well the satellite images can interpolate and extrapolate from measurements over a smaller region, and to investigate the relationship between the temperature

patterns, wind and topography.

Calibration problems, cloud contamination, data availability and the large quantity of data involved have frequently limited the use of satellite data to qualitative or semi-quantitative descriptions, such as the statistics of the location of fronts. To convert the images to maps of sea surface temperature, I removed the cloud-contaminated data and attempted to calibrate the images by removing systematic errors. The processing steps required to convert the infrared images to temperature maps included 1) geometric correction of the image for viewing angle distortion, 2) conversion of infrared radiance to brightness temperature, 3) registration of the image to a specified grid, 4) flagging of invalid data (clouds and land) and 5) correction for systematic errors. The first three steps are discussed briefly in Chapter 2, along with a description of the data. Step 4 is outlined in Chapter 3 and in Appendix A. Step 5 is discussed along with atmospheric correction in Chapter 4.

The remaining chapters contain the actual analyses of the data and the comparisons with other data from CODE. Chapter 5 discusses the spatial and temporal variability of the SST patterns. In Chapter 6 a comparison with the in situ data shows the satellite maps described the surface temperature field well and that, at least for this experiment, they also described the variability in the surface velocity field. In Chapter 7 the maps are analyzed using empirical orthogonal functions, these functions and their amplitudes are compared with winds and topography to show that local winds force the patterns, whose shapes are determined by the shape of the coastline. Using the close relationship

between the SST maps and the surface velocity field shown in Chapter 6, a simple model was derived in Chapter 8 to estimate surface velocities using consecutive satellite images. The results were compared with in situ velocity measurements.

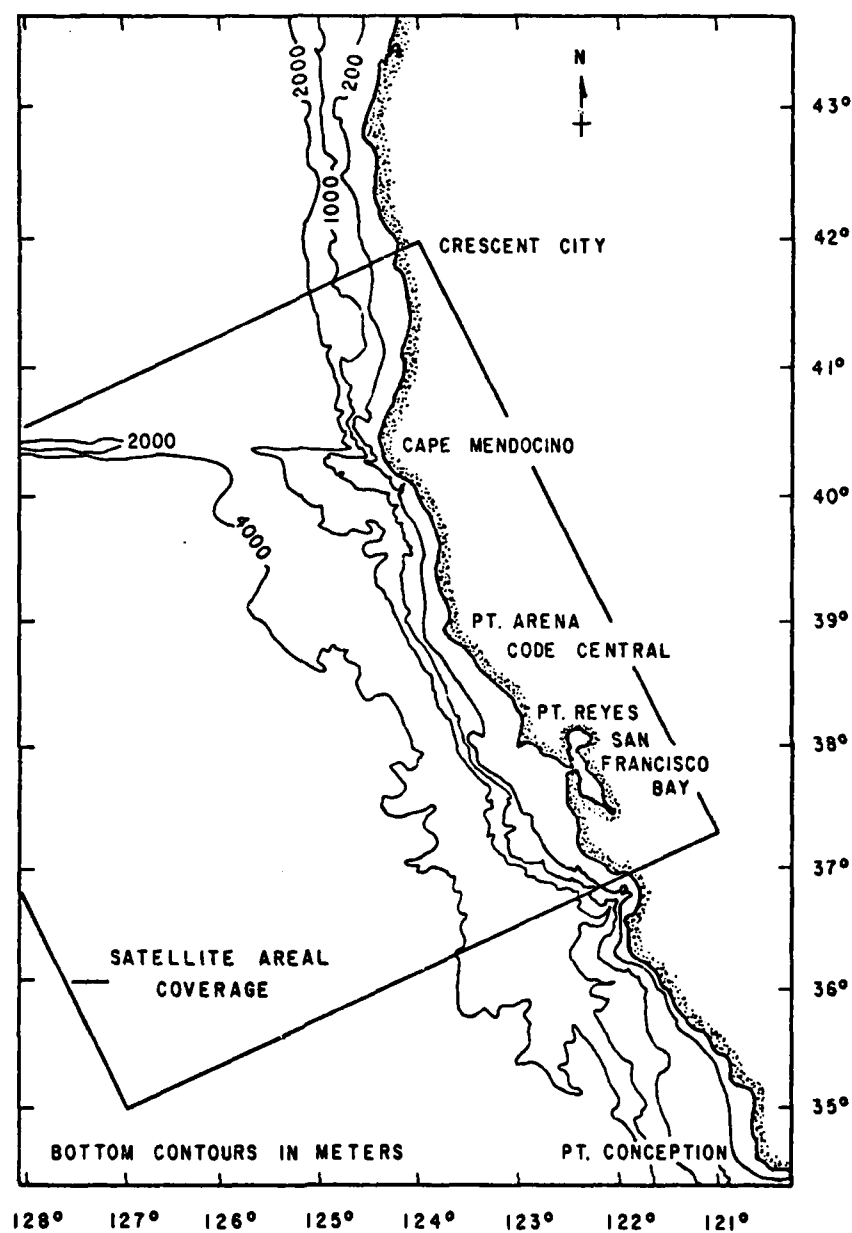


FIG. 1.1 NORTHERN CALIFORNIA BATHYMETRY

The large square outlines the area covered by the satellite images which was much larger than the area covered by the CODE moored array and most of the other measurements.

CHAPTER 2

DATA DESCRIPTION

This chapter briefly describes the the acquisition and preliminary processing of the satellite data as well as some sources of error and the problem of patchy coverage. Although the data are relatively easy to acquire, much processing and sorting are required before they can be analyzed quantitatively. The satellite images are not photographs, but are digital arrays of measurements that are usually displayed by color-coding the numbers. All of the data described here were recorded at the Scripps Satellite Oceanography Facility (SSOF) from the satellite NOAA-6. All data were Local Area Coverage (LAC), which have a spatial resolution of 1.1 km and are only available by transmission to local receiving stations as the satellite passes overhead. The data which are averaged and stored on the spacecraft and are archived by NOAA are Global Area Coverage (GAC) with an approximate spatial resolution of 4 km.

2.1 Data Collection

The NOAA satellites are polar-orbiting satellites which pass overhead twice per day. One pass is from north to south (descending) and one is from south to north (ascending). Successive passes shift to the east so that the satellite views the area of interest from a slightly different angle on each pass. Figure 2.1 shows the area scanned by the NOAA-6 satellite's radiometer on an ascending pass over the west coast of North America. The satellite subtrack (the line on the earth directly beneath the satellite) is shown near the center of

the area of coverage. The earth is scanned at right angles to the sub-track. The times (in GMT) at the right indicate when various areas were scanned. Figure 2.1 shows the area scanned in ten minutes on a single pass.

The edges of the image are so distorted that they are not useful for quantitative analyses. As the satellite shifts eastward the area of interest moves from the right-hand side of the image to the left-hand side. Approximately every five days a given area can be found only on the left-hand edge of one pass or the right-hand edge of the next pass (100 minutes later) so that no useful data can be obtained for a day or two.

The NOAA-6 satellite contains a passive radiometer called an advanced very high resolution radiometer (AVHRR). The AVHRR detects existing radiation in four specific frequency ranges or channels. The new version of the AVHRR, flown on NOAA-7, has five channels. The AVHRR rotates continuously, scanning the area beneath the spacecraft simultaneously in the four channels. The first two channels lie in the visible range, the third in the near infrared ($3.7 \mu\text{m}$) and the fourth entirely in the thermal infrared ($10\text{--}11.5 \mu\text{m}$). Channels 3 and 4 are sufficiently narrow to give high-resolution images of ocean surface temperature features. The noise-equivalent differential temperature (NEDT), which is a measure of the noise level of the instrument, is 0.1°C . for the AVHRR (Schwalb, 1978). The AVHRR scans points of known temperature on board the spacecraft to provide calibration measurements for the infrared data. This information is included in the data transmission.

The data are digitized on board the spacecraft before transmission to local receiving stations. Each datum is the value of the detected radiance averaged over approximately one square kilometer along the scan line. An image is constructed by stacking scan lines into a rectangular array of data. The SSOF maintains a file of the orbital elements (ephemeris) for each satellite, which combined with the precise time of transmission, determines the actual earth location of recorded data and the viewing geometry.

The quantity of data recorded and archived at the SSOF is enormous. Each ten-minute transmission from the NOAA-6 satellite contains 3600 scan lines with 2048 measurements per line for each of four channels. To cover the area marked in Figure 2.1, from the middle of California north to the Oregon border for a distance of several hundred kilometers offshore, requires an image which contains 512×512 measurements. This is the area which was processed for each image in the CODE-1 data set. When digital data are displayed as an image, each datum is called a "pixel," thus each image contains about 250,000 pixels.

Since the opening of the SSOF in the fall of 1979, the programming staff have created or modified a series of special programs for processing NOAA data. The preliminary processing described in section 2.2 comprises the first three steps in an overall sequence and uses these special programs on the SSOF computer (Young and Fahle, 1981).

Only channels 3 and 4 of the original image are required for the data analyses described here. Channels 1 and 2 are in the visible range

and contain no information in nighttime images. Many of the daytime images examined were found to contain unusable data in channel 3.

2.2 Preliminary Processing

The first step in processing each of the images is to correct for viewing-angle distortion by the satellite. Three factors contribute largely to the distortion problem. The first is the necessity of projecting the spherical earth onto a two-dimensional surface. Second, the sensor foreshortens the areas near the edge of its field-of-view. And lastly, the scanning of an image requires several minutes, during which time the earth rotates beneath the satellite. Knowing the satellite orbit, the time the image was scanned, and assuming that the radiometer always looks directly beneath itself, the image can be mapped to an equal-area projection. An algorithm developed by Legeckis and Pritchard (1976) of NOAA was adapted for use at the SSOF to remove image distortion.

The second step in processing an image is the registration of the image to a standard grid. The geometric-correction algorithm maps to an equal-area projection centered on the satellite subtrack, but this is not the same projection for each image. In addition one wants to extract the same area from each image and orient it to a specified direction. The registration algorithm locates a grid of points which are specified in longitude and latitude, and warps the image to fit this grid using a least-squares measure of fit. The registration algorithm locates the points in the grid by reading an earth-location file, created from the ephemeris and the geometric-correction program. Earth

location is determined by the orbit and viewing angle of the spacecraft, rather than by observing known landmarks, as is common in land-based image processing. This is important in oceanographic applications because there are no landmarks in most ocean images. The accuracy of image registration without the use of landmarks is approximately 5 km. The accuracy of image registration is limited primarily by how well the time of data transmission is known. A time error of one second results in a registration error of 6 km. If landmarks are visible in an image, as was the case for this series of images, they can be used to translate the registered image, which gives an accuracy in location of about 1-2 km.

The third step is the conversion of infrared radiance values to brightness temperature, assuming the ocean surface to be a blackbody. The calibration data from the spacecraft are used along with the blackbody relationship between temperature and radiance to convert the radiometer readings to degrees Celsius. This is the apparent temperature of the ocean as it is seen through the atmosphere. These temperatures were usually less than in situ sea surface temperature measurements by about 1 degree.

The next processing steps require algorithms which I developed for this study and which are described in Chapters 3 and 4.

2.3 Sources of Error

The errors in the satellite-derived temperatures can be divided into three categories: 1) sensor noise, 2) atmospheric and viewing angle errors, and 3) sea-surface effects. Corrections for the first two categories will be discussed in Chapter 4. Errors from the second and third categories are actually not errors in the sense of the satellite measuring inaccurately, but rather arise because the satellite may not measure the quantity which the oceanographer wants to know. Errors from the third category can only be examined by reference to another data set.

Sensor noise in the AVHRR is most noticeable in channel 3. The noise fluctuates both in intensity and in frequency probably because it is caused by interference from other instruments. Figures 3.1 and 3.2 show channels 3 and 4 of the same image and Figure 4.1a shows the nature of noise in channel 3. The noise level in channel 3 may reach magnitudes of 1° C.; the noise in channel 4 is negligible. Noise levels in channel 3 were high for the data which were acquired during CODE-1.

Atmospheric effects on sea-surface temperature are due to the approximately 800 km of atmosphere between the sea surface and the satellite. Water vapor in the air absorbs the infrared radiation emitted from the ocean and reradiates it at a lower temperature. The water vapor in an apparently-clear atmosphere will lower the perceived temperature up to several degrees. Clouds may completely obliterate the sea surface signal but be easy to detect or they may alter the signal slightly. Clouds smaller than the spatial resolution of the sensor (1

areas. Channel 3 may also be affected by scattering of infrared radiation, which would make the temperature appear higher than otherwise. Scattering was probably responsible for the hazy appearance of sea-surface features in channel 3 (as compared to channel 4) often seen in the morning passes.

Sea-surface effects are inherent in the method of observation. These effects arise from the opaqueness of the sea surface to infrared radiation (Stewart, 1983). The sea-surface signal received by the satellite originates in the upper fraction of a millimeter of the ocean's surface. Evaporation, diurnal heating and cooling, and the wind all affect this thin layer more than the water below. However, numerous experiments have shown that the satellite-derived temperatures are well-correlated with water several tens meters below the surface (Bernstein, et al., 1977, Van Woert, 1982). Chapter 6 describes how in situ measurements compared with the satellite data from CODE-1.

2.4 Patchiness

Although the satellite data can be acquired at regular intervals (twice per day), the usable data are patchy in space and in time, primarily due to cloud cover. Figure 2.2 gives a summary of the data available for CODE-1. For each image identified by a page number on Figure 2.2 a portion of the data near the CODE site is shown in the data report (Kelly, 1982).

Data were recorded only by request in 1981, all possible data were acquired only when there were few clouds or during periods

coinciding with ship-based experiments. At other times data were recorded and examined every few days. It was common to have no usable data for 5-6 days and then have three or four usable images in a row. There was an exceptionally long period of clear skies in July when 16 usable images were acquired over a period of nine days.

Because cloud cover determines data availability the data are biased toward certain weather conditions. In particular data were most often available during periods of strong, steady winds. Wind-biasing and its effects on the correlation between winds and SST patterns are discussed in Chapter 7.

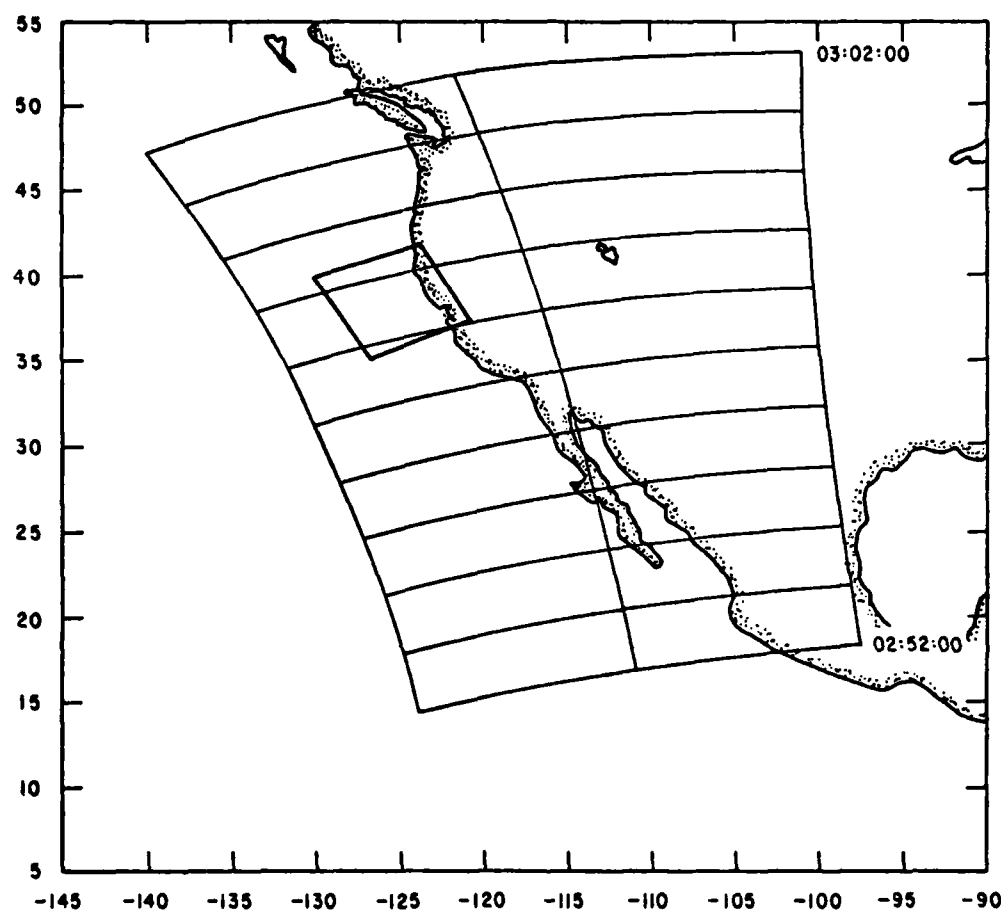


FIG. 2.1 AREA COVERED BY A TYPICAL NOAA-6 PASS

The lines mark one-minute intervals on the region scanned in ten minutes on an ascending pass. The north-south line is the satellite's subtrack. The smaller region is the area covered in the CODE images.

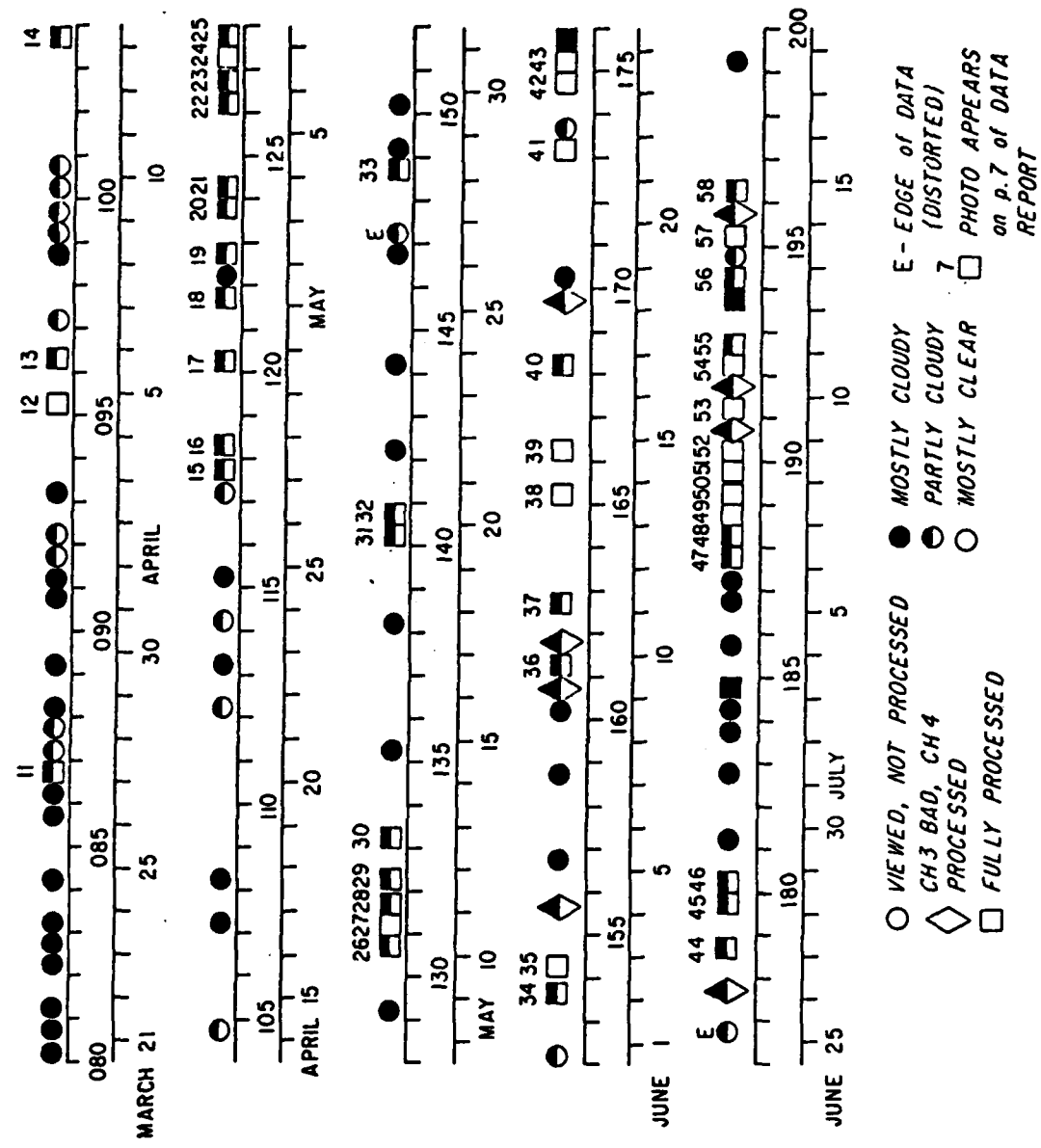


FIG. 2.2 SATELLITE DATA AVAILABLE FOR CODE-1 (1981)

Each image is designated by its year day, calendar date and degree of cloud contamination. The numbers above certain images give their page numbers in the data report (Kelly, 1982).

CHAPTER 3

CLOUD DETECTION

After the images were registered to a common grid the data were classified into usable and unusable data. The radiances recorded at the satellite were the infrared signal emitted by the nearest surface beneath the spacecraft, whether cloud tops, land or ocean, plus reflected and scattered radiation. Temperature measurements from clouds and from land were flagged so that they were not confused with ocean temperatures. Land was relatively easy to flag because after registration it was in nearly the same location in every image. Clouds are present to some degree in every image and must be identified because their signal is so large it would interfere with the SST analysis. Clouds are usually colder than the sea surface and their temperature variance is an order of magnitude larger than that for the ocean, but low clouds can be confused with cold fronts. This chapter describes the procedure which I developed to flag cloud-contaminated data. The enormity and tediousness of cloud flagging required a nearly-automatic procedure.

3.1 The Effect of Clouds on the Data

There are several forms in which clouds appear in the data. If the clouds form a dense mass, they obliterate the ocean signal beneath. The clouds may be dense but scattered, so that ocean features are visible between the clouds. Finally, the clouds may be smaller than the sensor resolution (1 km^2), and will not usually be visible in the image. Figure 3.1 shows a typical channel 3 image and Figure 3.2 shows the

channel 4 image. In each image light shades correspond to low temperatures and dark shades to high temperatures. The very light areas are clouds, the coast of California is on the right side of the image. The effect of dense clouds is that of a data glitch, not noise superimposed on the signal, because the signal from the clouds is larger than that from the sea surface. I simply flagged the areas where dense clouds were present as bad data. If the clouds are scattered, there is information between the clouds. My procedure retrieved this information only if the clear area was at least 5×5 pixels or $\approx 25 \text{ km}^2$. In the case of small clouds, one could model the effect of the clouds if the cloud temperatures were known (Bernstein, 1982). However, in general this information is not available and the range of possible values is great. These clouds remained as an uncorrected form of contamination. My cloud-detection procedure flagged an area slightly larger than the detectable clouds to minimize the effect of small nearby clouds.

3.2 Cloud Detection Methods

Numerous cloud-detection methods have been developed to identify clouds in satellite data. Most of these methods were designed to produce meteorologists with global cloud climatology for general circulation models. Thus they provide information on cloud amount, albedo and height, rather than sorting individual pixels into clouds and ocean. One notable exception looks for the one or more pixels in an image which are least likely to have cloud contamination, these pixels are used to obtain the most accurate possible sea-surface temperatures (Bernstein, 1982). Most algorithms use a visible channel to locate clouds and

therefore cannot be used on nighttime data. An exception to the use of visible data is an algorithm that finds clouds by pattern recognition using only infrared data (Coakley and Bretherton, 1982).

I wished to analyze the spatial patterns of SST's rather than determine cloud characteristics or accurate SST's, and in order to have any statistical reliability, I needed to use all available data. None of these existing algorithms was particularly suited to this problem so a new procedure was needed. This procedure was designed to meet the following goals:

- i) clouds must be detected in both daytime and nighttime data, i.e., the method cannot use a visible channel
- ii) each pixel must be designated as cloud, land, or ocean
- iii) the amount of usable data must be maximized
- iv) human intervention must be minimized.

3.3 A Method for Flagging Cloud-Contaminated Data

Starting with the Coakley and Bretherton technique as a model, I developed a pattern recognition scheme using only infrared data. The procedure consisted of two algorithms supplemented by some additional calculations and operator decisions. Appendix A contains an example of the complete procedure applied to one image. A flow chart for the process is shown in Figure 3.4. The first algorithm sorted subsets of the difference image (channel 3 minus channel 4) and the second algorithm computed statistics of subsets of the channel 4 image. The difference of channels 3 and 4 for the image shown in Figures 3.1 and 3.2 is shown in Figure 3.3. A suggestion by R. L. Bernstein, that the difference of

channels 3 and 4 could be used to screen data which could not be corrected for atmospheric effects, led me to examine this difference image in detail and to use it for cloud detection. Appendix B contains a discussion of the content of the difference image. Channel 4 (11 μm) is more sensitive to the presence of moisture in the atmosphere than is channel 3 (3.7 μm), subtracting the two channels removes the signal of ocean features while leaving the radiance signal of the moisture. The difference image gives a clear delineation of clouds and fog which are apparent, but less obvious, in either channel by itself. However, when the noise level in channel 3 is high ($\approx 1^\circ \text{C}$.), it is difficult to distinguish noise from scattered clouds. Noise levels for this entire series were large, because channel 3 was deteriorating with the age of the sensor, which made detection using the difference image less effective. Therefore, after an initial rough sort was done using the difference image, the remaining valid (ocean) areas in the channel 4 image were subjected to a pattern recognition algorithm.

Both algorithms relied on the statistics of subsets of the image, in this case 5×5 non-overlapping boxes. The method of analyzing subsets came from Coakley and Bretherton, who used a similar method to determine percent of cloud cover in infrared images. The output of each algorithm was a mask for the image. The cloud (and land) mask consisted of an array whose elements were either 0 or 1, zeroes correspond to invalid data (clouds or land) and one's to valid data (ocean). The dimensions of the mask are those of the original image divided by the subset dimension. I used images which were 500×500 pixels with 5×5 subsets, so that the mask size was 100×100 . Each mask value

corresponded to 25 pixels in the image. Data in the original image were not individually classified, they were classified in groups of 25 pixels.

3.4 Algorithm 1

In the difference image cloudy areas can be detected either by the mean value (very low or very high) or by jumps in adjacent values. The jumps derive from the inherently larger variability in cloud radiances. The first algorithm computed for each subset the average value and the maximum difference between adjacent pixels. Those subsets whose maximum differences exceeded a given threshold were flagged as clouds, the rest were subdivided by average temperature and assigned a code from 2 to 8, with larger numbers corresponding to larger mean values. By comparing this encoded version of the mask with the original image the coded values were interpreted as ocean or clouds. High values generally corresponded to dense clouds, occasionally, low values also corresponded to clouds. This is one of the steps that required a decision by the operator.

The land mask, which was needed for algorithm 1, was the same for each image because they were co-registered. It contained ones for ocean areas and zeroes for land areas. This land mask was created by a method similar to that of cloud detection, but it was done on a series of clear images using only a single channel. The cloud-detection algorithm detects land because its properties in the image are similar to those of clouds, i.e., highly-variable radiances. The cloud masks of these clear images were compared and those areas which were repeatedly

flagged were designated land. The land appeared as a cloud which was always in the same place.

3.5 Algorithm 2

The mask from algorithm 1 was refined by algorithm 2, which was applied to the channel 4 image. In the channel 4 image clouds appear as cold areas with high variability between adjacent pixels. The second algorithm required the mean channel 4 temperatures of the subsets which were valid according to the mask from algorithm 1. Since the sea surface is generally coldest along the coast and gets warmer offshore, the temperature threshold below which a subset was designated a cloud varied across the image. The mean temperatures were plotted as a function of their distance offshore to find a minimum temperature threshold which was described by a parabola of temperature versus offshore distance. The second algorithm used this minimum threshold parabola, along with a constant maximum threshold to classify the remaining subsets. Each subset was classified according to several criteria which would tend to invalidate it. The criteria included:

- i) mean temperature for the subset was outside the threshold limits
- ii) jumps of both signs between adjacent pixels occurred close together
- iii) several values in the subset differed significantly from the subset mean value
- iv) the number of positive jumps and the number of negative jumps in adjacent pixels exceeded a given limit

Each subset received an integer code, ranking it according to the severity and number of the criteria it met. The output of this step was a coded array.

The second part of this second algorithm edited the coded array by pattern recognition in the coded mask itself. Essentially, subsets with high rank were classified as clouds, those with low rank were classified as ocean, and the rest were classified according to how many neighboring subsets were clouds or ocean. Those subsets which could easily be classified by pattern recognition were left in their coded form. Here again, operator intervention was required to complete the classification into clouds and ocean. The editing by the operator completed the cloud mask. The second algorithm was rerun with more stringent limits if obvious cloud-contamination still remained. The final form of the cloud mask is shown as applied to the channel 4 image in Figure 3.5. Invalid subsets are shown as white and the valid areas contain the original image. This cloud mask was used as a bookkeeping device for further computations on the data.

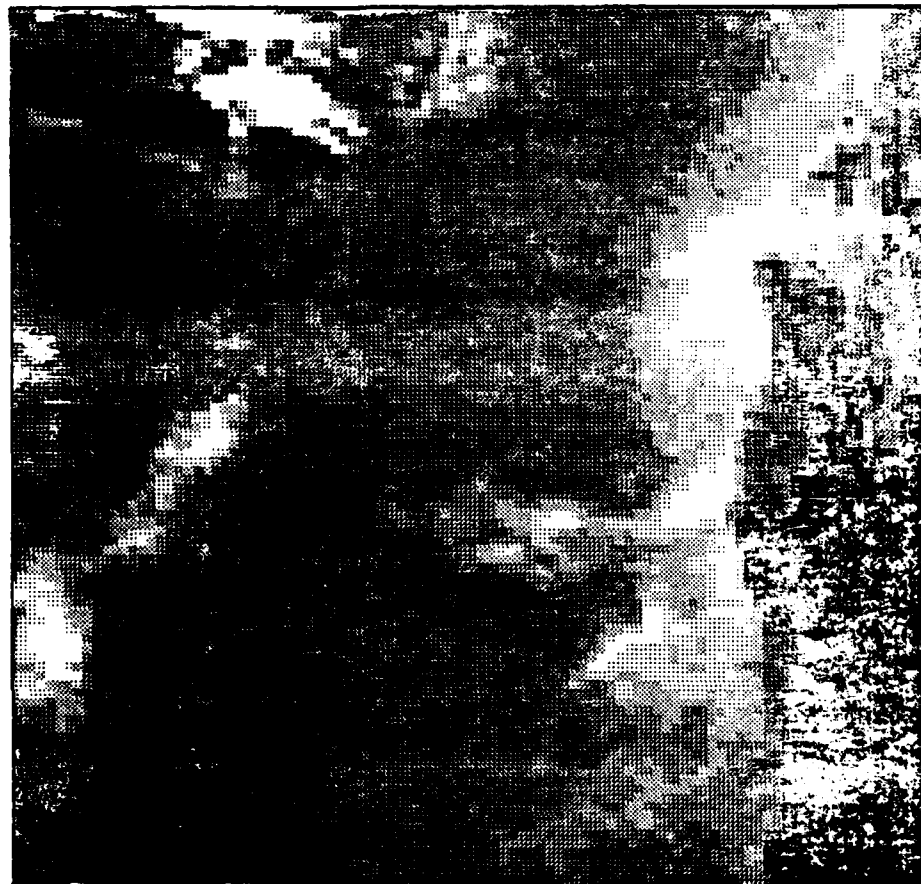


FIG. 3.1 CHANNEL 3 OF A TYPICAL IMAGE

Light shades correspond to low temperatures and dark shades to high temperatures. The warm area along the right side of the image is the coastline of northern California. The light shades in the center and left parts of the image are clouds.



FIG. 3.2 CHANNEL 4 OF THE IMAGE IN FIG. 3.1

Same as Figure 3.1, except channel 4.



FIG. 3.3 CHANNEL 3 MINUS CHANNEL 4

The difference of the images in Figures 3.1 and 3.2. There are no ocean features visible in the difference image. Clouds appear as very dark (warm) or very light (cold) areas.



FIG. 3.5 CHANNEL 4 IMAGE WITH CLOUD MASK

The mask computed with the cloud detection algorithms applied to the image in Figure 3.2. The masked areas are white.

CHAPTER 4

CORRECTION FOR ATMOSPHERIC EFFECTS AND SYSTEMATIC ERRORS

The temperature obtained from the calibration algorithm for AVHRR data is not the actual sea-surface temperature, but is instead the temperature of a blackbody that corresponds to the radiance seen by the satellite. This radiation is a combination of reflected and scattered solar radiation and thermal emissions from the ocean's surface, from cloud tops, and from the various gases in the atmosphere and includes the emissivity of sea water. To determine the actual SST of the ocean one must insure that reflected and scattered radiation is small compared with thermal emission, screen data which have been contaminated by cloud radiation and correct for the absorption and re-emission of radiation by gases.

One of the simplest methods for atmospheric correction uses a linear combination of the data from two or more channels of the AVHRR to obtain a more accurate temperature. This theory assumes that there are no more sources of error than there are channels because each additional channel gives one correction parameter. For the two-channel correction the errors are assumed to be predominately from a single process, i.e., water vapor absorption; thus, any data which might be contaminated by other sources must be eliminated. All multi-channel methods correct for atmospheric effects by sacrificing both the spatial and temporal resolution of the infrared data to obtain better absolute temperature accuracy. When all data that could possibly be contaminated by clouds or solar reflection have been removed, the number of measurements has been reduced by about 10^5 by this screening. The few remaining measurements

from numerous images are used to construct an SST map which has low spatial and temporal resolution, e.g., mean monthly temperature anomalies for the Northeast Pacific with 25 km resolution (Bernstein, 1982). My goal instead was to find an approximate correction for a series of images, eliminating only the data which was obviously contaminated, so I could maintain the best possible spatial and temporal resolution, this amounted to a reduction by about a factor of three.

Daytime and nighttime data may need different correction parameters, primarily because channel 3 is sensitive to solar radiation, and some multi-channel corrections are only valid for one type of data. By using only the infrared channels for cloud detection, as discussed in Chapter 3, I could use both daytime and nighttime data for my analysis, however, I could not eliminate pixels which contained clouds smaller than the sensor resolution of 1 km^2 . Assuming that I had sacrificed some temperature accuracy to keep data resolution and with the obvious clouds removed, I investigated the multi-channel correction as a method for approximately correcting a series of images.

4.1 Multi-channel Atmospheric Correction Theory

Deschamps and Phulpin (1980) presented a theory for correcting for the effects of the atmosphere on SST's based on two or more channels of the AVHRR. They wrote the radiative transfer equation governing the radiation at wavelength λ as

$$I_{\lambda} = B_{\lambda}(T_o)t_{\lambda}(0, p_o) - \int_0^{p_o} B_{\lambda}(T(p)) dt_{\lambda}(0, p) \quad (4.1)$$

where I_λ is the radiance measured at the satellite, T_0 is the temperature of a blackbody at p_0 , $t_\lambda(0,p)$ is the optical depth of the atmosphere between pressure levels p and 0 and $B_\lambda(T)$ is the Planck function which defines the relationship between any radiance value and the temperature of a blackbody that would give the same radiance

$$B_\lambda(T) = I_\lambda.$$

The temperature obtained when the radiance is inverted with the Planck function is called the brightness temperature and is generally not the actual temperature of the radiator. The first term in equation 4.1 is the (sea) surface radiance transmitted to space and the second term is the radiation of the atmosphere. No term for reflected radiation was included; Deschamps and Phulpin stipulated that their method was not suitable for daytime data where reflection would be important. Using 4.1 the error in the radiance, δI_λ , can be written:

$$\delta I_\lambda = B_\lambda(T_0) - I_\lambda = - \int_0^{p_0} [B_\lambda(T_0) - B_\lambda(T(p))] dt_\lambda(0,p) \quad (4.2)$$

where for small changes in T ,

$$\delta T_\lambda = \delta I_\lambda \left[\frac{\partial B_\lambda}{\partial T} \right]_{T_0}^{-1}. \quad (4.3)$$

The following assumptions were made to linearize the problem:

- i) absorption by atmospheric gases is so low that

$$dt_{\lambda}(0,p) = -k_{\lambda}dU(p) \quad (4.4)$$

where t_{λ} is the absorption coefficient and $dU(p)$ is the "content" of absorbing gas between 0 and p .

ii) changes in the Planck function can be approximated by the first two terms of a Taylor's series:

$$B_{\lambda}(T) = B_{\lambda}(T_0) + \left[\frac{\partial B_{\lambda}}{\partial T} \right]_{T_0} (T - T_0) . \quad (4.5)$$

Then the "error" in the temperature measured by the AVHRR can be written

$$\delta T_{\lambda} = T_0 - T_{\lambda} = k_{\lambda} f(T(p)U(p)) \quad (4.6)$$

where f is not a function of λ . This formulation allows T_0 to be found from a linear combination of the T_{λ} 's computed from different channels.

Some problems with the Deschamps and Phulpin formulation are the following:

- i) it only applies to nighttime data;
- ii) the first assumption implies that the source of contamination in all channels is absorption by one gas or that the concentration of absorbing gases are well-correlated. This one source is generally interpreted as water vapor; however, Chahine (1981) argued that other processes, e.g., reflected solar radiation, variations in sea-surface emissivity, haze and scattering, were equally important in channel 3.
- iii) the Planck function is not linear near $3.7 \mu\text{m}$, the

channel thought to give the most accurate sea-surface temperatures.

The first assumption of Deschamps and Phulpin is not a serious limitation because a linear correction can be used effectively on a non-linear problem; however, Chahine's arguments are important in that the number of processes contributing to the error probably exceeds the number of channels available for the correction. Thus, one cannot correct for errors from all the processes.

Several researchers have attempted to determine the coefficients for this multi-channel correction, notably McClain (1981) and Bernstein (1982). Their methods are similar so Bernstein's results will be discussed in this chapter. Bernstein posed the two-channel problem, as did McClain, as follows:

$$Z = T_s - T_3$$

$$Z' = a_0 + a_1(T_3 - T_4) + a_2T_3$$

where T_s is the sea-surface temperature measured in situ, and T_3 and T_4 are the channel 3 and channel 4 temperatures, respectively. Z is the error in the measured temperature, Z' is a correction term, and a_0 , a_1 and a_2 are coefficients to be determined. Using the coefficients computed from a multiple regression, Bernstein reported an improvement in the temperature accuracy as a reduction in the standard deviation of Z from 0.91°C . to 0.56°C . when the correction term was subtracted. Bernstein's results are analyzed along with the results for the CODE data in section 4.3.

4.2 Noise Removal

For the CODE data I attempted to find an atmospheric correction using a linear combination of channels 3 and 4, however, first it was necessary to reduce the noise level in channel 3 data. As instrument noise increases, the quality of the computed sea-surface temperature degrades accordingly. Deschamps and Phulpin (1980) estimated that as instrument noise or residual atmospheric contamination increased from 0.05°C . to 0.5°C . the minimum estimation error for the AVHRR would increase from 0.29°C . to 0.83°C . Channel 3 of every AVHRR has had high noise levels, which have increased with the time since the spacecraft was launched. For the CODE data, which were collected two years after the launch of NOAA-6, rms noise levels were as high as 1°C . The noise in channel 3 is periodic with slowly-varying wavenumbers and has length scales comparable to the smallest ocean temperature features (see Figure 4.1a). The image from channel 4 is nearly noise-free. The predominate noise is a series of stripes oriented along a scan line of the original image.

If the full spatial resolution of the data is not required, then the noise-removal can be effected by smoothing the data, however, using both channels it is possible to remove the noise without smoothing small ocean features. A standard image-processing technique to remove this noise is to perform a two-dimensional Fourier transform on the image and to remove the noise spikes in the Fourier magnitudes by inspection. This procedure requires examining the Fourier transform of each image and deciding which coefficients are noise. The noise does not always recur in the same place in the Fourier domain so that this cannot be

done automatically. An alternative method which I developed for this time series takes advantage of the similarity of the image from channels 3 and 4. The image which is the difference of the channels (literally, channel 3 minus channel 4) contains no observable ocean features (see Figure 3.3). The features which can be seen are the sensor noise, clouds and some detail in the land. Ocean features are not apparent because the coefficient of emissivity of sea water is approximately spatially constant and both channels record the radiance from exactly the same area.

If channel 4 is assumed to be noise-free, extracting the noise from the difference of channels 3 and 4 is equivalent to extracting the noise from channel 3. The advantage of using the difference image is that small length scales in the sea-surface signal are not affected by the removal of the noise. The errors induced by this method include 1) introducing channel 4 noise into channel 3, and 2) contaminating clear ocean areas with the colder cloud temperatures from small clouds and from the edges of large clouds. The details of this technique are discussed in Appendix B. Figure 4.1a shows the channel 3 image before the noise was removed and 4.1b shows the channel 3 image after the noise was removed. This filtered version of the channel 3 image was used in subsequent comparisons discussed in this chapter.

4.3 Comparison of Satellite and Thermistor Data

To investigate the effectiveness of a multi-channel correction for point measurements, I compared the satellite data with temperature measurements from thermistors on CODE current meter moorings and an NDBO buoy near the moorings. Records from four thermistors at depths of 1 m below the surface were available from April to August 1981 (Brown, Irish and Bratkovich, 1981). These thermistors were located at C3, C5, R3 and near S4 as shown in Figure 6.1. The thermistor located on mooring C3 was not used in the analysis because it fell within a 5 km x 5 km box which was designated land by the mask, which was described in Chapter 3.

The effects of registration error and of spatial aliasing from the advection of strong temperature fronts were minimized by comparing hourly averages of the thermistor records with spatial averages of the satellite data. For each image the one-hour average thermistor value corresponding to the time of satellite data collection was compared with a 5 km x 5 km average of channel 3 and channel 4 temperatures at the thermistor location. Figure 4.2 shows a plot of this comparison for mooring C5. The symbols on each line indicate actual measurements, the symbols have been connected by straight lines. Note that the channel 3 and channel 4 measurements appear better correlated with each other than with the thermistor values. Channel 4 is generally, but not always, colder than channel 3 and both channels are usually colder than the thermistor measurements.

The multi-channel correction is best treated as a linear prediction problem where the channel 3 and channel 4 temperatures are used to

predict the thermistor temperature. The method used here is based on Davis (1977) and is described in Appendix C. The mean of each record was first removed and then each of the variables was fit to the thermistor record using a least-squares fit. The measure of the effectiveness in predicting the thermistor record is the amount of total variance that the prediction can explain and is called the skill. If α is found by least-squares such that

$$\underline{T}_s = \alpha \underline{T}_3 + \underline{e} \quad (4.7)$$

where \underline{T}_s is the vector of (demeaned) thermistor measurements, \underline{T}_3 is the vector of (demeaned) channel 3 measurements, and \underline{e} is the vector of errors, then the skill in estimating \underline{T}_s by the variable \underline{T}_3 is

$$1 - \underline{e}^T \underline{e} [\underline{T}_s^T \underline{T}_s]^{-1} \quad (4.8)$$

where \underline{e}^T is the transpose of the vector \underline{e} . For two variables two coefficients are found such that

$$\underline{T}_s = \alpha \underline{T}_3 + \beta \underline{T}_4 + \underline{e} \quad (4.9)$$

For each variable used in the prediction an artificial skill, S_A , is added, related to the finite size of the data set. For variables not well-correlated with the quantity to be predicted, the artificial skill can be approximated as

$$S_A = \frac{M}{N^*} \quad (4.10)$$

where M is the number of variables used and N^* is the equivalent number of degrees of freedom of each variable. When the addition of a variable does not improve the skill by substantially more than S_A , the additional variable is not contributing to the real skill.

Table 4.1 shows the results of this analysis on the CODE thermistor data, using only those images for which cloud-free satellite temperatures could be found for all three thermistors. A total of 113 measurements was used. In this case N^* is no larger than the number of measurements, so the artificial skill from using each variable is $1/113$ or $\approx 1\%$. For the CODE data the addition of channel 3 improved the skill of channel 4 by only 0.5%, which is less than the artificial skill, so the second channel is not contributing to the actual skill. The fact that channel 3 by itself has some predictive skill is just a result of the high correlation between channel 3 and channel 4: their correlation coefficient is 0.67. The rms error for the CODE data using channel 4 is 0.80°C .

This analysis was repeated on the data published by Bernstein (1982) and the results are shown in Table 4.2. The problem posed by Bernstein can be rewritten by a simple algebraic manipulation in the same form as that used on the CODE data. In this rewritten form, when means are added back into the variables, the coefficients in Table 4.2 are identical to those found by Bernstein (1982). The number of measurements in Bernstein's data is 42 so S_A is $\approx 2\%$ for an additional

variable. Only a 0.3 % improvement was found using channel 4 in addition to channel 3. Bernstein's data shows high predictive skill for each channel. The rms error using only channel 3 is 0.63°C .

The predictive skill for Bernstein's data is much higher than that for the CODE data. The probable explanation for this difference was provided by Bernstein (personal communication) who suggested that the climatological mean should be removed from his data before the skill analysis is done. Bernstein's data covered a large part of the globe, the SST prediction for his data includes a spatially-varying mean temperature as well as an anomaly. The CODE data came from a small region whose mean is nearly the same as the mean of the set of measurements, thus the prediction includes only the anomaly. This difference in the SST to be predicted can be seen in Tables 4.1 and 4.2: the variance of T_s is 24.1 for Bernstein's data compared with 0.93 for the CODE data. A large mean in the variables will increase the apparent estimation skill, which can be seen from equation 4.8 as an increase in skill with an increase in the variance of T_s .

In both the CODE data and Bernstein's data the use of a second channel does not contribute to the accuracy of the sea-surface temperature estimates for point measurements. The skill analysis for Bernstein's data might be improved by removing a climatological mean, however, this analysis shows no evidence that a linear combination of these two channels gives more estimation skill than a single channel.

4.4 Comparison of Consecutive SST Maps

A point comparison of the satellite data with the thermistor temperatures shows how much the two measurements differ, but it is not particularly useful in finding systematic errors. Comparing the temperature maps (the entire images) with each other shows how the satellite data differ from physically realistic ideas of sea-surface temperature.

There are surprisingly large differences in the mean temperatures of images which are near in time. This can be seen in the CODE data report as a variation in the range over which the channel 3 images were enhanced (Kelly, 1982). Because each image has a different cloud-free area, it is difficult to obtain mean values for a series of images. Instead for each channel I computed the mean difference over the common clear area between pairs of images separated by 12 or 24 hours. This measure was chosen because it seemed unlikely that the mean ocean surface temperature would change very much over short times. Only those pairs of images for which the common clear area exceeded $20,000 \text{ km}^2$ (16,000 pixels) were used. The results are shown in Table 4.3. The images are identified by their year days and are from the evening pass (approximately 8 pm PST) unless followed by an A, which marks them as from the morning pass (8 am PST). Note that the year days are based on GMT so that, for example, the image labeled 127 precedes 127A by about 12 hours.

The statistics of the pairs of images are summarized in Table 4.4, which shows the rms differences in each channel for the type of

data pair. From Table 4.4 it can be seen that

- i) channel 3 has consistently larger jumps in the mean value than channel 4,
- ii) there are no significant differences in the magnitude of morning data jumps versus evening data jumps,
- iii) there is no significant diurnal signal because the pairs of data at 12-hour separations have the same size jumps as those at 24-hour separations.

These systematic errors could be expected to contribute a large error to the point measurements. If the mean of each image has an expected error of σ , and if the mean temperature of the ocean does not change in 24 hours, then the expected error of the mean difference of two images will be $\sqrt{2} \sigma$. Therefore, for the mean difference in channel 4 of 0.78°C ., the expected error for each image is 0.55° , which is nearly large enough to account for the 0.80° deviation of the channel 4 temperatures from the thermistors.

Some possible explanations for these jumps were compiled with the help of R. L. Bernstein :

- i) advection of strong temperature fronts
- ii) AVHRR calibration errors
- iii) variations in the gas content of the atmosphere
- iv) variations in radiance due to satellite viewing angle or sun angle
- v) variable wind speeds

A spot check of some of these pairs showed that the mean difference was not a result of the advection of strong temperature features, but was

nearly uniformly distributed over the image. A check of the calibration data for a pair of images whose mean difference was greater than 1° C. showed stable calibration values even in channel 3, which was very noisy.

If the atmosphere was causing the jumps, either because of highly variable optical depth or because the satellite must view the sea surface through more atmosphere at large viewing angles, then one would expect to be able to correct one channel using the other, following the argument of Deschamps and Phulpin. However, the differences in channels 3 and 4 were uncorrelated.

Winds could affect the satellite sea-surface temperatures in two ways. First, the wind mixes the surface layer with the water below, creating a sudden change in temperature over a large area. Second, the emissivity of sea water is a function of the roughness of the sea surface, which varies with wind speed. To examine the importance of winds I compared mean channel 4 temperatures with the magnitudes of the wind at CODE mooring C5. Although it was not possible to obtain the mean values for the entire CODE series, for one exceptionally clear period in July 1981, I obtained mean values over the common clear area. These mean values for channel 4 are plotted in Figure 4.3. The clear area was 36,050 pixels or approximately $43,600 \text{ km}^2$ and covered nearly the entire north-south extent of the image along the coast. The rms mean temperature difference for the images separated by 12 hours is 0.71° C., for 24-hr separations it was 0.63° C., which suggests that the July images are typical of the entire CODE series. For this period winds were consistently southward and there was no obvious change in wind speed

corresponding to, for example, the very low mean temperature on day 191.

To examine the effect of viewing angle on the mean temperatures I estimated the distance between a fixed point in the image and the satellite subtrack. These distances are shown in Table 4.5 along with the direction of the fixed point location relative to the subtrack. Sun-satellite-sea surface geometries are shown schematically in Figure 4.4 which defines the viewing angle, θ , and the sun-satellite-sea surface angle, ϕ . Although these angles can now be computed using an algorithm at the SSOF, they are not easily computed for the CODE data, which was processed before the algorithm was introduced. The angle, θ , was computed for the distance estimates in Table 4.5. At sunset and at sunrise the angle ϕ is given by

$$\phi \approx \theta + 90^\circ, \quad \text{sunset}$$

$$\phi \approx \theta - 90^\circ, \quad \text{sunrise}$$

where θ is positive when the pixel being scanned is west of the satellite. The magnitude of ϕ decreases as the sun rises above the horizon. For the CODE series which ran from March through July, the magnitude of ϕ fluctuated with the data collection time, but generally decreased through the series.

When the pixel in Figure 4.4 is between the sun and the satellite, the AVHRR is more likely to pick up reflected infrared radiance from the sun. This translates to images lying to the east of the subtrack in the morning and to the west of the subtrack in the evening.

Table 4.5 also shows which days had obvious contamination in the channel 3 image: all these images come from morning passes with the CODE area to the east (sun side) of the subtrack, which suggests that reflected solar radiation is responsible for the degradation of the channel 3 image.

Solar reflection is not considered a source of contamination for channel 4, the viewing angle, θ , could affect channel 4 temperatures through the angular dependence of emissivity, ϵ , which is defined as

$$\epsilon = \frac{I_{\lambda}}{B_{\lambda}(T)} = \frac{\text{observed radiation}}{\text{radiation for a blackbody}}.$$

The cosine of the viewing angle, θ , is plotted in Figure 4.3, which shows a clear correlation between viewing angle and mean channel 4 temperature. For infrared radiation at the sea surface the transmittance is negligible so that

$$\epsilon = 1 - \rho(\theta) \quad (4.11)$$

where ρ is the reflectance and is given by the Fresnel reflection coefficients. These coefficients are complicated functions of the complex dielectric constant for seawater and the sines and cosines of θ (Stewart, 1983).

To determine the dependence of the temperatures on viewing angle one needs to examine the equation for brightness temperature

$$T_{\lambda} = B_{\lambda}^{-1}(I_{\lambda})$$

where

$$I_{\lambda} = z B_{\lambda}(T_s) \quad (4.12)$$

and T_s is the actual SST. Also since

$$\frac{\partial z_{\lambda}(\theta)}{\partial \theta} = - \frac{\partial \rho(\cos \theta, \sin \theta, \lambda)}{\partial \theta},$$

for small changes in θ

$$\begin{aligned} \frac{\partial T_{\lambda}}{\partial \theta} &= \frac{\partial B_{\lambda}^{-1}(T)}{\partial I_{\lambda}} \frac{\partial I_{\lambda}}{\partial \theta} \\ &= - \left[\frac{\partial B_{\lambda}(T_s)}{\partial T} \frac{1}{B_{\lambda}(T)} \right]^{-1} \frac{\partial \rho}{\partial \theta} \end{aligned} \quad (4.13)$$

where the term in brackets is the sensitivity for the given λ . The sensitivity for channel 3 is about twice that for channel 4.

Now because $\frac{\partial \rho}{\partial \theta}$ is a function of $\cos \theta$ and $\sin \theta$, it can be approximated for small angles by powers of $\bar{\theta}$, the average value of θ for an image pair. The correlations between $\frac{\partial T_4}{\partial \theta}$, $\frac{\partial T_3}{\partial \theta}$ and the powers of $\bar{\theta}$ were computed for the pairs of images in Table 4.3. The results are shown as the skill for each estimator in Table 4.6. The artificial skill for each computation is also shown. For channel 4 good correlations were obtained between the differences in temperature and the odd powers of $\bar{\theta}$,

$$\delta T_4 \approx - \alpha \bar{\theta} \delta \theta. \quad (4.14)$$

Integrating equation 4.14 gives

$$T_4(0) \approx T_4(\theta) + \frac{\alpha}{2} \theta^2. \quad (4.14')$$

Because this relationship is symmetric with respect to θ one can assume that this is purely a viewing angle problem unrelated to the location of the sun.

For channel 3 the highest skill was obtained for evening data and, following the same argument

$$\delta T_3 \approx \alpha \delta \theta \quad (4.15)$$

and

$$T_3(0) \approx T_3(\theta) - \alpha \theta \quad (4.15')$$

Comparing this correction term with the evening geometry in Figure 4.4, one can see that as the pixel moves toward the sun (and greater possibility of reflection) the measured temperature gets larger. The channel 3 correction is asymmetric with respect to θ and therefore must be related to sun position, so that one would expect that the actual correction term for channel 3 would involve the sun-satellite-sea surface angle, ψ .

Predictive skill for morning data was significantly less and included both even and odd powers of θ . Mean differences in morning

data may involve other processes or may be more dependent on \bar{T} . This problem cannot be resolved with the limited data available here.

4.5 Relating Map Errors to Point Errors

One would like to know is whether these systematic errors from satellite geometry are the errors responsible for the low correlations between satellite data and the thermistor measurements. I computed a correction term for each image included in the thermistor comparison using the approximate corrections given by equations 4.14' and 4.15' for channels 3 and 4. These constants were added to the original values and the skill of each channel in predicting the thermistor measurements was again computed. The results of this analysis are presented in Table 4.7. Correction terms were computed for all channel 4 data, however, given the increase in artificial skill associated with adding the correction term, there was no improvement in the predictive skill of channel 4 with the corrections. Channel 3 corrections were computed only for evening data. There was a significant improvement in the predictive skill of channel 3 data when the correction term was added, so that for evening data it is a better predictor of thermistor temperatures than is channel 4. This result is in agreement with Bernstein's data which showed that channel 3, under certain conditions, is a better predictor of SST's.

4.6 Using Maps to Study Atmospheric Correction

The multi-channel correction was shown in section 4.3 to be ineffective for point data comparisons with thermistors. But perhaps the errors due to the viewing angle and the sun angle described in section 4.4 dominated the variance analysis, if these systematic errors could be removed, a significant error reduction could be found using two channels. Using the method of comparing consecutive maps I again checked for the effectiveness of a multi-channel correction. Assuming a correction of the form given by equation 4.9, the equivalent statement for the consecutive maps is

$$\delta T_s = \alpha \delta T_3 + \beta \delta T_4 + e \quad (4.16)$$

where the differences are computed for images separated by short times, 12 or 24 hours. Assuming that the actual SST, T_s , does not change equation 4.16 can be rewritten

$$\delta T_4 = \gamma \delta T_3 + e \quad (4.17)$$

where only the ratio of the constants, γ , can be determined and e is an error term.

In section 4.4 it was shown that there is no significant correlation between the spatially-averaged terms, δT_4 and δT_3 . But suppose the mean values are dominated by the viewing-angle errors and that there are atmospheric errors which vary in magnitude across the image. This could happen if, for example, the left side of the first image contained

very moist air while the right side was drier and all the moisture was gone the next day. This would create an error pattern across the image where the left side appeared cooler on the first day than the second day, but the right side did not change.

As in section 4.4 I used the differences of image pairs for all cloud-free data, however, I did not average spatially, but kept all the points for the variance analysis. I removed the spatial average of each image pair from each point for channel 4

$$\delta T'_{4_i} = \delta T_{4_i} - \overline{\delta T_{4_i}}$$

and similarly for channel 3. Removing the mean reduced the total variance by 69 %, which suggests that spatially-constant errors are much larger than spatially-varying errors. If the errors in the satellite-derived temperatures were due to undetected clouds, one would expect a large variance which would vary spatially. The small clouds responsible for the errors would move in 12 or 24 hours so that the error would be in a new location in the next image. Only 31 % of the total variance was spatially-varying and this fraction necessarily includes temperature changes from advection of SST anomalies. Thus, the residual variance which could be caused by undetected clouds is much less than one-third of the total.

Taking account of the correlation between nearby data in the same image pair, I computed an equivalent number of degrees of freedom for all the data and an estimate of the artificial skill of 0.06 %. The computed value of γ for the demeaned variables was 0.25 and the

reduction of the remaining variance was 9 %, which is significant if not large. Computing γ for Bernstein's data from Table 4.7, where

$$\gamma = -\frac{\alpha}{\beta}$$

gives a value of 4.1, so that the magnitude of the corrections are not comparable. In terms of Bernstein's formulation in section 4.1, using his value for a_2 , the value of a_1 would be -1.3 compared with Bernstein's 0.31. Therefore, if the problem is posed as a correction to T_3 using the difference of the channels, $T_3 - T_4$, the correction I found disagrees both in sign and in magnitude with Bernstein's results.

4.7 Conclusions

The satellite data were checked for errors using individual measurements, entire images and the mean properties of images. The analysis of the mean properties of the SST maps showed the following:

- i) the large variations in the means of SST maps were systematic errors related to the satellite viewing geometry,
- ii) variations in the mean for channel 4 were smaller than those for channel 3 and were more predictable,
- iii) variations in the mean in channel 3 were uncorrelated with those in channel 4,
- iv) errors in channel 4 were well-described by the angular dependence of emissivity (Fresnel reflectance). A crude correction for viewing angle eliminated 75 % of the variance in mean temperatures; a more effective correction could

undoubtedly be computed from the Fresnel relationship and the exact viewing angle.

v) errors in channel 3 differed for morning and evening data and included a correction for the sun angle.

vi) errors from the sun angle were frequently so large that the data were unusable, channel 4 did not contain such large errors.

The use of a second channel did not produce a better SST map than that obtained from a single channel. A comparison of the CODE satellite data with thermistor measurements showed that two channels did not give significantly better agreement with the thermistors than a single channel, even after a correction for viewing geometry was added to each channel. The analysis of entire images produced a small significant correction using a second channel which disagreed substantially with the correction terms found by both Bernstein and McClain for point measurements. Thus, a small atmospheric correction for an entire image may be possible using these two channels, however, the correction would be small compared to the correction needed for viewing geometry. To make use of a multi-channel correction one would need to remove the sensor noise from channel 3 and to find a correction for sun-angle errors in channel 3 data. With a viewing-geometry correction, channel 3 by itself might be a better estimator of in situ temperatures than channel 4, at least for evening data. These analyses were done exclusively on the four-channel version of the AVHRR on NOAA-6. On the new instruments channel 4 was split into two channels. Some combination of the three infrared channels may produce better SST maps: a statistical analysis of

the new channels has not been done.

Small clouds, which are commonly thought to be the largest source of error in satellite-derived SST's, did not appear to be a significant source of error for the SST maps. Large clouds were removed before attempting the error analysis and small unresolved clouds could be expected to contribute spatially-varying errors. The analysis of individual points from entire images showed that spatially-constant errors were much larger than spatially-varying errors: nearly 70 % of the variance between consecutive images was described by a constant. The remaining 30 % included variance from the advection of SST anomalies, which is not an error, as well as the error from small clouds. Therefore, the contribution of small clouds to the error variance was substantially less than 30 %.

Because the determination of a viewing-angle correction term for the channel 3 morning data was inconclusive and because the channel 4 correction was effective in removing jumps in the mean temperature, channel 4 data were used in all analyses in the following chapters. An empirical correction for channel 4 was applied to each image based on equation 4.14': a constant was added to each image, which was a function of its approximate viewing angle. Channel 3 was not used in any form after the cloud-detection step which was discussed in Chapter 3.

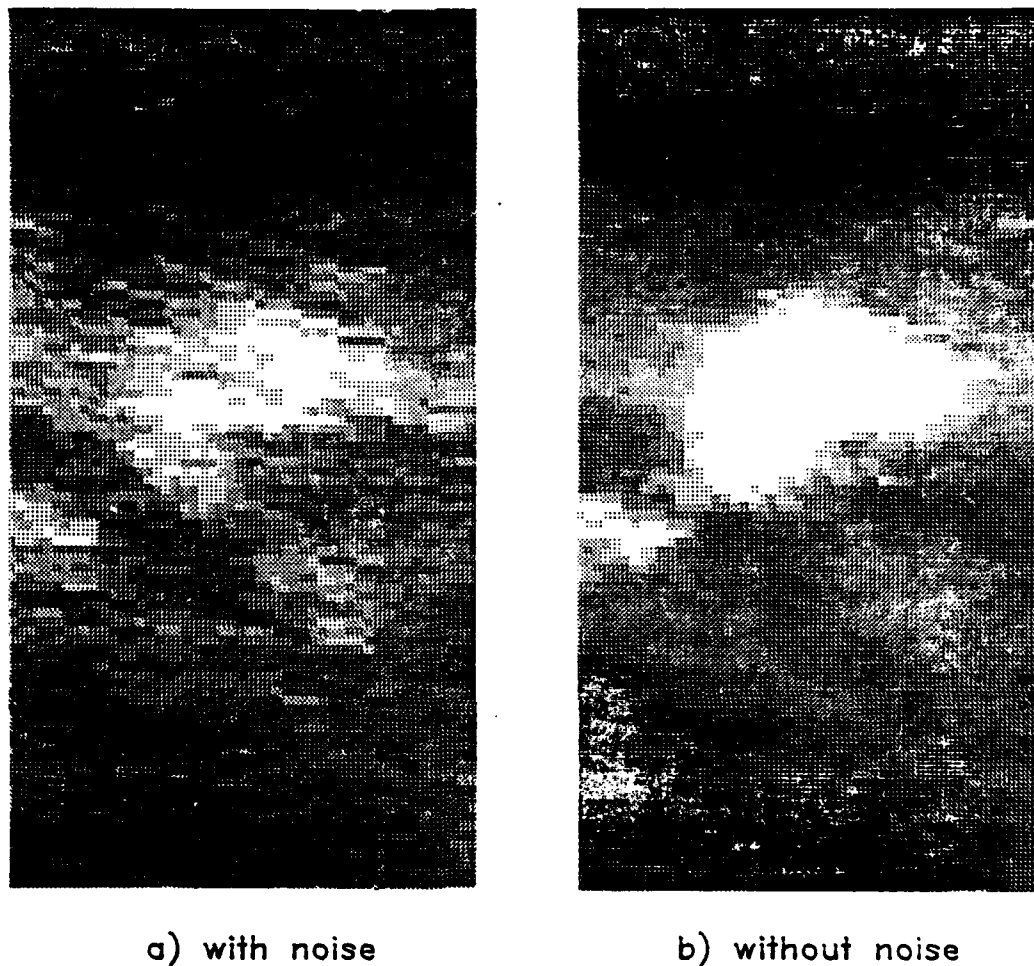


FIG. 4.1 CHANNEL 3 BEFORE AND AFTER NOISE REMOVAL

A portion of the image in Figure 3.1 is shown a) before the instrument noise was removed as described in Appendix B and b) after the noise was removed. The white area in the center of the figures is a cloud.

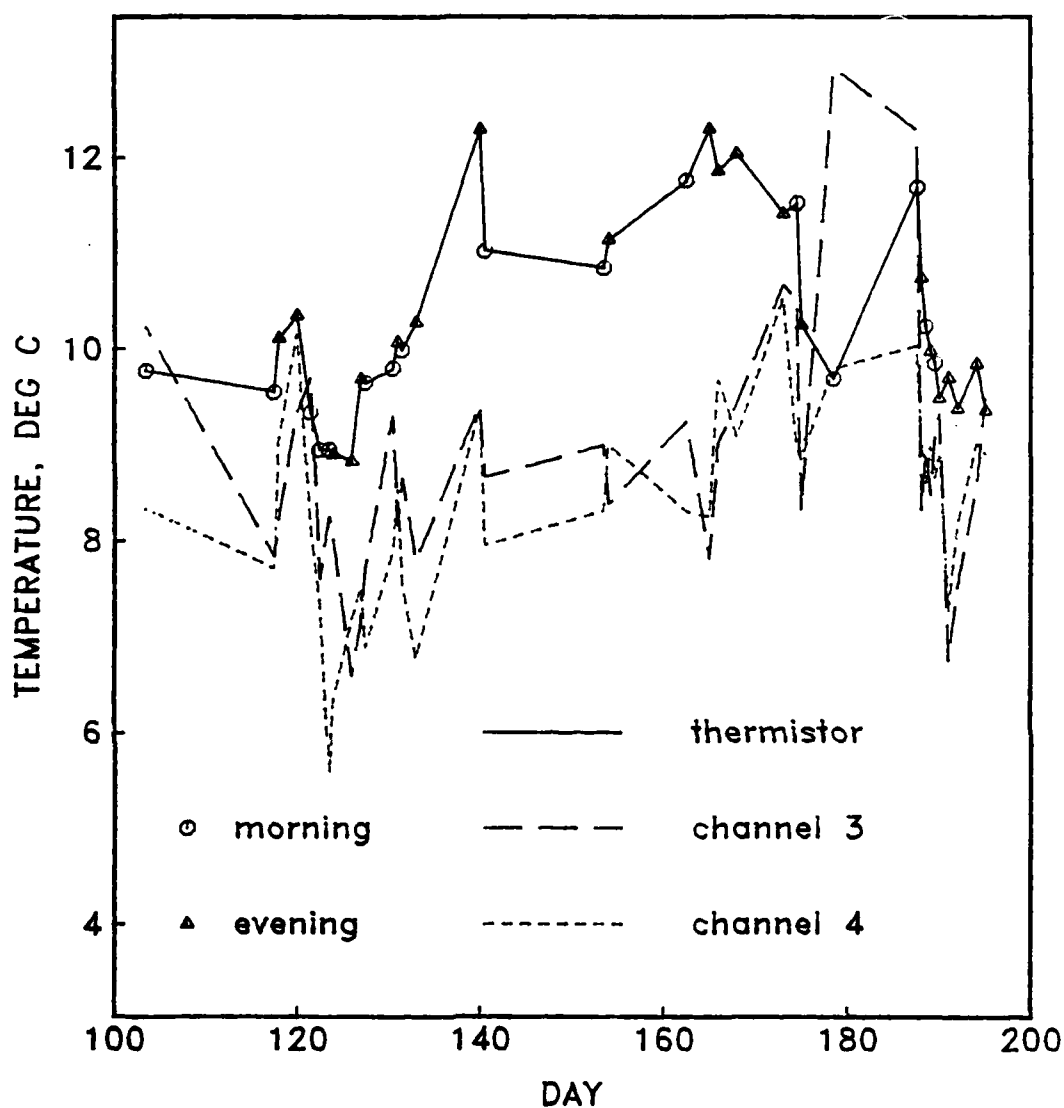


FIG. 4.2 COMPARISON OF SATELLITE AND THERMISTOR SST

Temperatures from channel 3, channel 4 and in situ thermistors plotted versus the day of the observation. Symbols indicate the actual measurements and the data type (morning or evening). Measurements are connected by straight lines. Note the close correlation of channels 3 and 4.

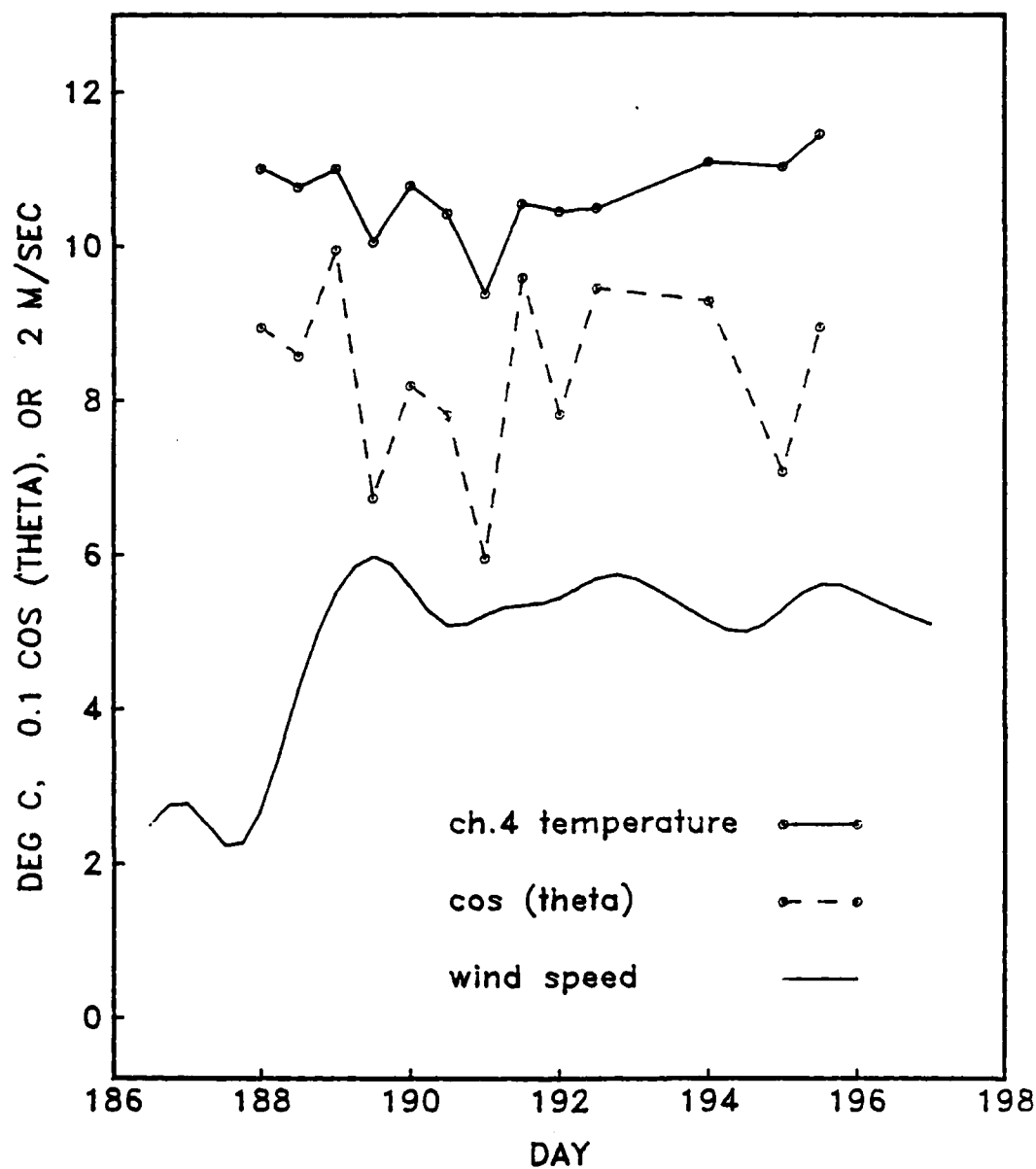
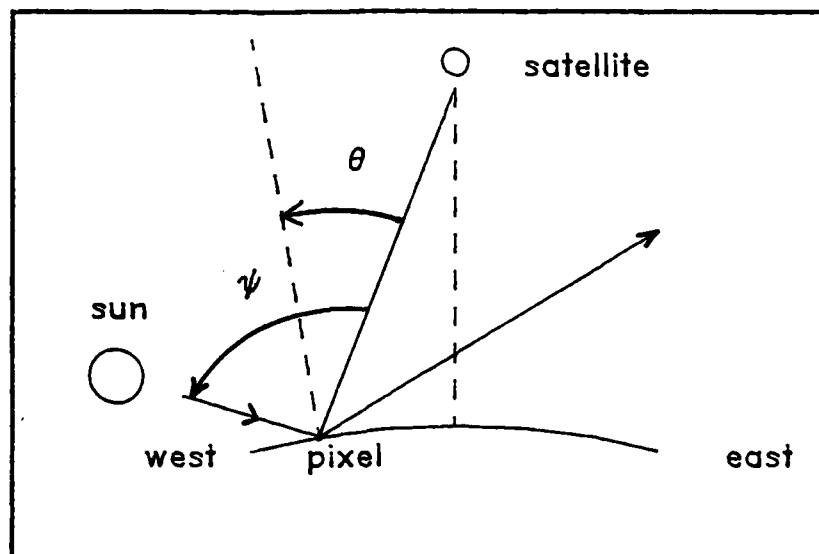
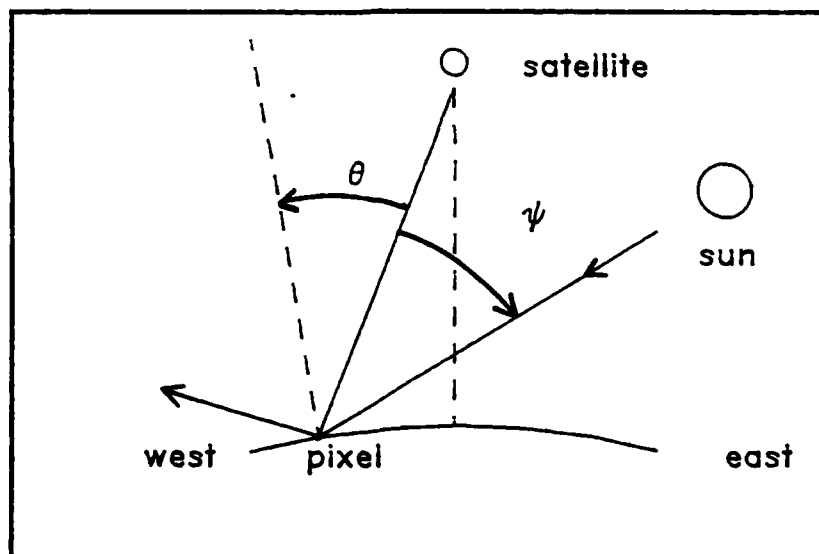


FIG.4.3 CHANNEL 4, COS (THETA) AND WIND SPEED

For a series of images in July, mean channel 4 temperatures, the cosine of the satellite viewing angle and the wind speed are plotted versus the day of the observations. The viewing angle, θ , is defined in Figure 4.4. Note the correlation between mean temperature and the viewing angle.



a) evening



b) morning

FIG. 4.4 SATELLITE VIEWING ANGLE GEOMETRY

The viewing geometry of the sun, the satellite and the region scanned is defined for a) evening and b) morning. The viewing angle, θ , is the angle between the satellite and a line normal to the surface and is positive in the figure. The angle, ψ , defines the sun-satellite-sea surface geometry (after Bernstein, 1982).

Table 4.1 Predictive Skill for CODE Data

form of prediction	coefficients		artificial skill, %	prediction skill, %
	α	β		
$T_s = \alpha T_3$	0.29	--	1	15.4
$T_s = \beta T_4$	--	0.41	1	25.0
$T_s = \alpha T_3 + \beta T_4$	0.08	0.36	2	25.5

$$\langle T_s^2 \rangle = 0.93, \quad \langle T_3^2 \rangle = 1.66, \quad \langle T_4^2 \rangle = 1.35, \quad \rho_{T_3, T_4} = 0.67$$

Skill of each channel separately and together for predicting the thermistor temperatures in the CODE array. The variable must contribute more to the prediction skill than the artificial skill for the variable to be a good predictor. The addition of channel 3 to the prediction using channel 4 alone is not significant because the additional prediction skill is only half the additional artificial skill. Channel 3 has some predictive skill because it is well-correlated with channel 4: the correlation coefficient is 0.67.

Table 4.2 Predictive Skill for Bernstein's Data

form of prediction	coefficients		artificial skill, %	prediction skill, %
	α	β		
$T_s = \alpha T_3$	1.15	--	2.5	98.4
$T_s = \beta T_4$	--	1.41	2.5	87.5
$T_s = \alpha T_3 + \beta T_4$	1.38	-0.31	5	98.7

$$\langle T_s^2 \rangle = 24.1, \quad \langle T_3^2 \rangle = 17.9, \quad \langle T_4^2 \rangle = 10.7, \quad \rho_{T_3, T_4} = 0.96$$

Skill of each channel separately and together for predicting the in situ temperatures in Bernstein's data. The addition of channel 4 to the prediction using channel 3 alone is not significant because the additional prediction skill is much less than the additional artificial skill. Channel 4 has some predictive skill because it is well-correlated with channel 3: the correlation coefficient is 0.96. Note that the variance in the sea-surface temperatures to be predicted, T_s , is much larger for Bernstein's data than for the CODE data, as shown in Table 4.1.

Table 4.3 Mean Differences for Image Pairs

image 1	image 2	$\delta T, ^\circ\text{C}$		common area, pixels
		channel 3	channel 4	
117A	118	-0.02	0.85	80,325
123A	124	-0.82	1.28	19,275
126	126A	1.05	0.11	40,950
126A	127	-0.76	0.16	38,900
127	127A	0.92	-0.69	23,525
130A	131	-2.10	-0.18	53,050
131	131A	1.06	-0.85	83,300
131A	132	-0.87	1.04	75,050
140	140A	0.57	-0.74	23,250
153A	154	0.17	1.27	93,400
174A	175	-1.62	0.14	40,550
175	175A	1.31	-0.07	18,975
179A	180	-0.98	0.62	123,250
187A	188	-2.72	-0.32	26,925
188	188A	0.57	-0.28	86,375
188A	189	-0.39	0.56	117,375
189	189A	-0.10	-1.31	131,400
189A	190	0.62	0.88	127,175
192	192A	1.11	-0.08	83,975
193A	194	-0.13	1.12	27,400
95	96	0.02	0.21	28,225
121A	122A	-1.57	-0.82	19,925
122A	123A	0.82	-1.88	17,950
126	127	0.35	0.18	50,525
126A	127A	0.24	-0.58	18,625
130A	131A	-0.95	-1.04	35,675
131	132	0.19	0.15	115,200
165	166	1.33	1.71	84,025
178A	179A	-1.89	-0.35	73,450
187A	188A	-2.18	-0.61	27,500
188	189	0.23	0.23	101,475
188A	189A	-0.50	-0.71	109,225
189	190	0.48	-0.46	148,925
190	191	-2.27	-1.21	121,000
191	192	1.05	1.10	103,750
192A	193A	0.12	-0.78	23,925
194	195	1.16	-0.07	102,275
195	196	-1.77	0.24	26,450

Differences in the mean value for each channel between the images whose year days are given in the first two columns. Images followed by an A are morning data. The days are based on GMT so that, e.g., image 127 precedes image 127A. The mean difference was computed over the common clear area, the size of the common area is given in pixels. Each pixel is approximately 1 km².

Table 4.4 Statistics of Image Differences

data type (time separation)	number of pairs	rms difference, °C.	
		channel 3	channel 4
morning/evening (12 hours)	20	1.11	0.76
morning (24 hours)	8	1.26	0.95
evening (24 hours)	10	1.14	0.78

The mean differences in Table 4.3 were grouped according to the type of data, morning or evening, and mean values for the mean differences were computed for each channel. Note that the mean difference between pairs is larger for channel 3 than for channel 4 for all data types.

Table 4.5 Distance of Image from Satellite Subtrack

day	distance, degrees longitude	viewing angle, degrees	channel 3 hazy?
86A	3.5 W	19	no
95	7.5 E	-36	
96	2.0 E	-11	
103A	1.5 E	-8	no
117A	3.5 W	19	no
118	3.0 E	-16	
120	9.0 W	41	no
121A	1.0 W	6	no
122A	6.0 W	30	no
123A	12 W	50	no
124	6.5 W	32	
126	7.0 E	-34	
126A	3.5 W	19	no
127	1.5 E	-8	
127A	9.5 W	43	no
130A	1.5 W	8	no
131	3.5 E	-19	
131A	7.0 W	34	no
132	2.0 W	11	
133	7.0 W	34	
140	2.0 E	-11	
140A	8.0 W	38	no
148A	3.5 W	19	no
153A	6.5 W	32	no
154	1.5 W	8	
155A	1.0 E	-6	yes
160A	4.0 E	-21	yes
161	8.5 E	-40	
162A	7.5 W	36	no
165	11.0 E	-47	
166	5.0 E	-26	
168	6.5 W	32	
169A	1.0 E	-5.6	yes
173	10 W	44	
174A	1.0 W	5.6	no
175	4.0 E	-21	
175A	6.0 W	30	no
177A	7.0 E	-34	yes
178A	1.0 E	-5.6	no
179A	4.0 W	21	no
180	0.5 E	-2.8	
184A	12.5 W	51	no
187A	0	0	no
188	5.0 E	-26	
188A	6.0 W	30	no

Table 4.5 (cont'd.)

day	distance, degrees longitude	viewing angle, degrees	channel 3 hazy?
189	1.0 W	5.6	
189A	11.0 W	47	no
190	7.0 W	34	
190A	8.0 E	-38	yes
191	13.5 E	-53	
191A	3.0 E	-16	yes
192	8.0 E	-38	
192A	3.5 W	19	no
193A	9.0 W	41	no
194	4.0 W	21	
195	10 W	44	
195A	5.0 E	-26	yes
196	11.0 E	-47	

For each image, designated by its year day, the approximate distance of the center of the image from the satellite subtrack is shown in degrees longitude, east or west of the subtrack. The viewing angle, θ , is defined in Figure 4.4. Channel 3 of many images recorded in the morning had a hazy appearance with no recognizable ocean features, while the channel 4 image was relatively cloud-free. Note that the morning images which were hazy correspond to a negative viewing angle, or the CODE region was to the east of the subtrack, the sun side, as shown in Figure 4.4.

AD-A135 462

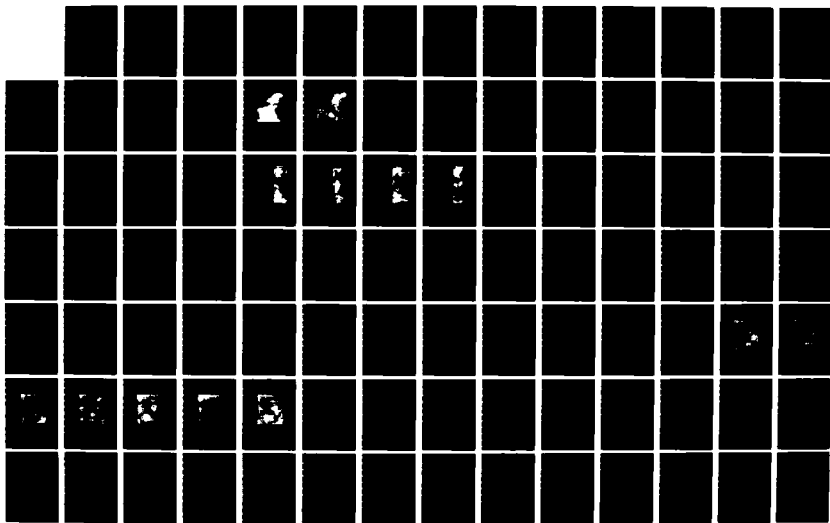
SWIRLS AND PLUMES OR APPLICATION OF STATISTICAL METHODS 2/3
TO SATELLITE-DERIVED (U) SCRIPPS INSTITUTION OF
OCEANOGRAPHY LA JOLLA CA K A KELLY AUG 83

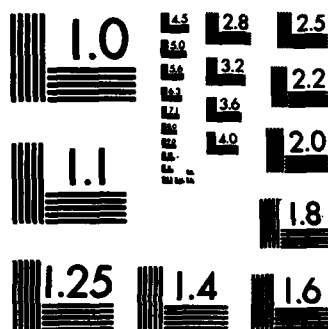
UNCLASSIFIED

SIO-REF-83-15 N00014-80-C-0440

F/G 8/10

NL





MICROCOPY RESOLUTION TEST CHART
NATIONAL BUREAU OF STANDARDS-1963-A

Table 4.6 Estimation of Time-Varying Means
Using Powers of the Viewing Angle

quantity estimated	skill for estimator, %				artificial skill, %
	1	$\bar{\theta}$	$\bar{\theta}^2$	$\bar{\theta}^3$	
$\frac{\delta T_4}{\delta \theta}$	9	75	17	62	2.5
$\frac{\delta T_3}{\delta \theta}$	38	2	13	< 1	2.5
$\frac{\delta T_3}{\delta \theta}$, evening	82	21	62	8	10
$\frac{\delta T_3}{\delta \theta}$, morning	48	61	64	58	11
$\frac{\delta T_3}{\delta \theta}$, morning- evening	2	38	23	27	5

Variations in the mean temperature of each channel with changes in the viewing angle, θ , were regressed against powers of the viewing angle. The results are shown as estimation skill for each power of θ . The pair of estimators with the highest individual skill were tested together for skill. No pair of estimators showed a significant increase in skill over the best individual estimator.

Table 4.7 Effect of Viewing-Angle Corrections on Estimation Skill for Point Measurements

estimator	data type	skill, %	artificial skill, %
T_4	all	25	< 1
T_4	morning	36	2
T_4	evening	21	1.5
T_3	all	15	< 1
T_3	morning	17	2
T_3	evening	20	1.5
$T_4 + C(\theta)$	all	28	2
$T_4 + C(\theta)$	evening	22	3
$T_3 + C(\theta)$	evening	39	3
T_3 and $T_4 + C(\theta)$	evening	42	6

Estimation skill for channels 3 and 4 for predicting thermistor temperatures, with and without viewing-angle corrections. The total artificial skill for each estimator is shown for comparison with the computed skill, the artificial skill includes a term for the viewing-angle corrections, where the corrections were used. Conclusions are discussed in the text.

CHAPTER 5

SPATIAL AND TEMPORAL VARIABILITY

The goal of this chapter is to present a simple statistical description of the data. This description is complicated by 1) the patchiness of the data and 2) the large size of the data set. The patchiness of the AVHRR data in both space and time, illustrated in Figure 2.2, makes even the simplest of statistics a complicated problem of definitions. To make matters worse the data are biased toward certain weather events (periods of calm generally coincided with heavy cloud cover) and toward certain parts of the ocean (dense clouds hovered about 300 km offshore on even the clearest days). The second problem, the large volume of data, means that each computation is expensive in computer time.

5.1 Problems in Defining Statistics

To illustrate the problem of defining statistics for patchy data, let us look at the simplest statistic, the mean or expected value of the temperature, $T(x,t)$, which is a function of space and time. The mean is usually defined as

$$\langle T(x) \rangle = \frac{1}{N} \sum_{n=1}^N T(x, t_n) \quad (5.1)$$

For an unbiased mean one would normally average over many values of T from equally-spaced times, t_n , or use only independent samples of T . To get independent samples one must first compute a decorrelation time to

know how to sample T . The problem of subtracting the mean before computing the time-lagged autocovariance can be circumvented by using the structure function, $S(x, \delta t)$, where

$$S(x, \delta t) = \langle [T(x, t) - T(x, t + \delta t)]^2 \rangle \quad (5.2)$$

which for a stationary series reduces to

$$S(x, \delta t) = 2 \left[\langle [T'(x, t)]^2 \rangle - \langle T'(x, t) T'(x, t + \delta t) \rangle \right] \quad (5.3)$$

where T' is the temperature anomaly

$$T'(x, t) = T(x, t) - \langle T(x) \rangle .$$

The first term in 5.3 is the variance of T and the second term is the time-lagged autocovariance. Some systematic errors in the AVHRR temperatures, as discussed in Chapter 4, may contribute a substantial error to the computation of $S(x, \delta t)$. The spatially-averaged temperature varied over short times, i.e.,

$$\langle [\overline{T(t)} - \overline{T(t + \delta t)}]^2 \rangle \approx 0.7 \text{ C}^2$$

for δt as small as 12 hours, suggesting that there were systematic errors from image to image. This apparent temperature change was reduced by $\sim 75\%$ by using a crude viewing-angle correction, but there was probably a residual systematic error.

Assuming that a decorrelation time, $\tau(x)$, has been computed for any location, one then picks independent measurements by sampling at times longer than the decorrelation time. Because the images occurred in clumps of a few days, if $\tau \geq 3$ days, only a few independent samples can be taken. To use more of the data, a weighting scheme can be devised to average dependent samples. However each spatial point, x , has a different distribution of measurements in time so one needs a complicated bookkeeping scheme for weighting approximately 150,000 spatial points. One also must determine a minimum number of samples required to get a sensible mean because some areas were under the clouds so often that a mean value for T would have to be computed from a couple of samples in July.

5.2 Reducing the Amount of Data

The first task I chose was to compact the data set to reduce the computations required in subsequent analyses. The goal of the data reduction was to eliminate noise by averaging without destroying the signal. In this case averaging consisted of replacing an $m \times m$ subset of an image by the subset's average value. The signal was defined to be variations which are correlated between images at the shortest spacing in time, 12 hours; variations with time scales shorter than the sampling rate cannot be resolved in most analyses. The noise is then defined as variance which is not part of the signal. The spatial resolution of the images (1 km) is better than the temporal resolution because a small temperature feature can easily move more than 1 km in twelve hours with typical surface velocities of 20 km day^{-1} . To reduce the data I needed

to find the spatial resolution corresponding to the twelve-hour sampling rate; the averaging length scale could then be chosen as any convenient number smaller than this necessary resolution. Four pairs of images from the July series were selected for this analysis and the simple mean of the images was removed. The images were averaged over a sequence of successively larger boxes; for each box size the variance of each image and the correlation for each pair were computed as follows:

$$\text{var}(t) = \frac{1}{N'} \sum_{i=1}^{N'} [\bar{T}(x_i, t)]^2 \quad (5.4)$$

$$\rho(t_1, t_2) = \frac{1}{N'} \frac{\sum_{i=1}^{N'} \bar{T}(x_i, t_1) \bar{T}(x_i, t_2)}{[\text{var}(t_1) \text{var}(t_2)]^{1/2}} \quad (5.5)$$

where \bar{T} is the average value for the box, N is the total number of (clear ocean) pixels in the image, and

$$N' = \frac{N}{m^2}$$

is the number of boxes of dimension m in the image. The results, shown in Figure 5.1, show that the variance decreases with an increasing box size: because the mean has been removed the variance approaches zero as the box size approaches the image size. The correlation also tends to zero in the limit of large m . The correlation is a measure of the signal-to-noise ratio because it is the ratio of the covariance to the variance. The correlation increases up to a 10-pixel box dimension and then decreases so that the maximum signal-to-noise occurs for 10 km x 10 km boxes. Thus at a 12-hour separation in time temperature features of

less than 10 km in diameter are uncorrelated and are noise for this time series; i.e., no signal is lost by averaging over them.

A feature which moves its own diameter in 12 hours will not contribute to the correlation between images: for features 10 km in diameter this corresponds to an advection speed of 20 km/day ($\approx 23 \text{ cm s}^{-1}$). For this speed features larger than 10 km will be correlated between images and features smaller than 10 km will not be correlated. Features smaller than 10 km are apparent in most images and can sometimes be followed by eye through a series of several images. These small scales may contain important information; however, this information will not contribute to those statistics which involve average correlations in time because small features are aliased at this temporal sampling rate. Small features are discussed further in section 5.5.

A somewhat smaller box size, 5 km x 5 km, was chosen for averaging the data; these spatially-averaged data were used in most subsequent calculations discussed in this chapter and in Chapter 7.

5.3 Decorrelation Time

The next task was to find a decorrelation time and from it, a weighting scheme for computing an expected value. The structure function was computed for the July series of images; it was spatially-averaged over the clear area common to 12 images and, to approximate the expected value operation, it was also averaged over several pairs of images for each time lag. The structure function was computed for two cases to find bounds for the function: 1) for the images with the

viewing-angle correction described in Chapter 4, and 2) for the images with constants added so that the spatially-averaged temperature was constant through the series (7.5 days). The second case allows no variations from either systematic errors or from real changes in the spatially-averaged temperature and yields the structure function which is due only to the temperature patterns changing in time. The first case includes the contribution from changes in the spatially-averaged temperature and any remaining systematic errors. The structure functions for these two cases are shown in Figure 5.2. The residual error after the viewing-angle correction was made is about $0.18 \text{ } ^\circ\text{C}^2$, approximately the difference between the two curves at the smallest time lag. The curves diverge slightly at larger time lags, indicating that the spatially-averaged temperature does change slowly because systematic errors do not depend on the lag. The structure function for which the spatial average was not allowed to vary is considerably smoother; however, the curves have essentially the same shape. Fortunately, variations due to changes in the temperature patterns are larger than variations due to the spatial means or to the residual viewing-angle error, meaning that the errors are not masking structure of the autocovariance, which is needed for subsequent computations.

The structure function contains some information necessary for further analyses on the images. If in equation 5.2 the measured temperature is given as

$$T(x, t) = T_g(x, t) + \epsilon \quad (5.7)$$

where T_s is the actual SST and s is the error in the measurement, then equation 5.2 becomes, after averaging over x ,

$$S(\delta t) = 2 [\langle T_s'^2 \rangle - \langle T_s'(t) T_s'(t + \delta t) \rangle + \langle s^2 \rangle] \quad (5.8)$$

In the limit as $\delta t \rightarrow 0$, $S(\delta t)$ gives an estimate of the noise level of the data, $\langle s^2 \rangle$, which can be visualized as the variance between two images taken simultaneously by two identical satellites. Only when the structure function, $S(\delta t)$, significantly exceeds $2 \langle s^2 \rangle$ are images distinctly different. Because the structure function rises steeply at the shortest time lag, another indication that the images are undersampled in time, the noise level is difficult to estimate. Assuming that

$$2 \langle s^2 \rangle \approx S(0.5 \text{ day})$$

then images become different at 1.5 - 2 days. At time lags of 0.5 - 1.0 day, the images are sufficiently similar that they can be combined for a composite image. The structure function starts to level out at a time lag of 4-5 days, the decorrelation time needed for the weighting scheme.

5.4 Mean and Variance

Using this decorrelation time as a guide, the images were grouped into blocks of four days and an average image was computed for each four-day block by averaging over all available data at each spatial point. Eighteen such average images were computed. These four-day images were again averaged over the available data at each spatial

point. Points for which there were contributions from at least half the averaged (independent) images were used to create the mean shown in Figure 5.3. In this figure cold areas are shown as light shades of gray and warm areas by dark shades. The range of temperatures represented by the gray shades is 8.5 to 14 ° C. This mean indicates the sea surface is colder near the coast everywhere except near the San Francisco Bay and it is coldest on the south side of Cape Mendocino.

This mean was subtracted from each image (where data were available) and the variance was computed in the same way, by first averaging over four-day groups. The variance is shown in Figure 5.4, where high values are denoted by dark shades and low values by light shades. The range of variance spanned by the gray shades is from 0.6 to 3.2 C². The variance map shows a different distribution than the mean with longshore variations predominating. The regions of highest variance are in the north near the Oregon border and in the south near San Francisco Bay. The high variance for these areas can be interpreted as the expansion and contraction of the large cold upwelling area depicted in the mean, i.e., sometimes these regions are part of the strong upwelling regime indicated by the mean and sometimes they are part of a warmer regime to the north or south. To a lesser extent a region extending offshore of Pt. Arena has a high variance as does a region offshore of Cape Mendocino. The CODE array was located in a cold area with low variance in the SST's.

Longshore averages of both the mean and variance were computed as a function of offshore distance. These values are shown in Figure 5.5, along with the profiles of the mean and variance near the center of

the CODE array. The average variance reaches a peak at about 70 km offshore very near the break in the offshore gradient of the mean temperature at about 90 km and decreases monotonically, but not very rapidly, after 70 km offshore. The actual offshore variance may be lower than is shown in Figure 5.5b because the offshore areas had more cloud contamination than the nearshore areas and because the difference between cloud temperatures and the water is larger for the warmer offshore regions. Although in many images there is a strong temperature gradient between 50-100 km offshore, parallel to the coast, this is not reflected in either the variance map or Figure 5.5b as a large local increase in variance. This diffuse peak in the variance probably results from the large excursions of this front in the cross-shore direction in time and from the meanders of the front in space. The spatial variations in the SST variance can be seen by comparing the longshore-averaged profile of variance with the profile for the CODE region in Figure 5.5b. While on average the variance increases with offshore distance, the variance in the CODE region decreases until about 120 km offshore, then increases abruptly. From Figure 5.4 this increase can be seen as an extension of the high variance region originating at Pt. Arena which is the result of the cold plumes which are frequently found there. The CODE region appears to be sheltered from the energetic meanders of the California Current which move farther offshore between Pt. Arena and Pt. Reyes.

5.5 Wavenumber Spectra

The coastal boundary creates a distinct inhomogeneity in the cross-shore direction which can be seen as a reduction in variance offshore; however, an argument can be made for an approximate homogeneity in the longshore direction. With this assumption, one-dimensional estimates of wavenumber spectra were computed from several images for each of four regions. Using very clear images every fourth column of the original (unaveraged) image arrays was Fourier-transformed and the Fourier magnitudes computed. The magnitudes were averaged over all columns in each region and over all images used. The results are shown in Figure 5.6 as a log-log plot of power spectral density versus wavenumber. The spectra are offset vertically for clarity, where the vertical axis is appropriate for region A. Each region was defined by its approximate distance offshore as follows :

- i) region A, 0-80 km
- ii) region B, 80-160 km
- iii) region C, 160-240 km
- iv) region D, 240-320 km

The spectra are all red with no obvious peaks at higher wavenumbers; peaks in region D are due to the smaller data volume available for computing the spectrum. Confidence intervals were not computed because the columns used for averaging were highly-correlated. The spectra are quite similar; however, region C may have a slightly different distribution of energy with less at the very lowest wavenumbers and more energy at wavelengths of about 35 km.

These spectra are not a particularly revealing way of describing the images which look quite different in time and in space; but perhaps the spectrum is changing in time. Certain images have smooth sharp fronts while others have more diffuse fronts and small shear eddies; these different characteristics may indicate different physical processes. To determine whether this difference could be described by a longshore spectrum, the previous procedure was repeated on two pairs of images, but only regions from a single image were averaged. The images in one pair were separated by six days; the others were separated by seven days. In both cases mean wind speed increased by more than 50 % from the first image to the second image in the pair. In both cases there is a decrease in spectral energy at small scales (~ 5 km). At first sight this tendency seems inconsistent with the appearance of the images. The first image in each pair had relatively strong smooth temperature fronts; the second image had more irregular fronts and more small-scale features. However, the sharp fronts in the first image may have contributed more to the high wavenumber energy than the small features in the second image.

There may be a quantifiable difference in the small-scale features that is correlated with the wind speed; if so, a better measure is needed that takes account of the coherence of the small scales, i.e., it would need to distinguish between small eddies and the sharp edges of a larger feature. An analysis of a digital picture by Oppenheim and Lim (1981) showed that phase information was more important in reproducing an image from its Fourier transform than the magnitudes. Oppenheim and Lim compared an image reconstructed from the exact Fourier magnitudes

and zero phase with an image reconstructed from unity magnitude and the exact phase information; they found that while the former was unrecognizable, the latter clearly resembled the original. They concluded that to get a reasonable reconstruction of an image one could use the magnitudes from another image, but that the exact phase information was essential. This suggests that to describe statistically the differences that can be seen in the original images, one needs to develop a statistic which does not average phase information. For larger scales the relationship between coherent structures and the winds can be examined by using empirical orthogonal functions. This analysis is discussed in Chapter 7. The EOF's preserve both the local phase information (the shapes of features) and their location in space (with respect to topography). However, the EOF's cannot describe the small-scale variations in temperature because the very smallest scales are aliased at the 12-hour time intervals and because the large-scale features dominate the variance.

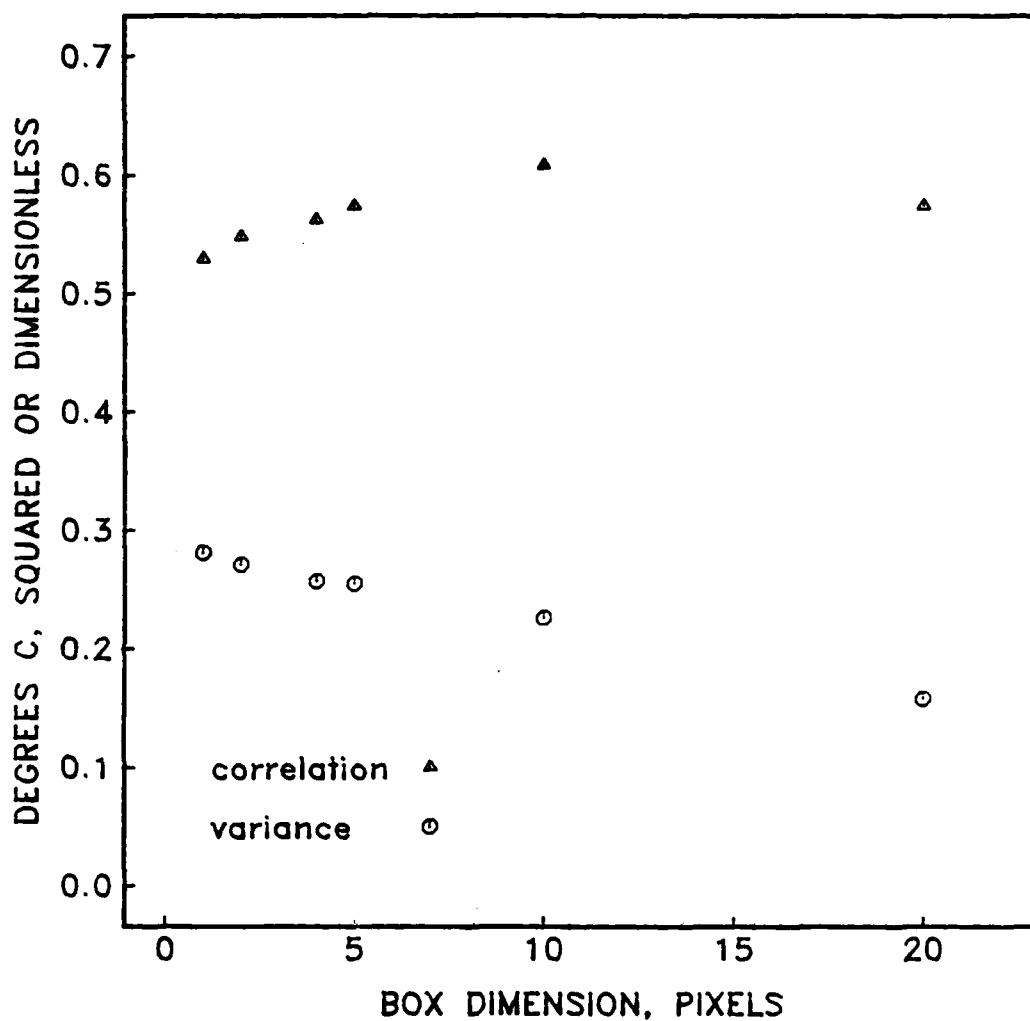


FIG. 5.1 CORRELATION AND VARIANCE FOR IMAGE PAIRS

To find the spatial resolution comparable to the fixed temporal resolution of 12 hours, several images were averaged over successively larger boxes. The variance of the images and the correlation between pairs of images is plotted against the box size. The correlation maximum at 10 pixels corresponds to the spatial resolution.

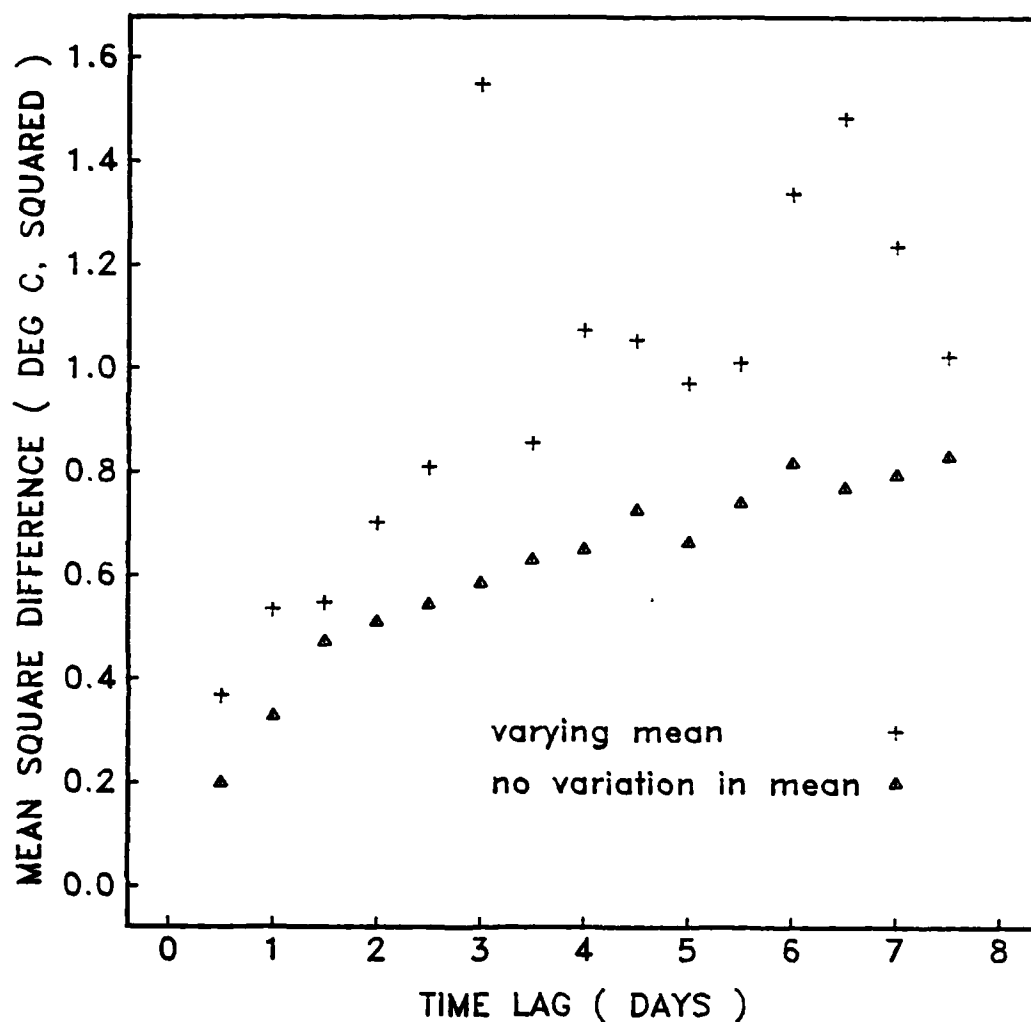


FIG. 5.2 STRUCTURE FUNCTION FOR JULY IMAGES

The spatially-averaged structure function for various time lags for two cases which bound the actual function. The case for which there is no variation in the mean gives the function only for temperature patterns changing in time. The other case allows the mean to change but also includes spatially-constant errors.



FIG. 5.3 MEAN SEA SURFACE TEMPERATURE

Computed by weighting more than fifty images which were grouped into 18 independent measurements based on a decorrelation time of four days. The coastline is shown in black. The mean was not computed for the white area at the left which had fewer than nine independent measurements. Values less than 8.5 C are white; values greater than 14 C are black. For locations refer to Figure 1.1.

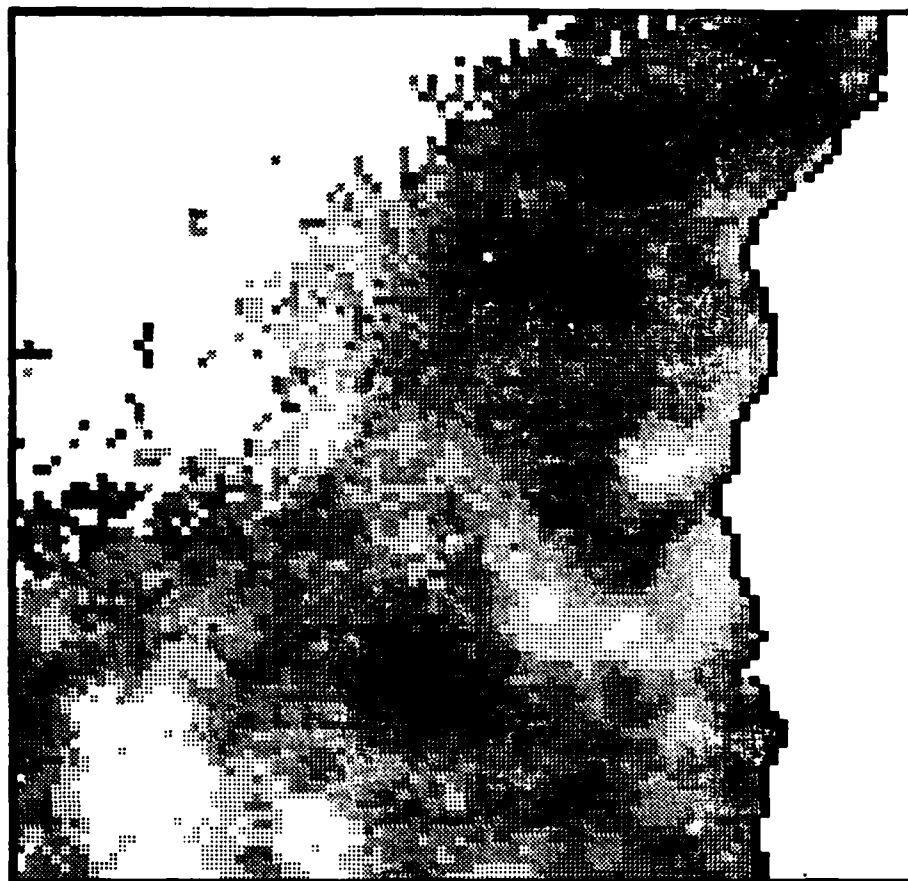


FIG. 5.4 VARIANCE IN SEA SURFACE TEMPERATURE

Computed as in Figure 5.3, after the mean was removed. Values less than $0.6\text{ }^{\circ}\text{C}^2$ are white; values greater than $3.2\text{ }^{\circ}\text{C}^2$ are black. The white area in the lower left corner has low variance; variance for the upper left corner was not computed. Note high variance regions at upper right (near Crescent City) and lower right (San Francisco Bay).

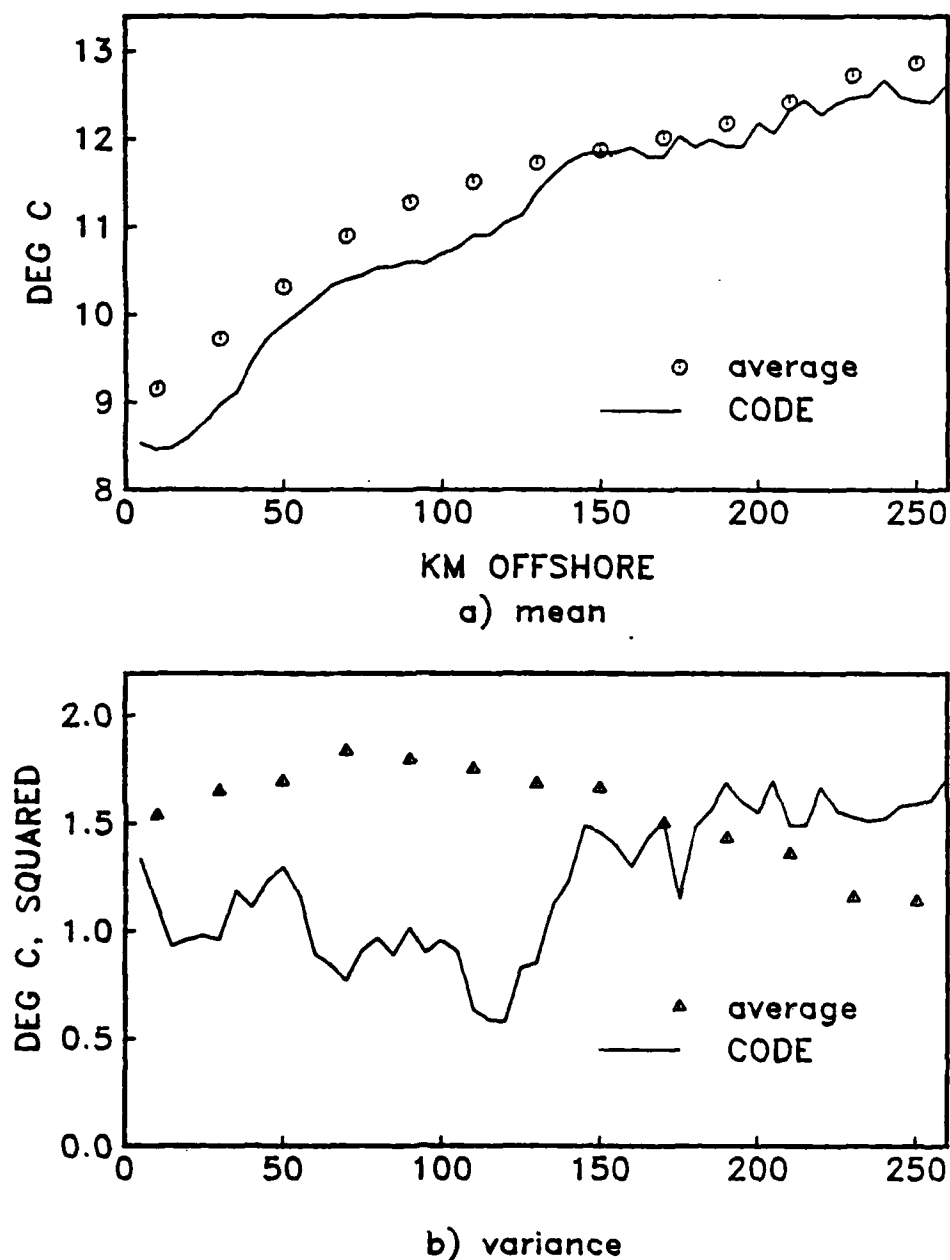


FIG.5.5 MEAN AND VARIANCE IN CROSS-SHORE DIRECTION

Profiles of the a) mean and b) variance from Figures 5.3 and 5.4. Symbols denote profiles which have been averaged in the longshore direction. Solid lines are the profiles through the center of the CODE array. The CODE array had a typical temperature profile, but unusually low variance.

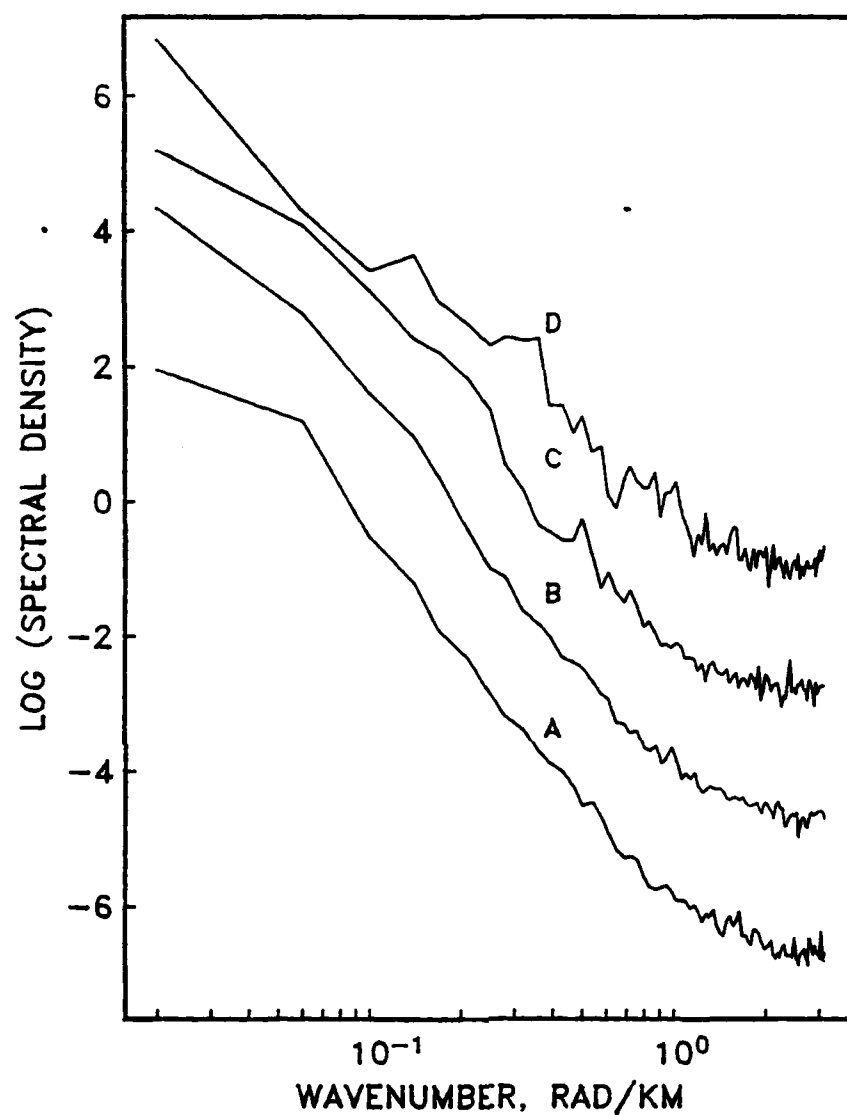


FIG. 5.6 LONGSHORE WAVENUMBER SPECTRA

One-dimensional spectra in the longshore direction for regions which were increasingly farther from the coast. Region A (adjacent to the coast) is plotted with the correct y-axis. Other plots are offset for clarity. The data used for the spectra were well-correlated making error estimates large. Error estimates are not shown.

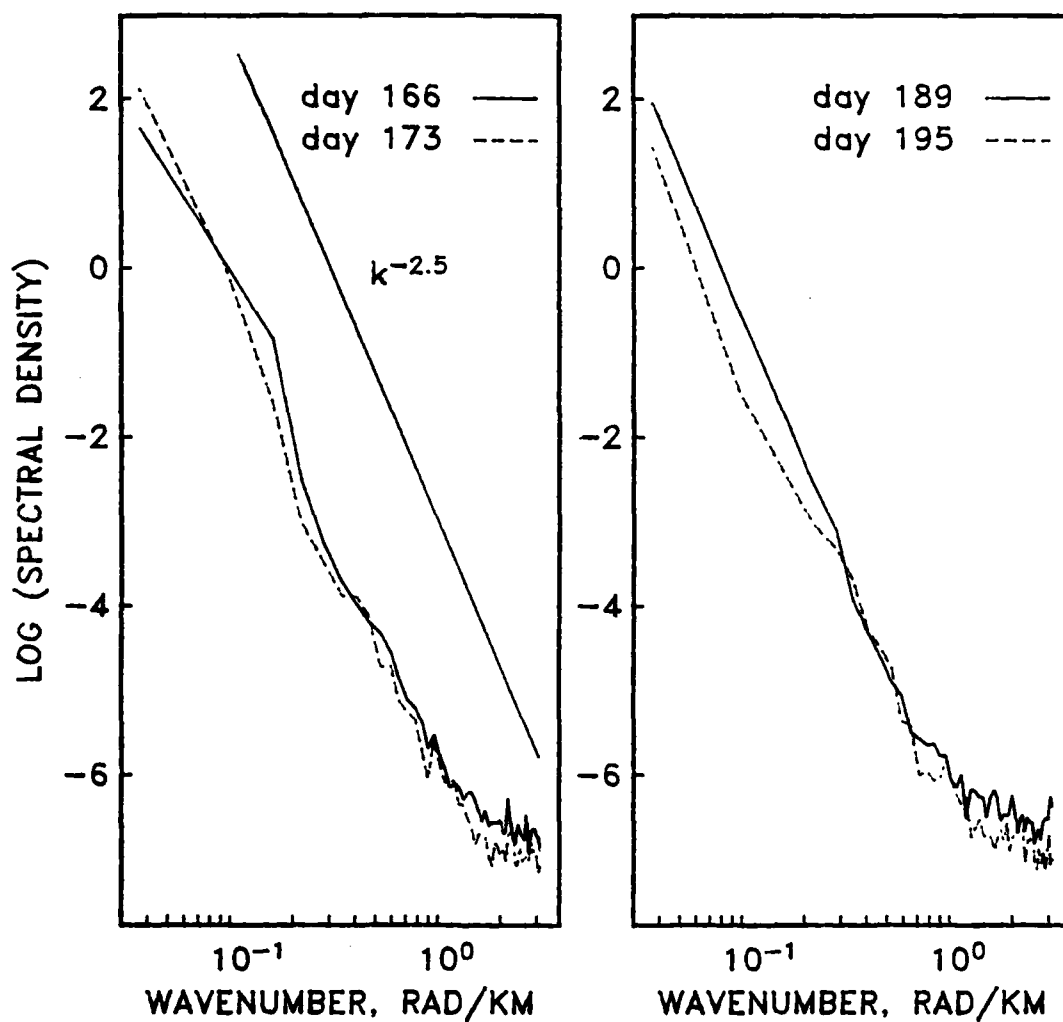


FIG. 5.7 WAVENUMBER SPECTRA FOR PAIRS OF IMAGES

Spectra for images separated by six or seven days. Mean wind speeds for the second image in each case (dotted lines) were 50% greater than for the first image (solid line). Note the decrease in energy at high wavenumbers. Changes at low wavenumbers are not significant.

CHAPTER 6

COMPARISON OF SATELLITE IMAGES WITH OTHER CODE DATA

Although the AVHRR measures only infrared radiance from the ocean's surface, the satellite images described the surface velocity field surprisingly well. Strong winds, a deep mixed-layer, barotropic current fluctuations and a simple T-S relationship combined to make the satellite SST maps good predictors of the upper 100 m of the ocean. This chapter briefly describes some of the other measurements taken during CODE-1 to establish that the SST analysis in Chapter 7 has implications for the geostrophic near-surface currents and that the simple model for estimating velocities in Chapter 8 is consistent with in situ measurements. The in situ data also illustrate the limitations of the satellite description.

6.1 Hydrographic Data

Two hydrographic surveys were conducted during CODE-1: Leg 4 from 25 April to 7 May 1981 and Leg 7 from 1 to 14 July 1981. The surveys were conducted using the Oregon State University R/V Wecoma under the direction of Adriana Huyer. Results of each survey are contained in an OSU data report (Fleischbein, et al., 1982) and (Olivera, et al., 1982). The second survey was the subject of a Master's thesis by R. M. Olivera (1982); his results will be summarized here.

The first survey was confined to the shelf and the inner slope so comparisons with the larger scale satellite images are less useful than for the second survey. In late June the cloud bank over northern

California moved offshore to reveal a well-defined cold plume about 200 km long extending offshore at the CODE site. Using the images which I sent to the ship with the Scripps' participants and the NESS/Redwood City SST maps, the survey was designed to sample this plume in addition to the stations within the CODE array.

Maps of SST, surface salinity and density were constructed from CTD measurements for Leg 4 from just north of Pt. Arena to the southern end of the CODE array. Agreement with the satellite images was good for both the location of the temperature fronts and the magnitude of the gradients. The channel 3 images had temperatures about 0.5 to 1° C. colder than the CTD-derived maps. Surface salinity maps for the same dates and region showed features similar to those in the temperature field with salinity decreasing offshore as temperature increased. Because of the consistent relationship between salinity and temperature, maps of density looked much like the SST maps. Maps of dynamic height showed evidence of a countercurrent for 200/500 db. All maps showed stronger gradients in the vicinity of Pt. Arena.

Vertical profiles of salinity, temperature and density showed that near the coast (to depths of about 150 m) the water column was well-mixed to the bottom; offshore of the CODE array, over the slope, the depth of the mixed layer was about 50 m decreasing to only about 20 m offshore of Pt. Arena. As shown in Figure 5.4 the SST had low variance at the CODE array where the mixed layer was deepest and much higher variance near Pt. Arena where the mixed layer was quite shallow.

Winds measured at the ship were generally southward about 40 km offshore, turning eastward to parallel the coast farther inshore. Thus winds were about 15° offshore south of Pt. Arena. Winds were weak within 10-15 km of shore and were strongest in the afternoon and early evening. The curl of the wind stress south of Pt. Arena would enhance the upwelling in this region by Ekman pumping and is consistent with the mean SST field shown in Figure 5.3, which shows this area to be consistently cold.

The second survey established that the cold plume visible at the surface was recognizable at depths of 100 m and that it was associated with large dynamic height anomalies. Salinity and density fronts generally corresponded to temperature fronts; all fronts were strongest at the surface and increased with distance offshore.

Olivera (1982) interpreted the survey as a picture of a meandering geostrophic current which was the boundary between two water masses. The warm, fresh water was from the Columbia River and the cold, salty water was of subsurface origin, except near Half Moon Bay, where there was a different type of water, which was warm and salty. Temperature and salinity had a correlation of -0.73 at the surface, dropping to -0.65 at 100 db, and negligible correlation at 200 db.

The agreement with satellite images was good and was probably limited primarily by the motion of temperature patterns during the several days required to make a hydrographic survey. Fronts at depth generally coincided with surface fronts except at the northern edge of the cold plume where the density front was shifted about 10 km further

north at 50 db. The warm water north of the plume extended further south at depths less than 100 db; at 100 db there was no warm anomaly. Temperature and salinity fronts were about 50% weaker at 50 db. The T-S relationship at the CODE array was similar to that at 80-160 db at 100 km offshore, except that it was about 0.5° C. warmer, indicating the water may have upwelled from that depth and been warmed by the sun.

Dynamic height anomalies correlated well with temperature at depths of up to 200 db, but correlated well with salinity only at the surface where there were strong gradients. A current meander resulted in northward flow about 80 km offshore. This flow extended from the surface to more than 300 db. There was evidence of a deep counter-current over the slope north of Pt. Reyes.

6.2 Current Meter Records

A heavily-instrumented array of current meters was deployed by Clinton Winant and Robert Beardsley. The location of the moorings is shown in Figure 6.1; a description of the array configuration and the instruments is contained in the data report (Winant and Bratkovich, 1983).

The velocity records were dominated by highly-barotropic longshore currents. Longshore was defined as parallel to local isobaths; northward as used in this chapter means along the y-axis at 317° T. The longshore near-surface velocities were the most energetic; particularly at C3, C4, and M3 within the upper 20 m. All of the moorings had longshore fluctuations in velocity in phase from the shallowest

current meter (at 4-9 m depth) to the deepest (within about 20-50 m of the bottom). The near-surface velocities were on average southward and there was a mean vertical shear so that the mean velocity at depth was northward. The barotropic structure of velocity fluctuations gives greater importance to measurements at the surface, such as the satellite data, because the surface field can be used to infer motion in the entire water column.

In the cross-shelf direction there was a mean offshore flow in the surface layer, becoming more onshore with depth, which is the classical upwelling profile. However, there was a net offshore flow for the entire CODE array. This created a mass balance problem; the solution was probably a return flow to the north and/or south. Point Arena is a likely area for this return flow with its highly-variable SST's and its shallow mixed layer. The most energetic cross-shelf record was at C5 where the variability exceeded that at C4 by a factor of three. This mooring was over the slope where it must be less constrained by the coastline and more influenced by velocity structures in the deeper ocean. This is consistent with the increase in SST variability offshore of the CODE array as shown in Figure 5.4.

There were several northward events in the predominately southward velocity records. These events generally coincided at several moorings; northward flow at C5 usually coincided with onshore flow to give a classical downwelling event. At C5 these events were centered on days 106, 117, 125-127, 143-146 and 190-200. These were generally also times of calm winds and heavy cloud cover so they were not well-represented by the satellite images (cf. Figure 2.2).

At the southern end of the CODE array the single mooring R3 showed evidence of a different flow regime toward Pt. Reyes. Mean longshore flows at R3 were southward but with much smaller magnitudes than those on the C-line. In contrast to the other moorings there was only a single large southward event from day 121-128.

The mismatch in spatial scales limits direct comparisons between current meter data and the satellite images. The deep mixed layer and the barotropic current structure explain why SST variance was so low at the CODE array. The satellite images suggested that the currents outside the CODE array were quite different; this information was used to extend the current meter array to Pt. Arena for CODE-2.

6.3 Doppler Log and Surface Drifters

There were two other types of measurements whose spatial scales were more comparable with those of the satellite images: doppler acoustic log velocities and surface drifter tracks. Comparisons with these measurements confirmed that the satellite images contained information about the surface velocity field.

The doppler log is an acoustic device which measures velocity shear from depths of about 30 m to 100 m. Michael Kosro was responsible for collecting these measurements and for producing maps of near-surface currents. The doppler log was operated from the R/V Wecoma during both hydrographic surveys. Figures 6.2 and 6.3 show velocity vectors at about 30 m below the surface along with the satellite image which corresponded most closely in time. The satellite data were

recorded in about five minutes while the doppler velocities were recorded over several days so times scales are not precisely matched. The X on the velocity vector marks the location of the measurement and the tail of the vector. In Figure 6.3 both the satellite image and the doppler velocities show evidence of two eddies of about 30 km diameter. The eddy north of Pt. Arena is cyclonic and cold; the eddy south of it is anti-cyclonic and warm. The maximum velocities shown are about 50 cm s^{-1} .

Both the doppler-log velocities and the satellite images were obtained by remote sensing techniques which are relatively new to oceanographic experiments. These measurements are complementary in understanding the spatial structures in currents: the satellite images established that the current reversals measured by the doppler log were eddies; the doppler log established that the SST structures that appear to roll up have the corresponding velocity structures. The satellite images define the spatial and temporal extent of the velocity structures and the doppler log assigns numbers to the spatial patterns seen by the satellite.

Surface drifters tracked by Russ Davis showed similarly good correspondence with the satellite data (Davis, 1983). The drifters were designed to respond only to the shallowest currents and were not drogued. Several series of drifters were released during each of the hydrographic surveys and were tracked by aircraft. Although released within a small area, the drifters followed widely-varying trajectories. Figure 6.5 shows the tracks of a set of drifters released during the second hydrographic survey along with a satellite image. The triangle

marks the position at which the drifter was deployed on day 185 (4 July 1981). The drifters were tracked until sometime on day 189 (8 July). The satellite image is from day 188 so that it corresponds with the middle part of the tracks. The drifters were sighted intermittently; their known locations at intervals of about six hours are shown here connected by straight lines. Some of the drifters deployed northwest of Pt. Arena were entrained by the large (40 km diameter) cold eddy shown in the satellite image. This eddy could be followed from its apparent origin south of Cape Mendocino about ten days earlier to its absorption into the cold plume near Pt. Reyes about a week later. Its approximate southward drift was 10 cm s^{-1} . The drifters which moved south went offshore just north of Pt. Reyes, where the cold plume of water extends out from the coast about 250 km.

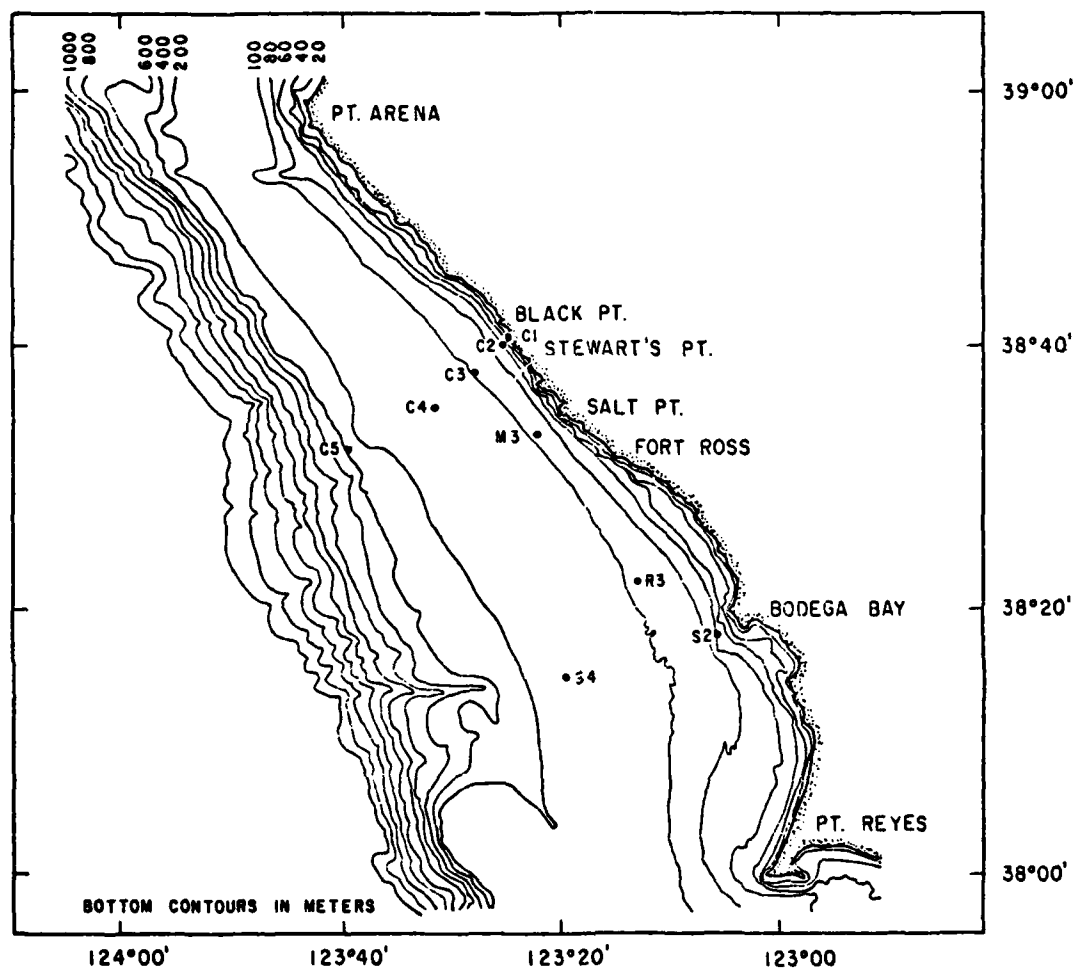


FIG. 6.1 CODE-1 MOORING LOCATIONS

Sites C1, C3, C5, M3 and R3 had current meters densely spaced in the vertical. Winds were recorded at sites C3, C5, R3 and S4. Thermistors used in the comparisons in Chapter 4 were located at C5, R3 and S4.

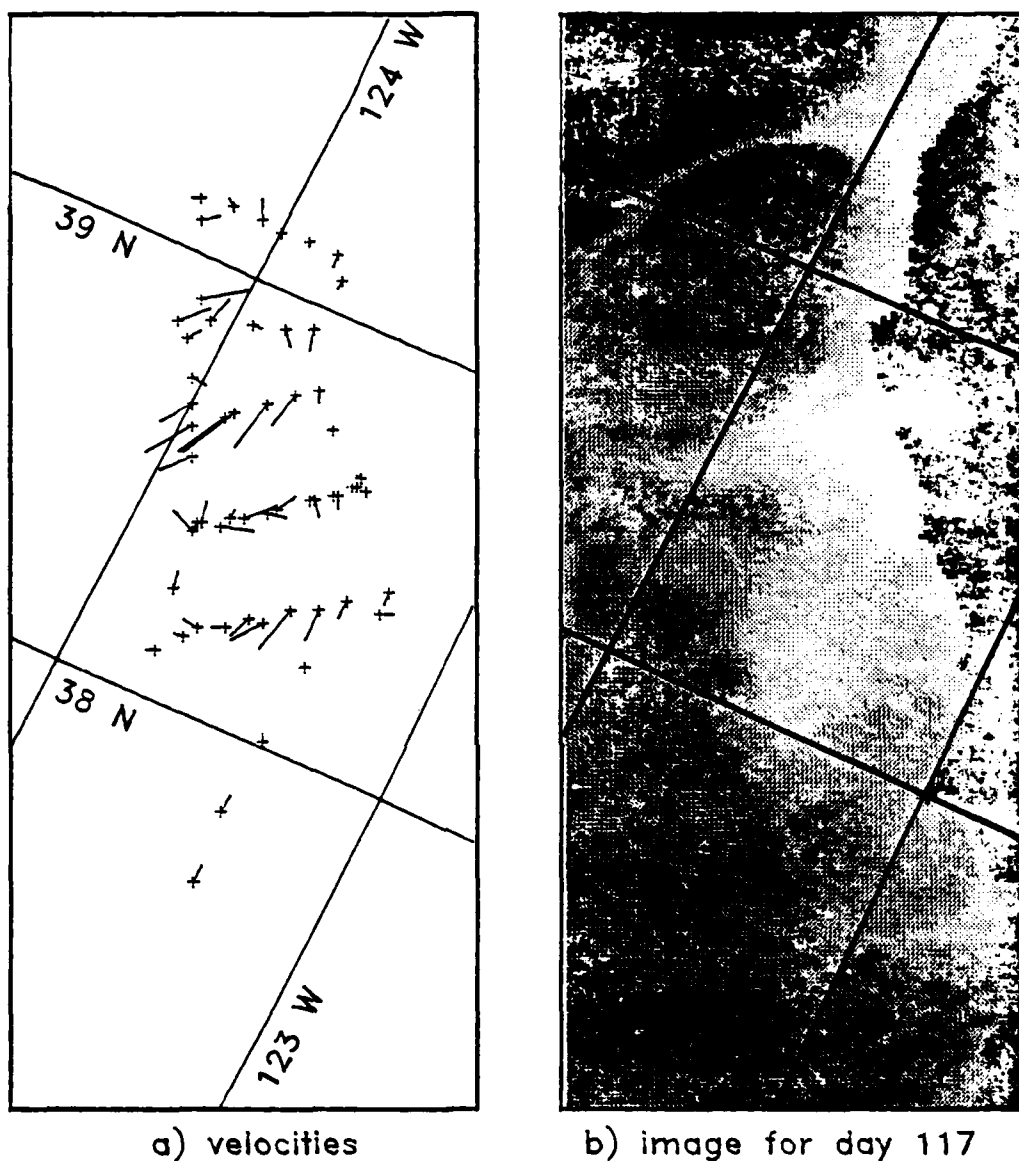


FIG. 6.2 DOPPLER VELOCITIES AND SATELLITE IMAGE

Comparison of a) doppler acoustic log velocities computed by J. M. Kosro from measurements on days 116-118 with b) satellite image for the same area on day 117. The cross marks the tail of the velocity vector and the location of the measurement. The points in the coastline at the right are Pt. Arena and Pt. Reyes. Note the relatively large offshore velocities corresponding to the cold plume southwest of Pt. Arena.

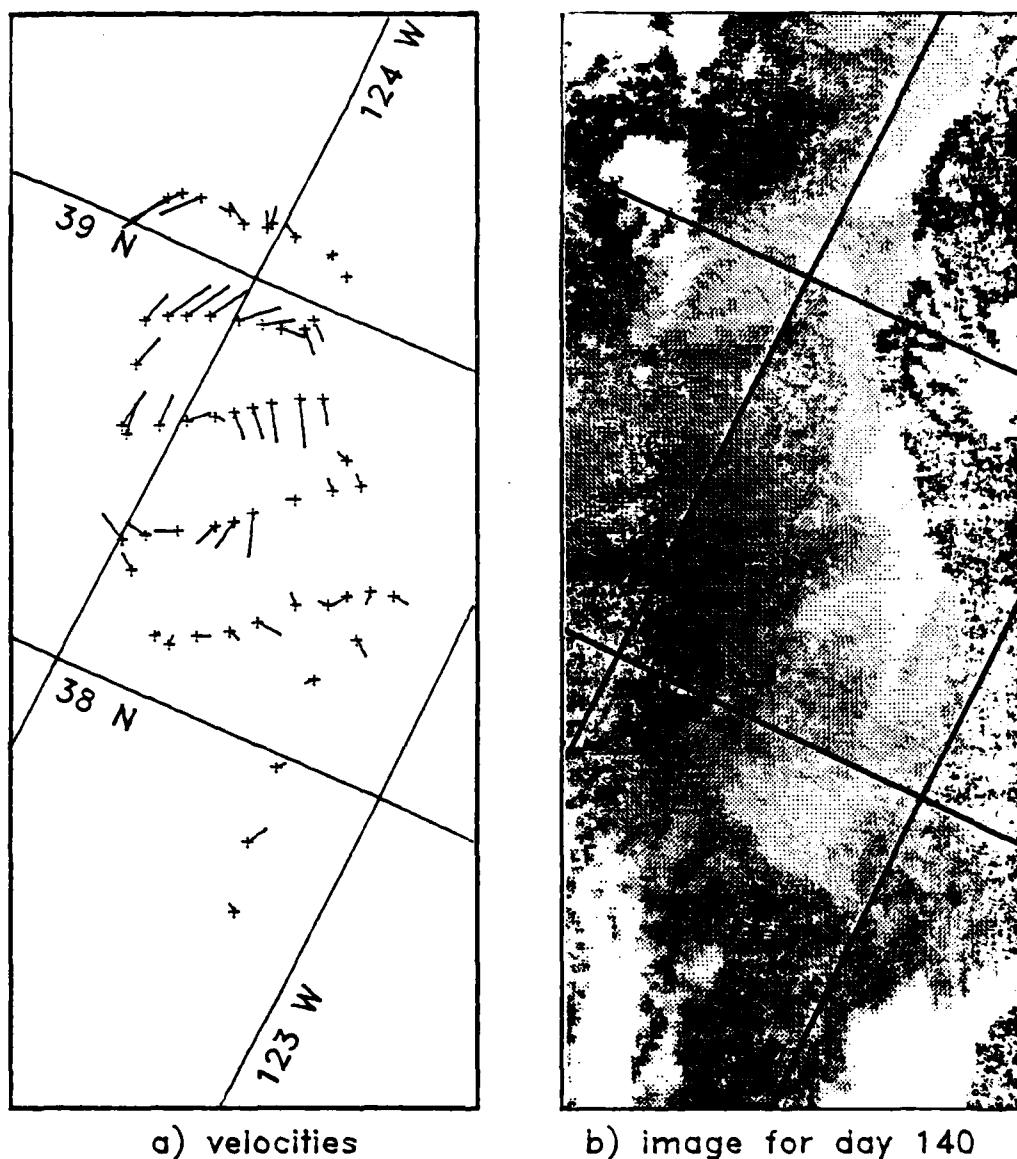


FIG. 6.3 DOPPLER VELOCITIES AND SATELLITE IMAGE

Comparison of a) doppler velocities from Kosro for days 141-143 with b) satellite image on day 140 for the same area. Note that the cyclonic eddy northwest of Pt. Arena evident in the velocities corresponds to a well-defined cold region which appears to have cyclonic rotation. A larger warm anti-cyclonic eddy southwest of Pt. Arena is paired with this cold eddy, but has a weaker temperature signature.

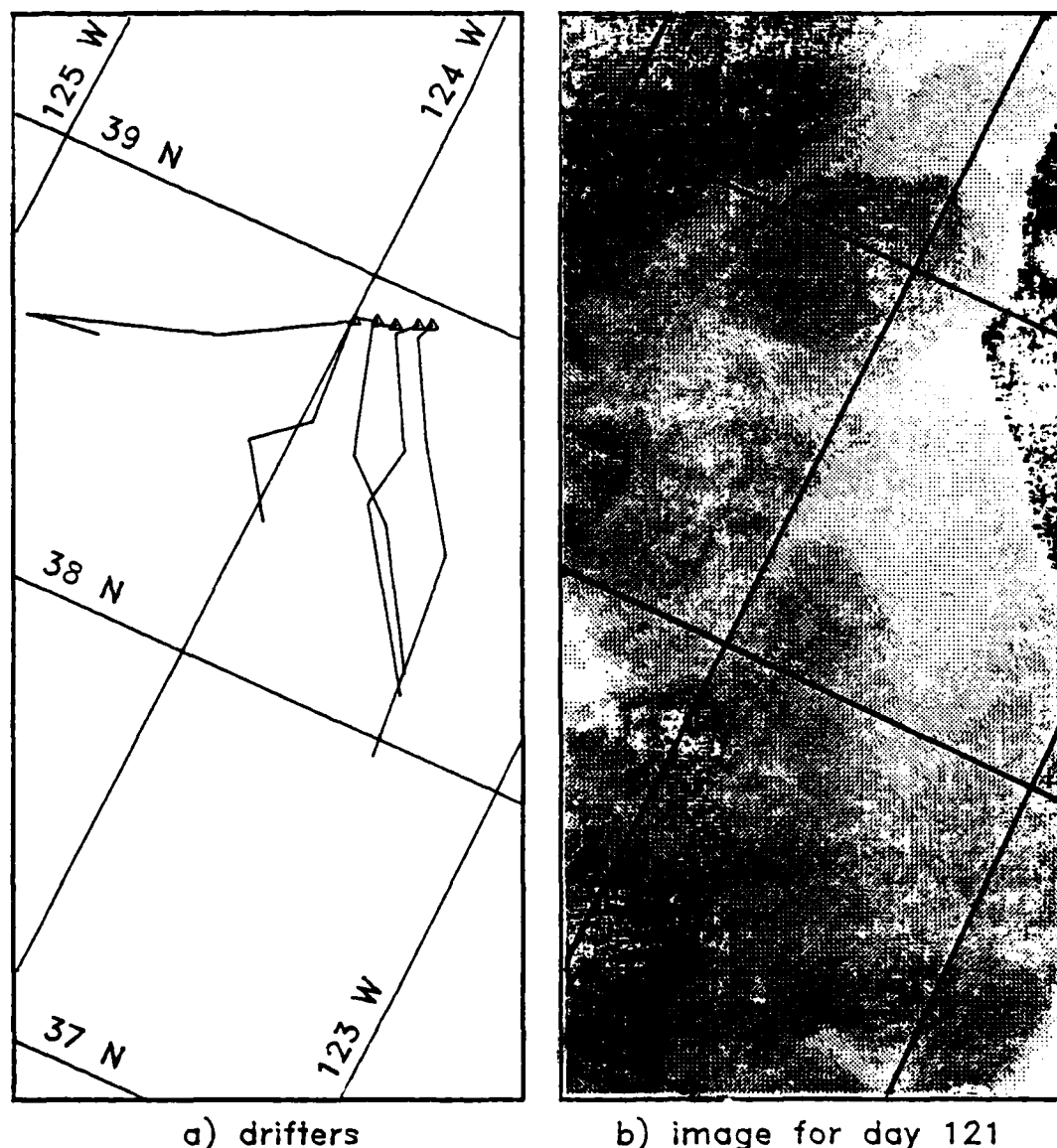


FIG. 6.4 DRIFTER TRACKS AND SATELLITE IMAGE

Comparison of a) the trajectories of surface drifters tracked by R. E. Davis from release on day 122 to day 126 with b) the satellite image for the same area on day 121. Release locations are denoted by triangles. Locations were recorded about every six hours and are connected by straight lines. In successive images the warm area northwest of Pt. Arena contracted to form a single cold plume at the point. The single drifter which moved rapidly offshore was caught in this plume.

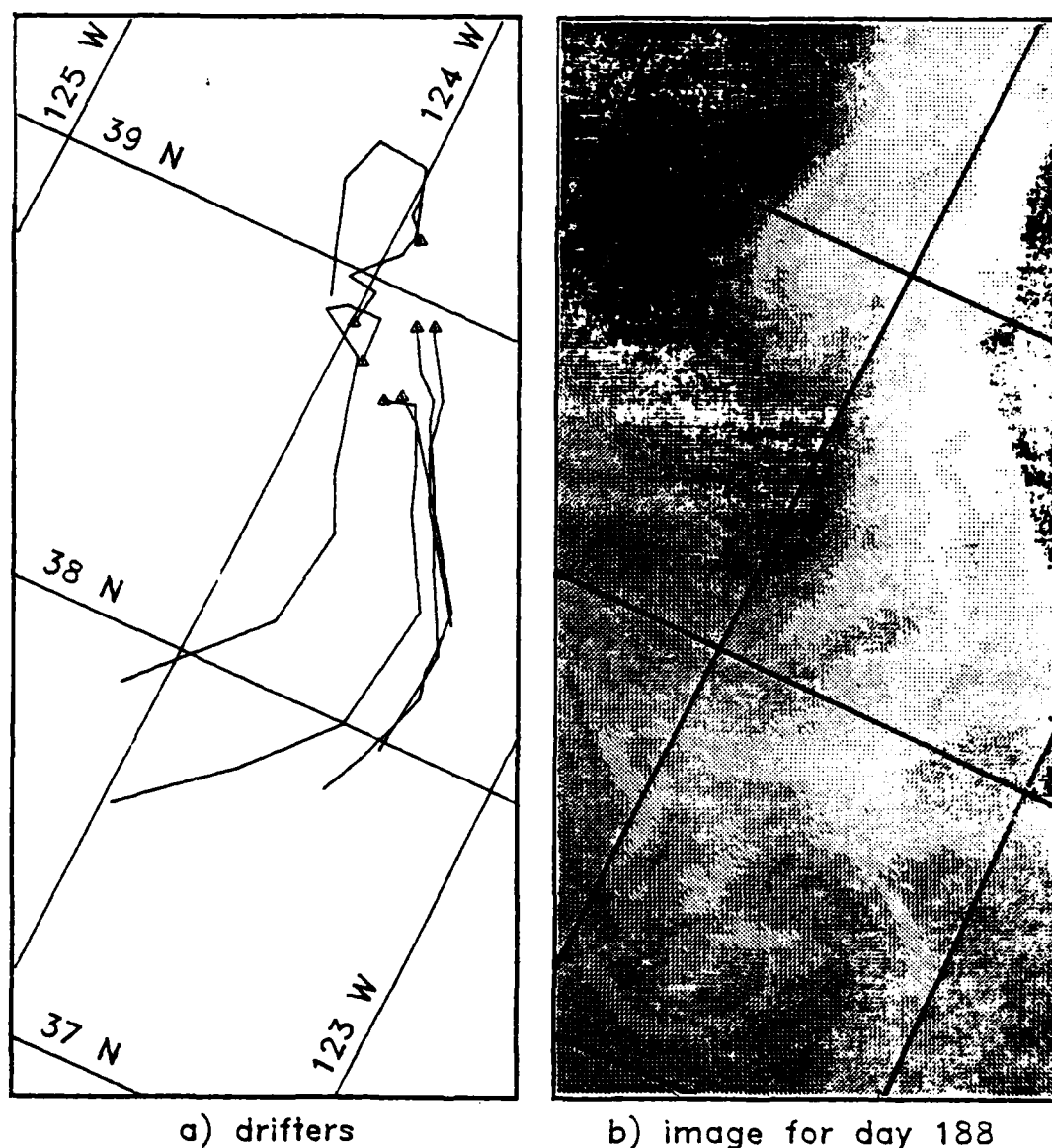


FIG. 6.5 DRIFTER TRACKS AND SATELLITE IMAGE

Comparison of a) surface drifter tracks from Davis for days 185-189 with b) satellite image for the same area. Release locations for the drifters are denoted by triangles. The cold eddy northwest of Pt. Arena had a southward drift speed of about 10 km/day, which places it at the circular drifter track on the release day (185). Note that all drifters south of Pt. Arena were swept offshore in the cold plume north of Pt. Reyes, which is just visible at the right edge of the image. This plume extended about 250 km offshore.

CHAPTER 7

WINDS, TOPOGRAPHY AND SST

An examination of numerous satellite images revealed apparent patterns in what seemed to be a chaotic SST field. The large cold plumes which extended some hundreds of kilometers offshore, particularly in the summer and fall, recurred in about the same place from year to year (cf: Kelly, 1982 and Breaker, 1981). Within a given year features formed and reformed in about the same location. A large (about 40-km diameter) cold, cyclonic eddy appeared offshore of Pt. Arena in both CODE-1 and CODE-2, at times moving slowly (10 cm s^{-1}) down the coast. There appear to be special places along the coast which trap or generate temperature features. These special places are usually associated with capes or points, of which there are several in this region as well as the San Francisco Bay: Cape Mendocino with very rough bottom topography, Pt. Arena, an uncomplicated bump in the coastline and Pt. Reyes with a wide shelf which extends down to San Francisco Bay (see Figure 7.1). The purpose of this chapter is to quantify the extent of this coastal trapping and to determine the relationship between the SST patterns and the wind. The comparisons between SST and near-surface velocities shown in Chapter 6 indicate that the SST patterns closely resembled those of the velocity field so that this is also an analysis of the relationship of meanders in the California Current to topography and winds. Sea-level height was also examined, not as an independent variable, but as an additional description of the wind response. Chelton (1980) showed that SLH was well-correlated with geostrophic winds but he could not resolve the coastal upwelling response with his data.

Variable topography could generate SST features by flow separation. The large cold eddy shown in Figure 6.5 appeared to be shed from Cape Mendocino about ten days before the image was recorded. In flow visualization experiments Head (1982) showed that a pressure gradient that opposed the flow caused a turbulent boundary layer to widen and separate; such a pressure gradient could arise from the variable topography.

The large, energetic features typically occur in the summer and fall when southward winds are strong and are identifiable by large temperature anomalies; therefore, they are presumably associated with coastal upwelling. Arthur (1965) suggested that the intense upwelling observed on the leeward side of capes was due to an increase in vorticity from the deformation of streamlines around the cape. Hua (1981) simulated the upwelling patterns off the coast of southern France using only the coast shape in a numerical model. Peffley and O'Brien (1976) compared the effect of coast shape and topography on upwelling coastal circulation off Oregon using numerical simulation. They concluded that bottom topography was more important than coast shape in determining the velocity field; however, their published model results showed that the near-surface currents followed the coast shape.

In addition to the direct effect of irregular topography on coastal circulation, the topography may also make the wind field irregular, in turn causing the patterns in SST. Capes usually have an expression above sea level as well as below. Variability in the wind field of a factor of two on scales of 20 km were found during an overflight by Friehe during CODE-1 (Friehe and Winant, 1982). Maps of the winds

measured during the first hydrographic survey showed a positive curl in the wind field south of Pt. Arena where the nearshore winds followed the bend in the coastline (Fleischbein, et al., 1983).

In the measurements it is difficult to separate these parameters, especially because the SST's, the winds and the topography are complicated. To simplify the comparisons the SST maps and the wind and SLH records were decomposed into their dominant modes, using empirical orthogonal functions. The wind and SLH records used were those obtained at coastal stations from Crescent City to Point Conception by Allen and Halliwell (1983) as shown in Figure 7.1, as well as the winds collected at the CODE site (Mills and Beardsley, 1983).

7.1 Empirical Orthogonal Functions

To obtain a more concise description of the variables to be used for comparisons, SST, winds and SLH were decomposed into empirical orthogonal functions (EOF's). These functions do not necessarily have dynamical significance; they are useful when one does not know a priori what the signal should look like. By using those few functions which describe most of the variance in the data, one can distinguish the dominant recurring patterns from the remaining variability, which may be treated as noise for most analyses.

The EOF decomposition of the data is a linear combination of functions of space, $f_j(x_i)$,

$$D(x, t) = F(x) A(t) \quad (7.1)$$

where D is the $N \times T$ matrix of data, with T columns of measurements at each of N locations, F is a $N \times N$ matrix which contains each function, in a column and A is an $N \times T$ matrix of coefficients. The functions are spatial patterns and the coefficients are amplitudes which are functions only of time. The functions are orthogonal in the usual sense of vectors and are normalized so that

$$F^T F = I \quad (7.2)$$

Davis (1976) discusses EOF's using summation notation; Appendix E contains a similar discussion in vector notation.

7.2 Computing EOF's Using Singular Value Decomposition

The large number of SST data made the usual method of computing EOF's impractical, so an alternative method was used. The usual method requires computing a covariance matrix and solving for its eigenvalues and eigenvectors. If D is the data matrix, with each of the T images in a column, then the mean product matrix, C , is given by

$$C = \frac{1}{T} D D^T \quad (7.3)$$

where D^T is the transpose of D . If all the images are independent samples of the variable then this mean product matrix is the covariance matrix and the EOF's are found by solving the eigenvalue problem

$$C F = F L \quad (7.4)$$

where F is the square matrix whose columns are eigenvectors and L is the diagonal matrix of eigenvalues. There were approximately 5000 spatial points sampled at 50 times, so the covariance matrix would be 5000×5000 . Computing F takes $O(N^3)$ operations, where $N = 5000$. The storage requirement for the matrix (100 megabytes) and the computer time required to solve this system make this problem impossible on a typical scientific computer. One alternative is to compute a few of the eigenvectors corresponding to the largest eigenvalues using a power method (Parlett, 1980); however, it is still necessary to compute and store the large matrix. Another alternative, which takes advantage of the large ratio of spatial points to temporal points and which was used for the SST data, is singular value decomposition (SVD) (Lawson and Hanson, 1974).

Instead of solving for the eigenvectors of the covariance matrix, one can factor the data matrix to obtain its singular values and singular vectors. The data matrix, D , is factored into

$$D = F S H^T \quad (7.5)$$

where F is the same matrix of orthogonal functions as in Equation 7.4 and H is the matrix of functions corresponding to $D^T D$ instead of DD^T . The matrix, S , has the form

$$S = \begin{bmatrix} S' \\ 0 \end{bmatrix}$$

where S' is diagonal. The relationship between the singular values, s_i ,

on the diagonal of S' and the eigenvalues of L , l_i , is

$$s_i^2 = l_i \quad (7.6)$$

The operation count for computing the SVD is $O(NT^2)$. Using the values above for N and T the SVD method is 10^4 times faster than the covariance method: this difference makes the computation of the EOF's feasible. Appendix E contains a more detailed description of EOF's and the SVD method for computing them.

7.3 Missing Data

A drawback of the SVD method is its inability to handle missing data. Using the covariance method one estimates the elements of the matrix C by simply averaging over the available data, e.g., averaging over $(T-4)$ pairs of data if 4 measurements are missing. No equivalent process can be defined for SVD; therefore, the missing elements of the data matrix D must be estimated. Having a large ratio of estimated elements to data will degrade the analysis so EOF's were computed only for those areas which had good coverage in time.

Missing data were estimated using a variation of objective mapping (Bretherton, Davis and Fandry, 1976). The method used on the images is described in some detail in Appendix D. A linear combination of data nearby in space and time were used to fill holes in images which were already nearly complete. Using the temporal correlation shown in Figure 5.2 data nearby in time were limited to other images within 12 or 24 hours of the original image. The spatial analysis shown in Figure 5.1

showed that the images used for the EOF's, which were obtained from the original data by averaging over 5×5 boxes, could be averaged again over 2×2 boxes without degrading the signal. Therefore, data nearby in space were defined as data within a 3×3 box surrounding the missing datum. Using the error estimate described in Appendix D, a missing datum was replaced by an estimated value only if the mean square error of the estimate was less than 30 % of the variance at that location. Thus only "small" holes were filled by interpolating spatially. Partial images separated by 12 hours (and occasionally by 24 hours) were composited; the objective mapping technique smoothed the edges where the second image was used to fill a large hole in the original. These composited and interpolated images were used to compute the EOF's; the original images were used to compute the time-varying amplitudes.

7.4 SST Bias for Certain Wind Conditions

A comparison of the available images as shown in Figure 2.2 and the wind records near the CODE site (Mills and Beardsley, 1983) reveals a tendency to have clouds obscuring the sea surface during periods of calm weather, and to have clear skies when winds were strong and steady. To quantify this bias I examined the wind records from two NDBO buoys (46014 and 46013). Using the rms average of the wind speeds for the two records, I computed the mean of the wind speed versus its variance over every two-day interval; a plot of these values is shown in Figure 7.2a. In Figure 7.2b are shown the wind mean and variance for the two days prior to each usable image, with a symbol indicating how many clear pixels the image contained. At low wind speeds many of the images had

fewer than 2000 pixels (out of a maximum of 8335 pixels). The clearest images generally coincided with higher wind speeds. The mean-variance plane was divided into four categories as shown on Figure 7.2a and in Table 7.1. The percentage of days of the wind record which fell in each category is shown in the table along with the percentage of images which fell in each category. Categories 1 and 3 were severely undersampled: category 1 images were mostly cloudy and there were few images in category 3. Periods of calm winds with low variability were generally cloudy; periods of high variability were adequately sampled by the images and periods of strong, steady winds predominated.

The representativeness of the empirical modes for various wind conditions was limited by the availability of images in categories 1 and 3. In computing the EOF's images from these categories were weighted to minimize this wind bias.

7.5 Computing SST EOF's by Separate Regions

Three non-overlapping spatial regions, with varying biases toward strong, steady winds, were defined for three separate empirical mode decompositions. Cloud coverage had a regular pattern: the edge of a cloud bank was usually parallel to the coast with its distance offshore varying with wind conditions. A region close to the coast was most often cloud-free; this region at times expanded to include half or more of the image. The shape of each region used in the modes was defined by the intersection of a group of images from categories 1 and 3. These images were combined with those images from wind categories 2 and 4 which were clear over the same area. An EOF decomposition was

done for each region; images from regions 1 and 3 were duplicated or triplicated to preserve the same ratio of the wind categories as in the whole record as shown in Table 7.1. Including the images multiple times is equivalent to weighting data in the covariance method for computing EOF's. The number of spatial points for each region and the number of actual images from each wind condition which were used in the EOF's are listed in Table 7.2.

EOF's for a larger region were computed as linear combinations of the EOF's from the smaller regions. A new EOF problem was defined in terms of the coefficients of the EOF's of the smaller regions; the procedure is presented here briefly. Define the matrix D' as the union of the data from the separate regions

$$D' = \sum_{i=1}^3 D_i \quad (7.7)$$

where each D_i covers the union of the three regions and has the value of the original data matrix in region i and is zero outside region i . For each region i the EOF decomposition was computed for the its data matrix

$$D_i = F_i A_i \quad (7.8)$$

where each matrix, F_i , of EOF's is defined analogously to D_i , i.e., it is zero outside of region i and takes the value of the functions inside region i . Because the EOF's were computed for non-overlapping regions, functions from region a , for example, are trivially orthogonal to the functions from regions b and c because they are each zero outside the

region on which they were computed. Then D' can be written as a linear combination of the F_i 's as

$$D' = FA \quad (7.9)$$

where the new matrix F is formed by joining the F_1 , F_2 , and F_3

$$F = [F_1 \mid F_2 \mid F_3]$$

and A is formed by joining the matrices of coefficients

$$A = \begin{bmatrix} A_1 \\ A_2 \\ A_3 \end{bmatrix}$$

The EOF's of D' are defined by the relationship

$$D'D'^T F' = F'L' \quad (7.10)$$

which is the same as equation 7.4. Defining the larger region EOF's as linear combinations of those from the smaller regions

$$F' = FG \quad (7.11)$$

where G is a new matrix of coefficients to be determined, and substituting 7.9 and 7.11 into 7.10 gives

$$FAA^T F^T FG = FGL' \quad (7.12)$$

which can be simplified by recalling that

$$F^T F = I \quad (7.13)$$

and by multiplying 7.12 on the left by F^T to obtain

$$AA^T G = GL' \quad (7.14)$$

This equation is analogous to 7.4 where the covariance matrix of the data, C , has been replaced by the covariance matrix of the coefficients, AA^T , for the small region EOF's. The functions, F , have been replaced by the matrix, G , which determines the linear combinations of the functions in F needed to produce the functions in F' . Equation 7.14 can be solved to find G (using the usual eigenvector decomposition because now A is not large) and F' can be computed using equation 7.11.

Composite modes were computed for region a together with region b and for all three regions together. The separate modes as well as the composite modes are described in section 7.9.

7.6 Amplitudes for Partial Images

For each region for which F was computed using composited images, the amplitudes were computed using the original images. When no data are missing from any spatial point the amplitudes, A , in equation 7.1 are simply the projection of the data at time t_j onto the functions

$$A(t_j) = F^T D(t_j) \quad (7.15)$$

which is a dot product of the j th column of D (a single image) with each column of F (an EOF). Because the functions are orthogonal there is a unique representation of the data in terms of the functions so A is uniquely determined.

When some of the data are missing the dot product of the data with each function can still be defined for the available data. However, there is no unique decomposition because the pieces of the functions which correspond to the available data are no longer necessarily orthogonal. Therefore, A must be estimated. A method which produces an unbiased estimate for A is a least-squares fit to the partial functions, i.e., solving the overdetermined system

$$D(t_j) = F A(t_j), \quad (7.16)$$

a set of N' equations in M unknowns, where N' is the number of available data and M is the number of functions. This system was solved using a matrix factorization algorithm, QR (Lawson and Hanson, 1974). The coefficients, $A(t)$, were only computed for those images for which at least 50 % of the data were available. Only these coefficients were used for the modes for the larger regions.

7.7 Misfit

Because there were not many images and not all of them were used in each computation, the functions may be biased toward the images used in the computation. To determine the bias of the EOF's, the rms misfit of each image to the first four modes was computed as

$$(\text{misfit})^2 = \frac{1}{N'} (D(t_j) - FA(t_j))^T (D(t_j) - FA(t_j)) \quad (7.17)$$

where N' is the number of clear pixels in the image and the amplitudes were those computed by a least-squares fit. For each region the misfit was plotted against the percentage of data in the image as shown in Figure 7.3. Each image is designated by a symbol which indicates whether it was a base image for the interpolation procedure, an image used to supplement the base image in a composite, or was not used to compute the EOF's for the given region. If the EOF's were heavily biased toward the particular images that were used in the calculation, one would expect the misfit to be significantly smaller for these images. The misfit was only slightly larger for those images which were not used in the EOF computation, regardless of the amount of data which were cloud-free. The EOF analysis, like any statistic, works best when the number of measurements over which one averages is large; however, the plots in Figure 7.3 show that the EOF's described the data used to compute them only slightly better than the other data. In other words, with a few exceptions, the EOF's can be treated as representative of the entire data set.

In regions a and b there were a few images whose misfit was noticeably larger. For region a those days were 133, 175 and 180 and for region b they were 178, 179 and 180. The days not well-described by the region b modes was an interesting period in which the wind started and stopped several times over a period of a few days. For this event the ocean near Pt. Reyes was always under clouds.

7.8 EOF's for Wind and Sea-Level Height

The winds and sea-level height records were filtered before the EOF's were computed. Both the wind vectors and SLH were sampled much more frequently than the 12-hour sampling interval of the infrared images. Averaging and interpolating the SST data, as described in section 7.3, further reduced the SST resolution to about 24 hours. In addition to the sampling rate problem, one might expect that SST is related to the geostrophic adjustment of density surfaces and thus has an inherently longer time scale than the wind. For all these reasons the wind and SLH records were filtered using a gaussian Fourier filter with a half-power period of four days.

Wind vectors were first converted to wind stress because the forcing parameter is a non-linear function of the measured winds; the relationship between wind stress and the wind vectors is

$$\tau = \rho_a C_d |\mathbf{y}| \mathbf{y} \quad (7.18)$$

where ρ_a is the density of air, C_d is an empirical drag coefficient and \mathbf{y} is the wind vector measured at 10 m above the sea surface (see, for

example, Bakun, 1975). The value used for C_d was that determined by Large and Pond (1981)

$$10^3 C_d = \begin{cases} 1.2, & U_{10} \leq 11 \text{ ms}^{-1} \\ 0.49 + 0.065 U_{10}, & U_{10} > 11 \text{ ms}^{-1} \end{cases}$$

After conversion to wind stress and after low-pass filtering the mean wind stress at each location was computed and subtracted before the EOF's were computed. The mean winds were southward, or upwelling-favorable, from Crescent City to Point Conception and were apparently strongest from Pt. Arena to the CODE array, although winds measured at the coast were probably weaker due to the sheltering effects of land. The EOF decomposition of the coastal wind field was computed by including both the u and v components in a single covariance matrix.

7.2 The Empirical Modes for Winds, SST and SLH

Each of the variables was well described by a few modes. The amount of variance which each mode described is shown in Table 7.3. The total variance for each variable is given by the sum of the squares of all the data, after the mean has been removed,

$$\sum_{j=1}^T D(t_j)^T D(t_j)$$

which can be rewritten using equations 7.2 and 7.16 as

$$\text{total variance} = \sum_{j=1}^T (FA(t_j))^T FA(t_j) \quad (7.19)$$

$$= \sum_{j=1}^T A(t_j)^T A(t_j)$$

which is simply the sum of the squares of all the elements in A and is shown in Appendix E to be the sum of the eigenvalues, f_i . The percent of variance for each mode is the ratio of its eigenvalue to the sum of all the eigenvalues. For comparison the cumulative percentage of variance described by the modes for each variable is shown in Figure 7.5. The more complex a variable is, the more modes are required to describe a given amount of variance. The wind field was the most complicated, requiring four modes to describe about 90 % of the variance as compared with, for example, two modes for region c, and two modes of SLH which described more than 95 % of the variance. Region a was nearly as complex as the wind, requiring four modes to describe 90 % of the variance.

Selected SST modes are shown in gray tones in Figures 7.6a through g. Light shades correspond to negative values and dark tones to positive values; for reference, the region over which the modes is zero is a medium gray. The first mode for each region is virtually a constant and is only shown here for the combination of regions a, b and c. Figure 7.6a shows mode two for region a, which is an area adjoining the coast north of Pt. Reyes from 50 to 100 km wide. The mode has a north/south structure, changing sign just north of Pt. Arena and in the small region offshore. Mode three, shown in Figure 7.6b, has several sign changes with positive values between the capes and negative values extending offshore from the capes. This mode describes the trapping of SST features by coastal topography. Modes two and three for region b are shown in Figures 7.6c and d. Mode two has a north/south structure

similar to that of Figure 7.6a with an offshore sign change. The darkest area (most positive) is just outside San Francisco Bay and south of Pt. Reyes. Mode three is also positive near San Francisco Bay, but changes sign somewhat closer to shore at about 50 km from the coast. The modes for region c describes only a few events due to persistent cloud cover. The second mode for region c, shown in Figure 7.6e, reaches its largest amplitudes halfway down the image where the cold plumes extend offshore from Pt. Arena. This mode simply describes a north/south shift in the location of the plume. The first two modes for the combined regions a, b and c are shown in Figures 7.6f and g. The first mode is nearly a constant throughout the entire region; the dark areas mask the isolated spots for which there were insufficient data to compute EOF's, the quasi-permanent cloud bank (upper left corner) and the land (right edge). Mode two has a distinctly north/south structure near the coast and is essentially the union of the second modes from the separate regions. For this mode the entire region north of Pt. Arena is in phase, while the region south of Pt. Arena is much more complicated, although generally of the opposite sign. The region near the CODE array has a near-zero amplitude (the background gray is zero, for reference) indicating that it was not as affected by this mode as the areas to its north and south.

The first four empirical modes for the wind stress are shown in Figure 7.7. The plots have been stretched horizontally so that the wind vectors are more clearly visible; the X's mark the tail of the vectors and the location of the measurement. The locations can be identified by referring to Figures 7.1 and 7.4. The first mode shows an

intensification of winds in the CODE region with all wind vectors in essentially the same direction. The second wind mode shows a north/south structure with the node in the Central Line of the CODE array (see Figure 6.1). The farthest offshore wind vector was part of the northern regime while the most landward vector was part of the southern regime. A strong positive amplitude for this mode would create downwelling north of the CODE array, upwelling to the south, and a negative wind stress curl in the CODE array which would enhance downwelling by Ekman suction. This is the structure which can be seen in mode two of the SST for the combined regions shown in Figure 7.6g. The cold and warm water masses split at Pt. Arena and the CODE region is warm at its offshore extreme. The third mode also changes sign in the CODE array with the inshore vectors having the same sign as the region south of San Francisco; this mode gives a wind stress curl within the CODE array. For all modes shown, with the exception of one vector in in mode three, all stations south of San Francisco are in phase, suggesting that any wind measurement between Pt. Conception and San Francisco would be a good predictor of winds south of Pt. Reyes and, usually, also for the CODE region.

The SLH modes all change abruptly at about 38 N, i.e., between the north and south sides of Pt. Reyes, an indication that local topography has an important effect on this parameter. The SLH mean and the first three SLH modes are shown in Figure 7.8, plotted as a function of latitude; the location of the stations is shown in Figure 7.1. The second mode has a north/south structure with a sea-level maximum at Crescent City and a minimum at Pt. Conception. In the third mode the

sea level is higher for all stations south of Pt. Reyes than those north of Pt. Reyes, with a gradual recovery in height by Crescent City.

All three variables have a north/south structure in their second mode with a node whose location varies between Pt. Arena and Pt. Reyes. The SLH node is undoubtedly that which Chelton (1980) could locate only as somewhere between San Francisco and Crescent City; the occurrence of the node in the other variables suggests that the node is associated with the coastal upwelling which also could not be resolved by Chelton. The slight difference in the location of the nodes is consistent with the topographic features of most importance to each variable. For SLH the most important topography would be that of the shelf, which has its strongest anomaly at Pt. Reyes. For the wind the topography above sea level is most important, a combination of the large headlands at Pt. Arena and the valley north of Pt. Reyes which caused the inland turning of the coastal winds shown in mode two. The winds measured on land showed a node at Pt. Arena; offshore measurements indicated the nodal line tilts to the south farther offshore. Sea-surface temperature would be affected both by the shelf topography and by the wind structure. Mode two for the combined regions had a complicated structure with the strongest boundary at Pt. Reyes, a nearshore node at Pt. Arena and an offshore sign change that made the offshore edge of the CODE array in phase with the region north of Pt. Arena. From the structure of the second SST mode one expects the winds 50 km offshore of Pt. Reyes to be in phase with Pt. Arena winds rather than with Pt. Reyes winds, i.e., northward relative to winds at Pt. Reyes for a positive wind mode amplitude. Because the mean wind everywhere was strongly southward this

would actually be a weakening of the winds offshore of Pt. Reyes.

7.10 The Time-Varying Amplitudes

For each variable time-varying amplitudes were computed to determine the relationship between the variables. The low sampling rate for SST and the patchy coverage made the computation of significant correlations impossible, so the amplitudes presented in Figures 7.9 through 7.11 are compared qualitatively.

The SST amplitudes for the first few modes are shown in Figures 7.9a, b and c. The amplitudes for each mode for all the regions are shown on a single figure because the modes for the separate regions appear to describe the same phenomena. The computed amplitudes are shown as triangles connected by straight lines in the figures. The first mode shows a mean temperature change in each region; a positive amplitude corresponds to colder temperatures. The functions were normalized to unity over the area covered, which was three times as large for the combined region as for region a; thus, an amplitude from the combined region which is three times as large as that for region a results in the same temperature anomaly.

The mode one amplitudes show a cooling of about 2.5 C. in each of the regions which took place between days 140 and 160 (about 20 May to 10 June). This compared favorably with the near-surface temperature change recorded in C5 of the CODE array of about 2 C. and with the hydrographic data, which showed a change of about 2 C. in the CODE array between day 125 and day 190. Between day 160 and day 190 the satellite

data show an increase of about 0.5 C. so that the agreement between the satellite data and the hydrographic data is excellent. Errors due to viewing angle, satellite calibration or atmospheric effects would show up in this mode so that some of the smaller fluctuations in the mode one amplitude do not reflect actual SST changes. As shown in Chapter 4 these errors had magnitudes of about 0.4 C. after an empirical viewing-angle correction was applied; however, these errors are random so that trends in the amplitudes are believable. The rapid warming coincided with a period of unsteady winds, as shown in Figure 7.10, which followed a period of intense southward (upwelling-favorable) winds. The nearly twenty days of intense southward winds following this warming trend, which produced a drop in temperature of only about 0.5 C., indicates that the wind response of SST is too small to account for this warming trend. Thus, the warming was probably due to seasonal heating or advection.

The second mode for both region a and the combination of regions a, b and c appeared to be anti-correlated with the amplitude of the second wind stress mode shown in Figure 7.11, with the wind leading SST by a few days. The dominant SST peak at about day 130 and the dominant trough at day 165, followed by another peak at day 180, correspond well with the dominant signals in the wind amplitude, with the appropriate sense for local coastal upwelling. A trough in the second wind mode corresponds to winds favorable for upwelling in the north and downwelling-favorable winds in the south, while a peak in the SST mode corresponds to cold water in the north and warm water in the south which is just what is predicted by the simplest coastal upwelling model. The

combination of the analogous structure in the second modes, the correspondence in the peak amplitudes and the agreement in sense with a simple upwelling model suggests that the primary synoptic-scale SST pattern was due to local variability in the wind. The second SLH mode, which has the same north/south structure as the other variables, is clearly correlated with the second wind mode at about a two-day lag; it is also clearly anti-correlated with the second SST mode. This completes the description of local upwelling because a trough in SLH mode two corresponds to anomalously high sea level in the south (characteristic of downwelling) and low sea level in the north (upwelling).

The third SST mode for either region a or region b appeared to be correlated with the first wind mode at a lag of about three days, which suggests that the plumes at the capes were generated by the variable topography rather than by a complex wind field. If a complicated wind structure were causing the plumes the third SST mode would be correlated with higher wind modes, rather than the simple first mode. The sense for the correlation is logical: when the winds were uniformly southward cold plumes appeared at each of the three large capes with warmer regions in between. The days with the largest mode three amplitudes were days 131, 169 and 175; these days were preceded by continuous southward wind events from days 120 to 134 and from 162 to 176. Sea-level height was anti-correlated with the mode one amplitudes in the expected sense for upwelling: southward (northward) winds produced low (high) sea level. The SLH lagged the wind by about five days. This suggests the SLH should be correlated with the third SST mode at nearly zero lag and this appears to be true.

An even more difficult comparison with these sparse SST amplitudes was that between different SST modes at various time lags. The amplitudes from different modes are, by definition of the EOF's, uncorrelated at zero lag. The only obvious relationship between the modes that I found was between the second and third SST mode from region b. Mode two appeared to lead mode three by five to ten days, with the amplitudes anti-correlated. Qualitatively, for the region south of Pt. Reyes, a positive mode two event followed by a negative mode three event would be anomalously warm water being pushed offshore by cold coastal water, or the beginning of an upwelling event. The reverse case would be anomalously cold water replaced at the coast by warm water, which suggests a nearshore countercurrent. The latter type of event occurred between days 126 and 131. As with the cold plumes one would like to know whether this pattern derived from a similar pattern in the winds or did a relatively simple wind change have a complex response in the ocean, i.e., this countercurrent. Because SST modes two and three were correlated with winds modes two and one, respectively, I checked wind amplitudes for a correlation with each other at a lag of five to ten days. As predicted by the SST correlation wind mode two appeared to lead a negative mode one amplitude by about eight days. The wind event corresponding to the countercurrent was a strong southward wind at day 123 followed by a cessation of wind in the region south of Pt. Arena about day 128. A close examination of wind mode two shows an onshore/offshore structure in the CODE array. A negative amplitude for mode two gives calm conditions south of Pt. Reyes and along the coast in the CODE array, slightly offshore winds at Pt. Reyes and winds still strongly southward offshore at C5 and at Pt. Arena. This wind structure

could form a countercurrent along the coast from the south as warm water pushed back toward the coast in the absence of any wind forcing. It also seems like an appropriate mechanism for generating a cold plume at Pt. Arena: cold water continues to upwell north of Pt. Arena, while warm water moves onshore and northward south of Pt. Arena, creating a convergence of water at the point which forces the cold water farther offshore. The original images starting on day 130 show the cold region south of the large plume at Pt. Arena contracting toward the coast and the plume elongating. A plume is also forming at Pt. Reyes.

This sequence of events in early May suggests that the pattern of cessation of upwelling events may contribute to the formation of cold plumes. If the winds in the San Francisco Bay area stop before those at Pt. Arena, with onshore winds in the CODE region stopping before the offshore winds, the sea-surface tilt left from the upwelling regime forces warm water shoreward and the longshore pressure gradient which opposed the southward wind forces warm water northward. The water converges south of Pt. Reyes, due to the wide shelf and also converges south of Pt. Arena because the wind is still blowing there. In both cases the cold surface water is forced offshore in a plume or jet at the point. A more complicated event occurred from about day 175 to 185 (late June and early July). Neglecting an abrupt increase in southward wind on day 179, the cessation of upwelling was similar to that of the early May event: wind mode two became negative about day 178 and winds ceased everywhere by day 180. The images for days 178-180 showed a well-defined cold plume off Pt. Arena and off Pt. Reyes. The SST modes do not show a similar structure to that in early May; however, these

were the days which were not well-described by the SST modes as discussed in section 7.7.

7.11 Conclusions

The analysis of SST, wind stress and sea-level height using empirical orthogonal functions revealed an SST field which was dominated by local effects: the shapes of the SST mean and anomalies were determined by the coastal topography and spatial variations in the wind, and the intensity of the anomalies varied with wind strength. The close relationship between the near-surface velocities and the SST field shown in Chapter 6 indicates that the SST patterns are the same as those in the velocity field. Thus, the near-surface current field, like the SST field, is forced by local variations in the wind, with some trapping of features by coastal topography. The temporal resolution of the satellite data is insufficient to detect long, coastally-trapped waves, which would move rapidly through the region; however, this picture of locally-forced currents is inconsistent with the idea of energy propagating into the region from forcing elsewhere along the coast.

The dominant pattern of SST, wind stress and SLH was a north/south structure which was consistent with locally-generated coastal upwelling. The nodal point for the structure was north of Pt. Arena in SST, south of Pt. Arena in the wind and at Pt. Reyes in SLH. Despite sparse data for SST, the close correspondence between the amplitudes and modal shapes of the variables verified the simplest model of upwelling: southward local winds generate cold SST's within several days, along with anomalously low sea level. North of Pt. Arena the SST

signature of upwelling extended from the coast to about 80 km offshore, with the edge of the SST pattern following the bottom of the slope. South of Pt. Arena the pattern was more complicated, but the region of influence appeared to be even larger. This region is much larger than the shelf width at about 15 km; it encompasses the entire continental slope.

The SST variance was dominated by a mean temperature increase of about 2° C.; the temperature increase was the same as that observed in hydrographic data. This warming was probably due to seasonal heating or advection. This analysis showed that, despite residual systematic errors which make the mea SST signal noisy, the satellite images, appropriately averaged, can resolve absolute temperature changes.

The third SST mode was a series of warm and cold areas whose spacing was clearly determined by the coast shape. The correspondence between this mode and the first wind mode suggests that an irregular coastline generates cold plumes at capes when the wind is uniformly southward. There was no obvious correspondence between the shape of this mode and topography beyond the shelf, suggesting only the shallow topography, the coast and shelf shape, is responsible for the plumes. One event, however, suggested that a particular wind cycle may enhance the separation of the plumes from the coast. In early May a steady southward wind event ended by winds first dying down south of Pt. Reyes, followed by a cessation of winds everywhere a few days later. Warm water apparently moved onshore and northward near the coast while the wind near Pt. Arena was still southward, creating a convergence at Pt. Arena. A cold plume which had started to form at Pt. Arena became more

distinct and moved farther offshore. The importance of such a mechanism for plume formation cannot be determined conclusively without better spatial resolution of the winds and a longer record, such as that recorded by another satellite-mounted instrument, a scatterometer.

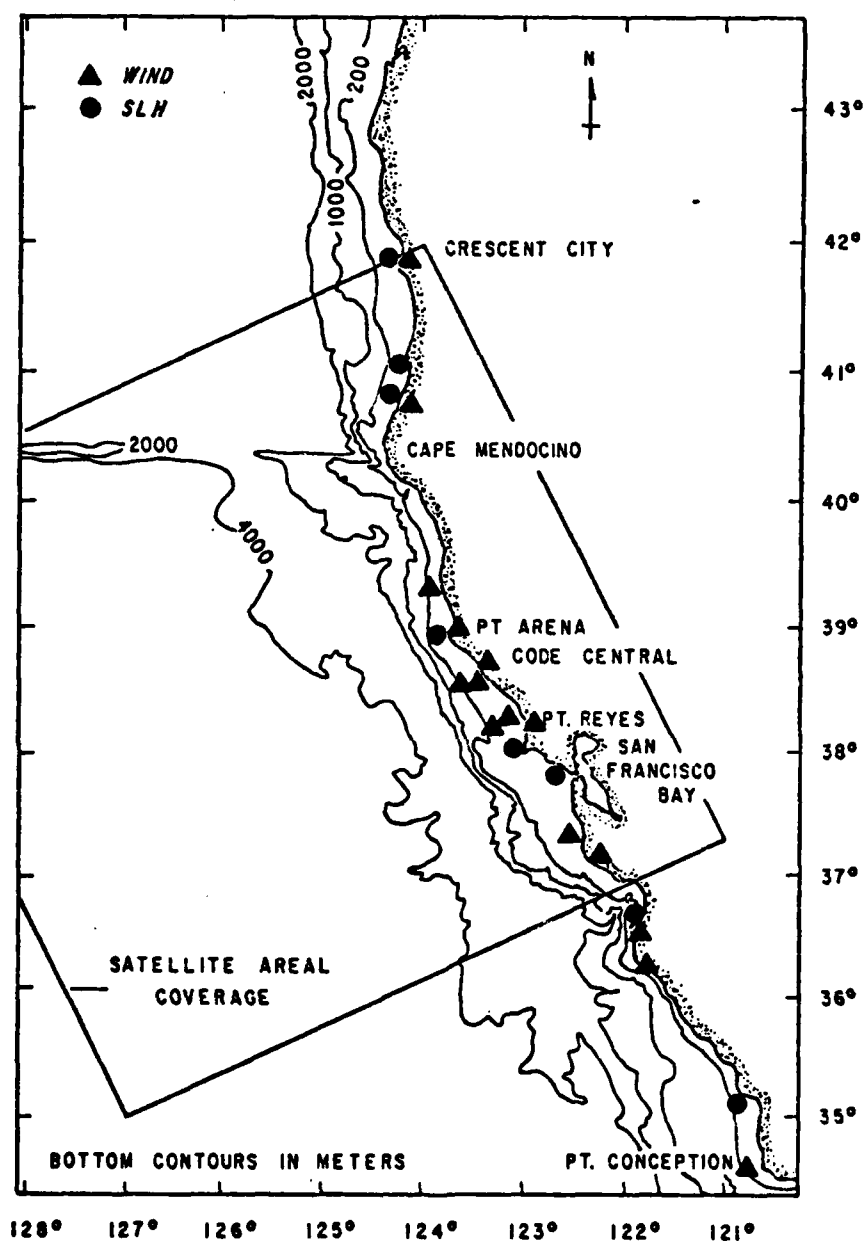
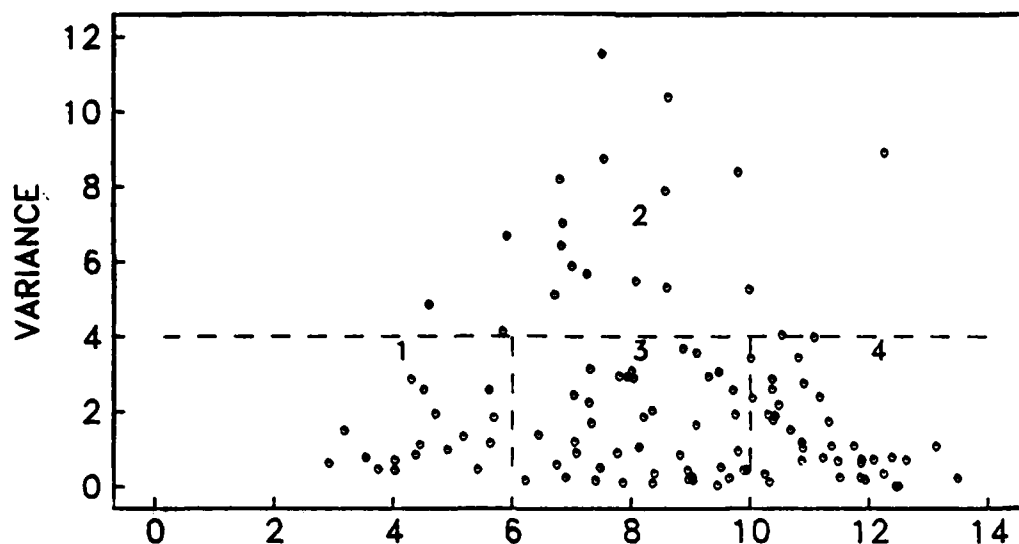
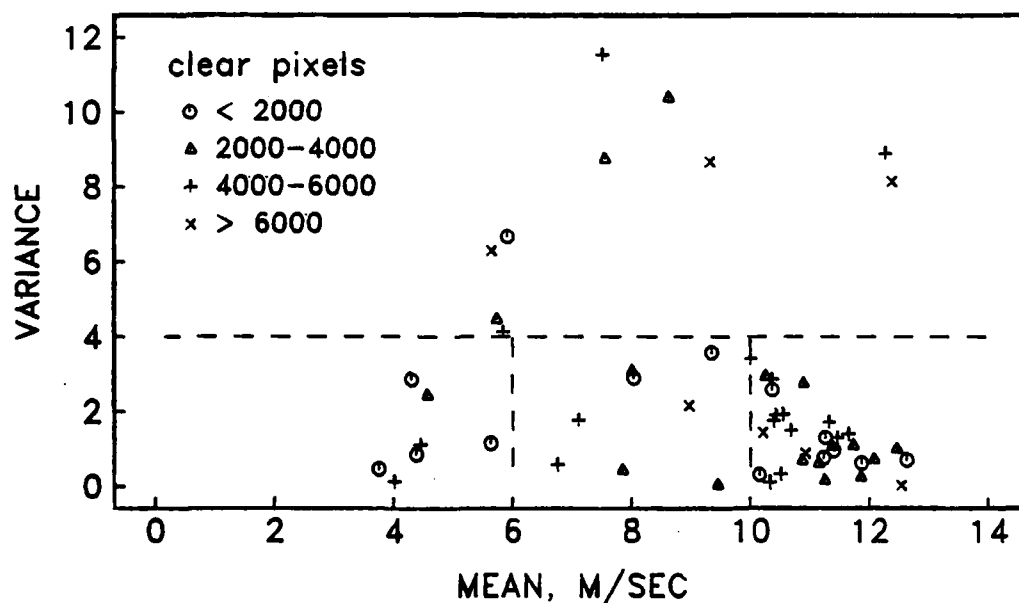


FIG. 7.1 LOCATIONS FOR WIND AND SLH MEASUREMENTS

In addition to wind measurements in the CODE array coastal winds and sea-level height measurements were collected at coastal stations from Crescent City to Point Conception.



a) entire wind record



b) images

FIG. 7.2 MEAN WIND SPEED VS. VARIANCE

Images were biased toward certain wind conditions. A scatter plot of the mean and variance for a two-day period is shown in a) for the entire wind record (100 days) and in b) for each image. The symbols show how many pixels, out of a maximum of 8335, were cloud-free. Categories 1 and 3 were undersampled.

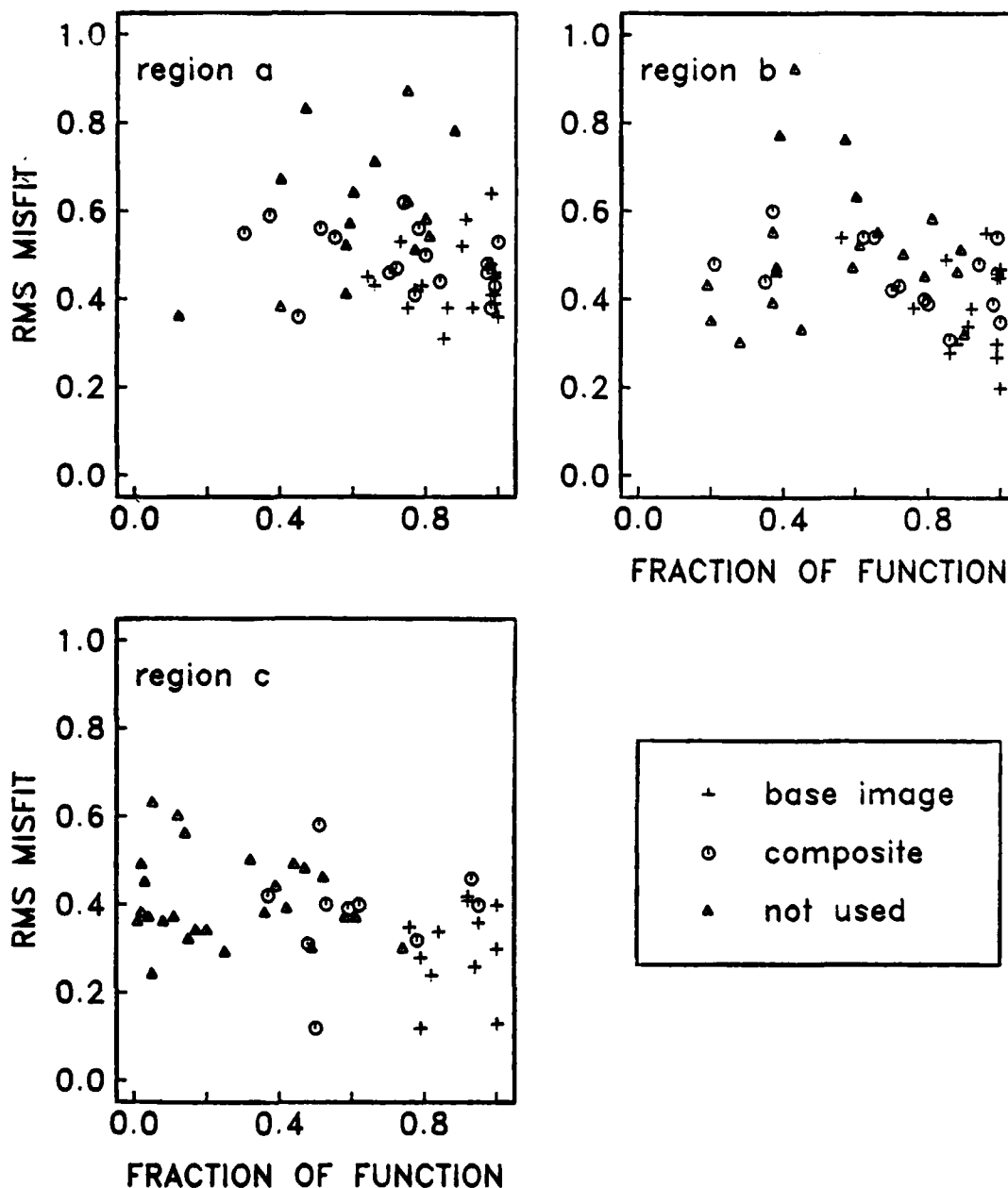


FIG. 7.3 MISFIT OF IMAGES TO FIRST FOUR EOF'S

For each image the rms misfit to the first four EOF's is plotted against the fraction of the region which coincided with the cloud-free data. The symbols show whether the image was used as a base image, as a supplementary image in a composite, or not used for the EOF calculation. Only a few images, which were not used to compute the EOF's, had noticeably higher misfit.

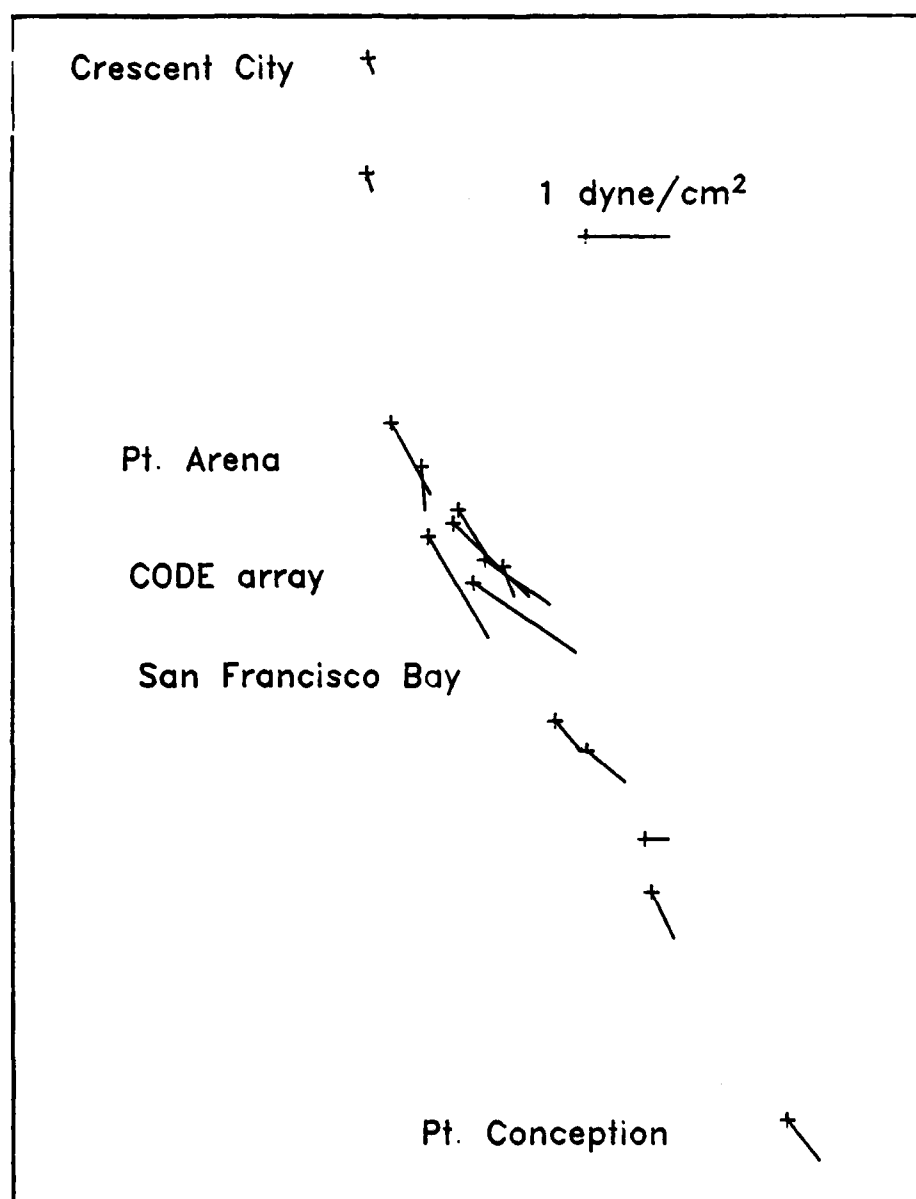


FIG. 7.4 MEAN WIND STRESS

For each location shown in Figure 7.1 the mean wind stress for the record was computed. The "+" gives the location of the measurement and the tail of the stress vector. The mean of each record was subtracted before the EOF's were computed.

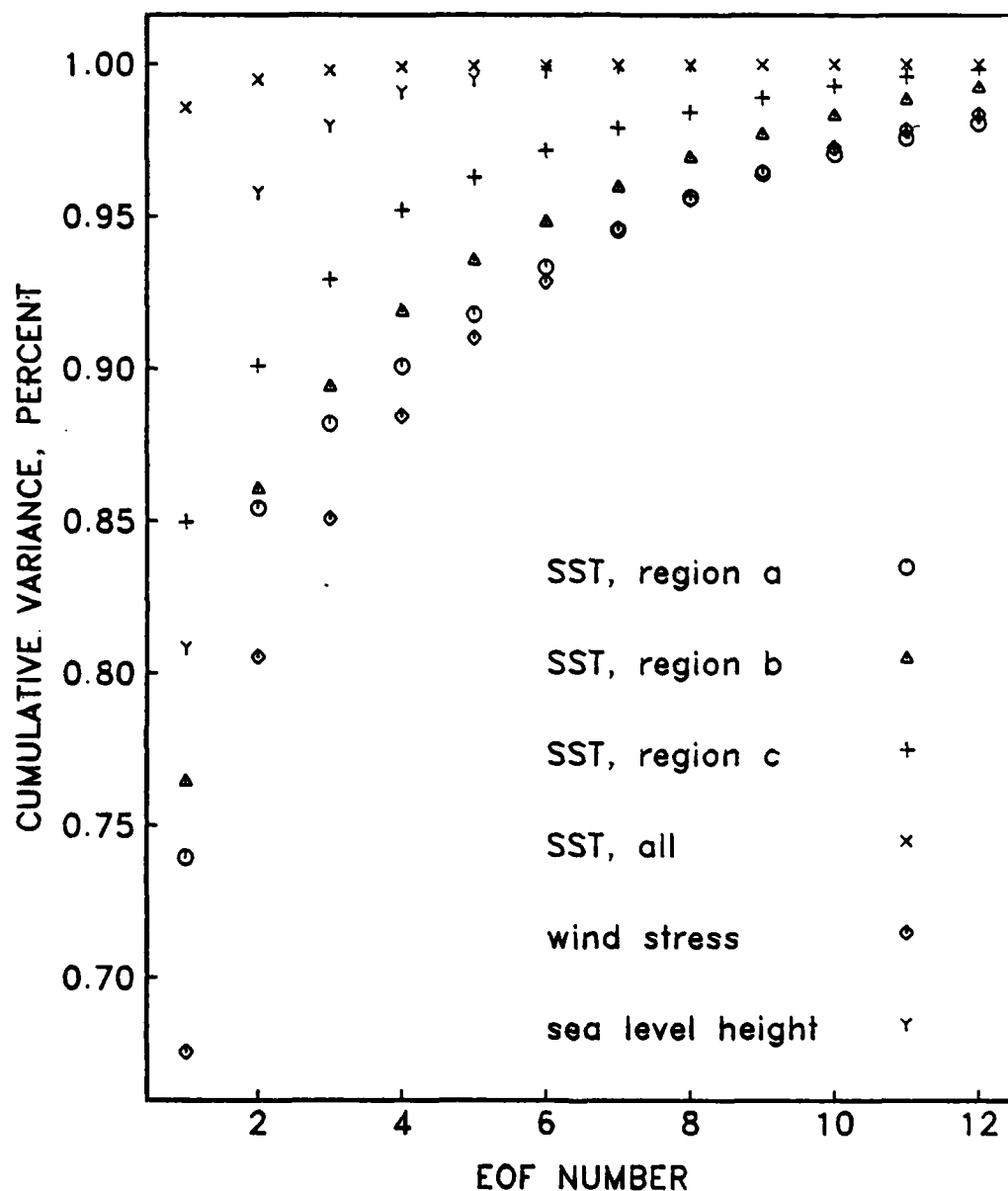


FIG. 7.5 CUMULATIVE VARIANCE IN EOFS FOR ALL VARIABLES

For each EOF decomposition the cumulative percent of variance is plotted against the number of functions. For example, the first SST function for region C described 85 % of the total variance and the first two functions combined described about 90 % of the variance.

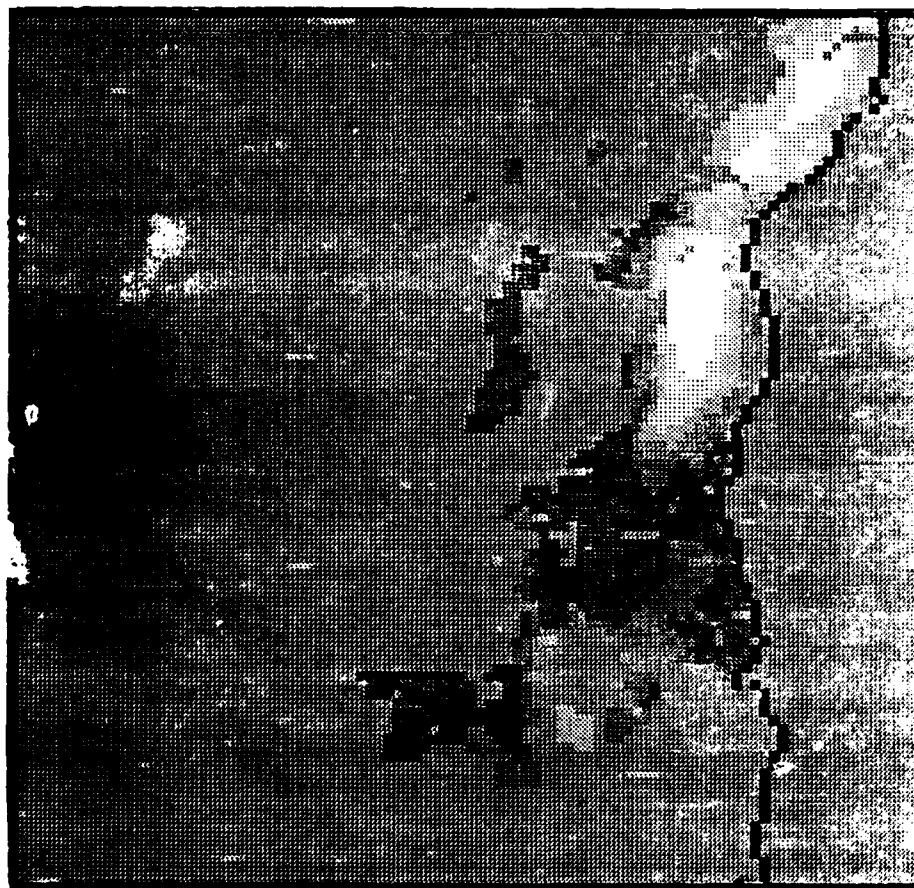


FIG. 7.6a SST EOF 2 FOR REGION A

Second empirical orthogonal function of sea-surface temperature for part of the area shown in Figure 7.1. Light shades are negative (cold) anomalies and dark shades are positive (warm) anomalies. The medium gray area, which for reference has a value of zero, was not included in region A. The dark line at the right is the coastline.

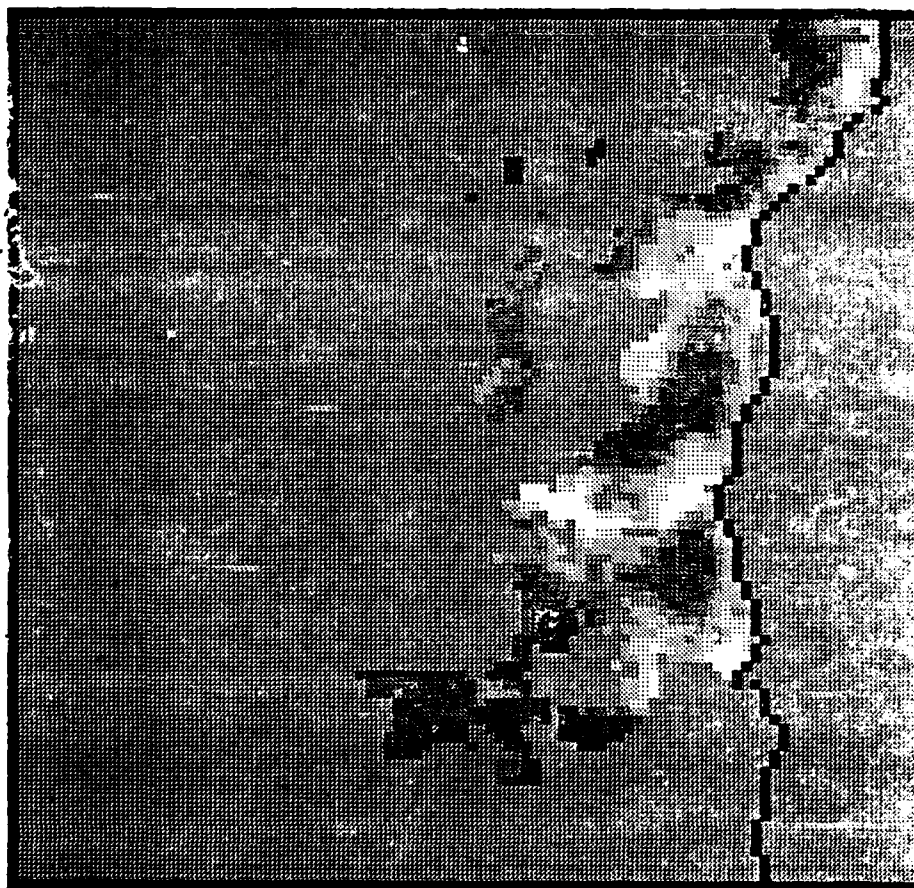


FIG. 7.6b SST EOF 3 FOR REGION A

Same as Figure 7.6a, except third function for region A.

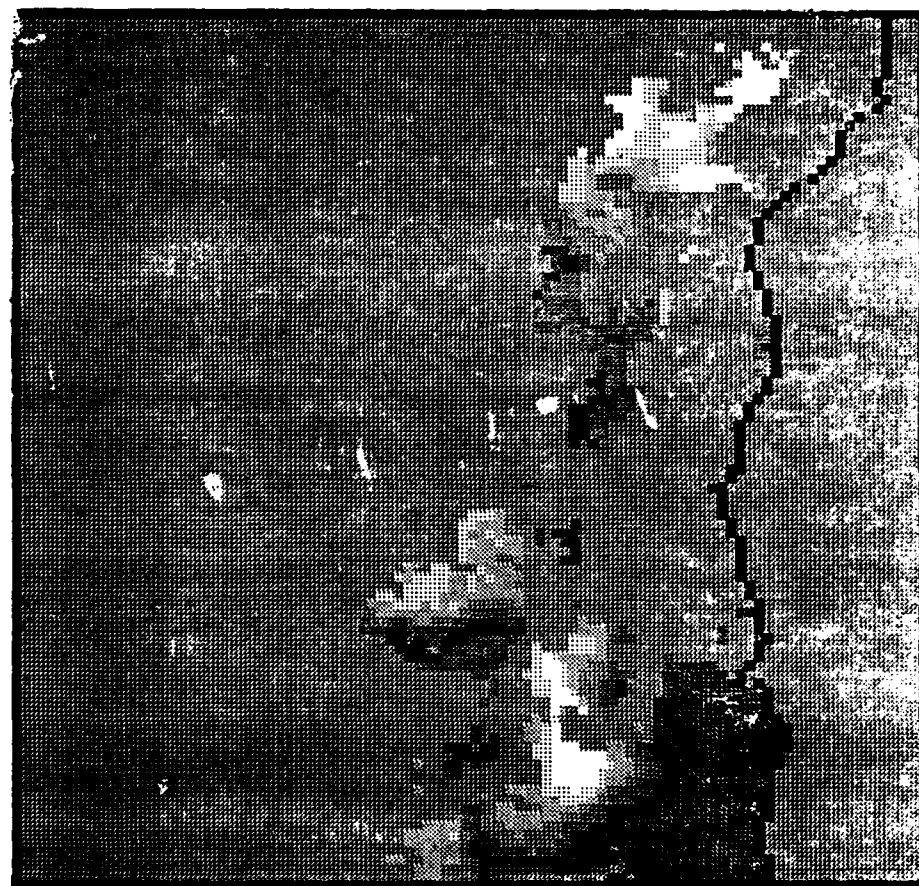


FIG. 7.6c SST EOF 2 FOR REGION B

Same as Figure 7.6a, except second function for region B.

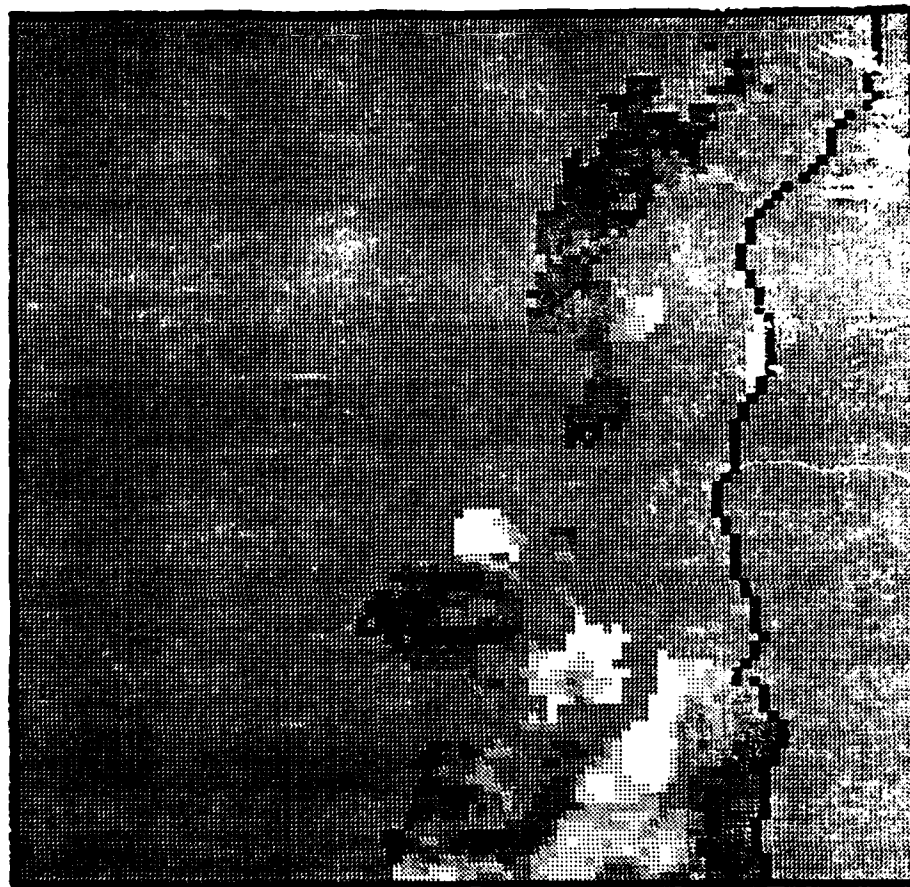


FIG. 7.6d SST EOF 3 FOR REGION B

Same as Figure 7.6a, except third function for region B.

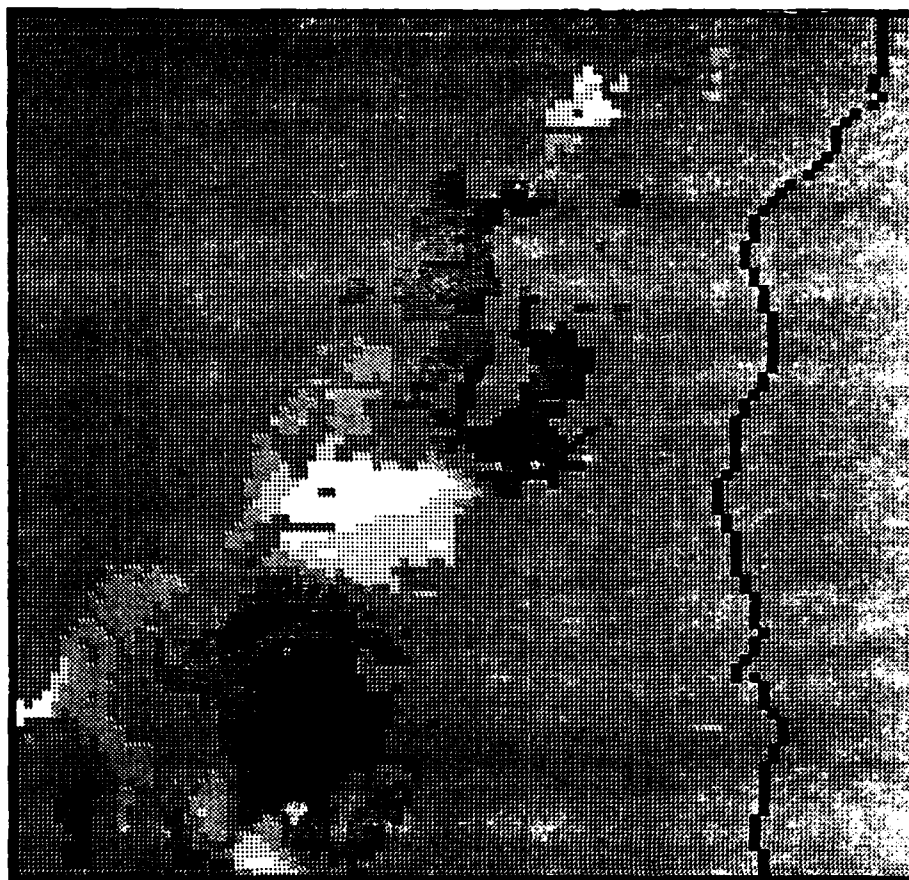


FIG. 7.6e SST EOF 2 FOR REGION C

Same as Figure 7.6a, except second function for region C.

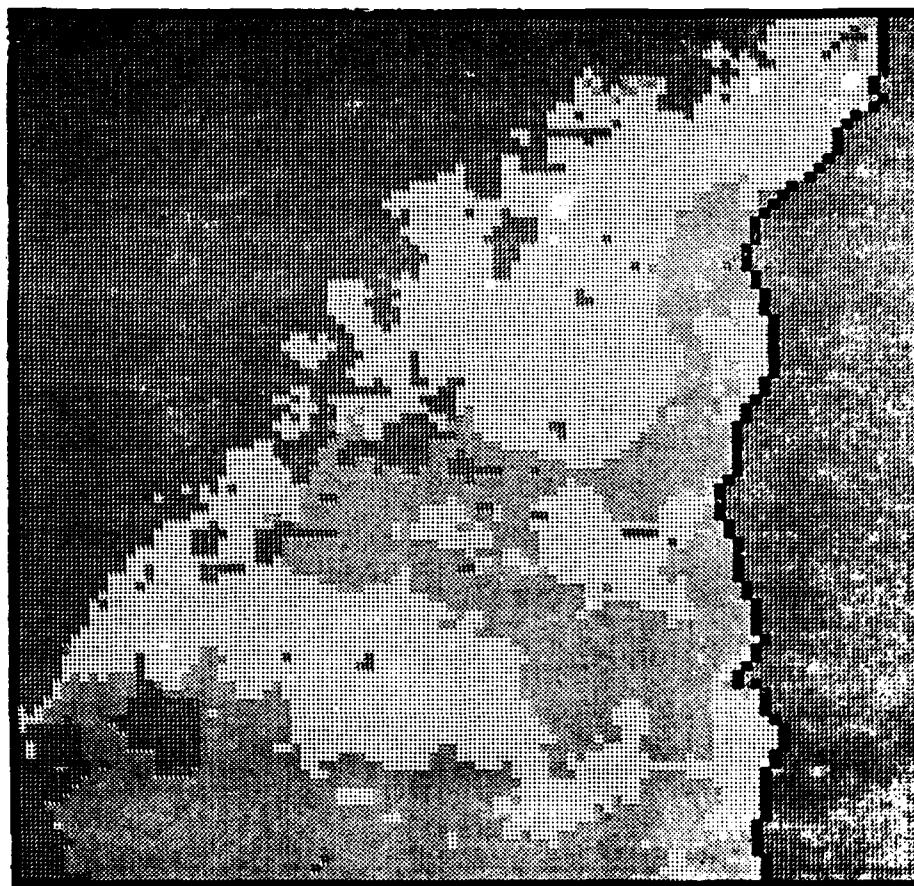


FIG. 7.6f SST EOF 1 FOR REGIONS A,B AND C

Same as Figure 7.6a, except first function for combined regions A, B and C.



FIG. 7.6g SST EOF 2 FOR REGIONS A,B AND C

Same as Figure 7.6a, except second function for combined regions A, B and C.

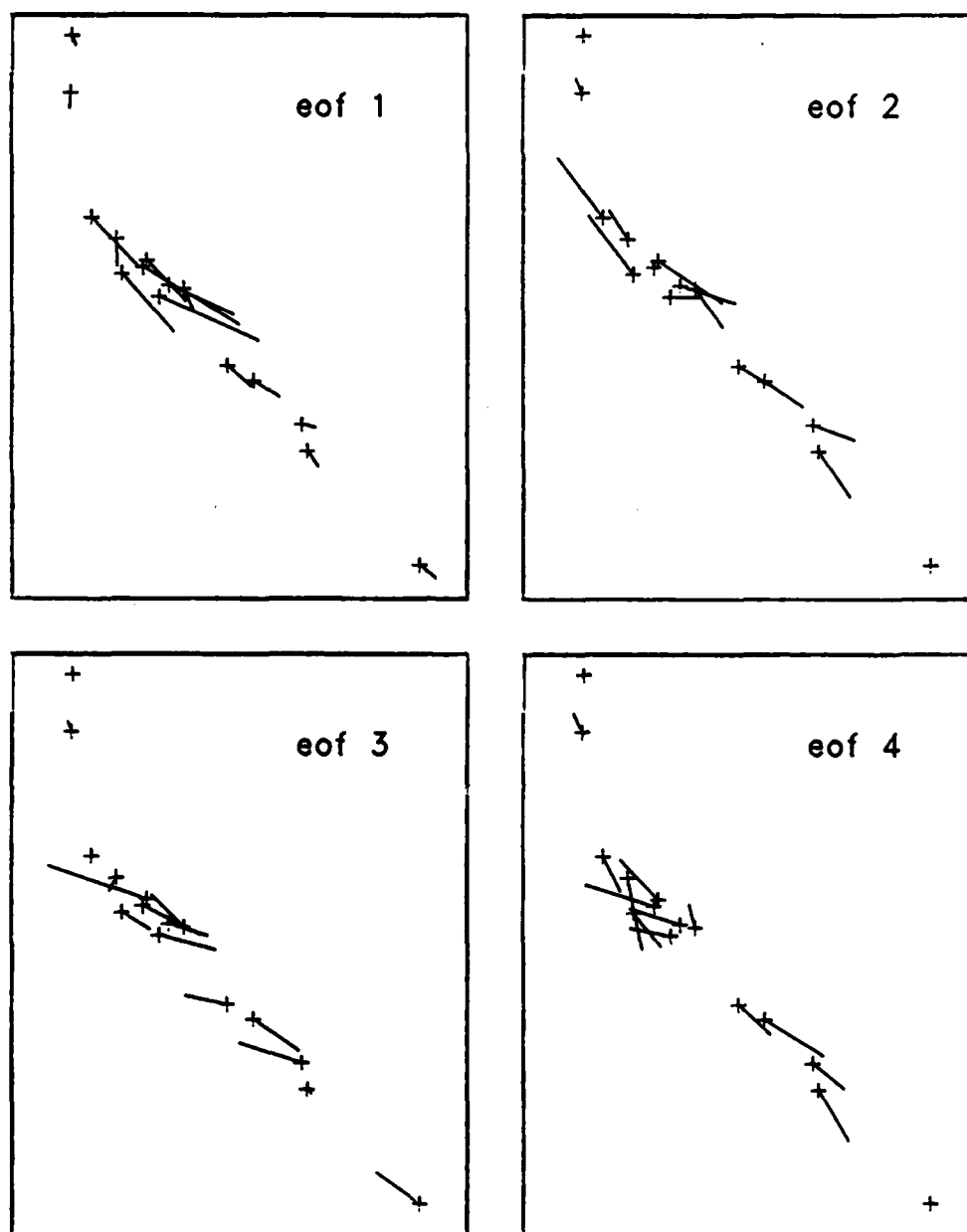


FIG. 7.7 WIND EOF'S 1 - 4

Empirical orthogonal functions for wind stress for the locations shown in Figure 7.1. The horizontal direction has been expanded to make the individual vectors visible. The "+" marks the location of the stress anomaly and the tail of the vector.

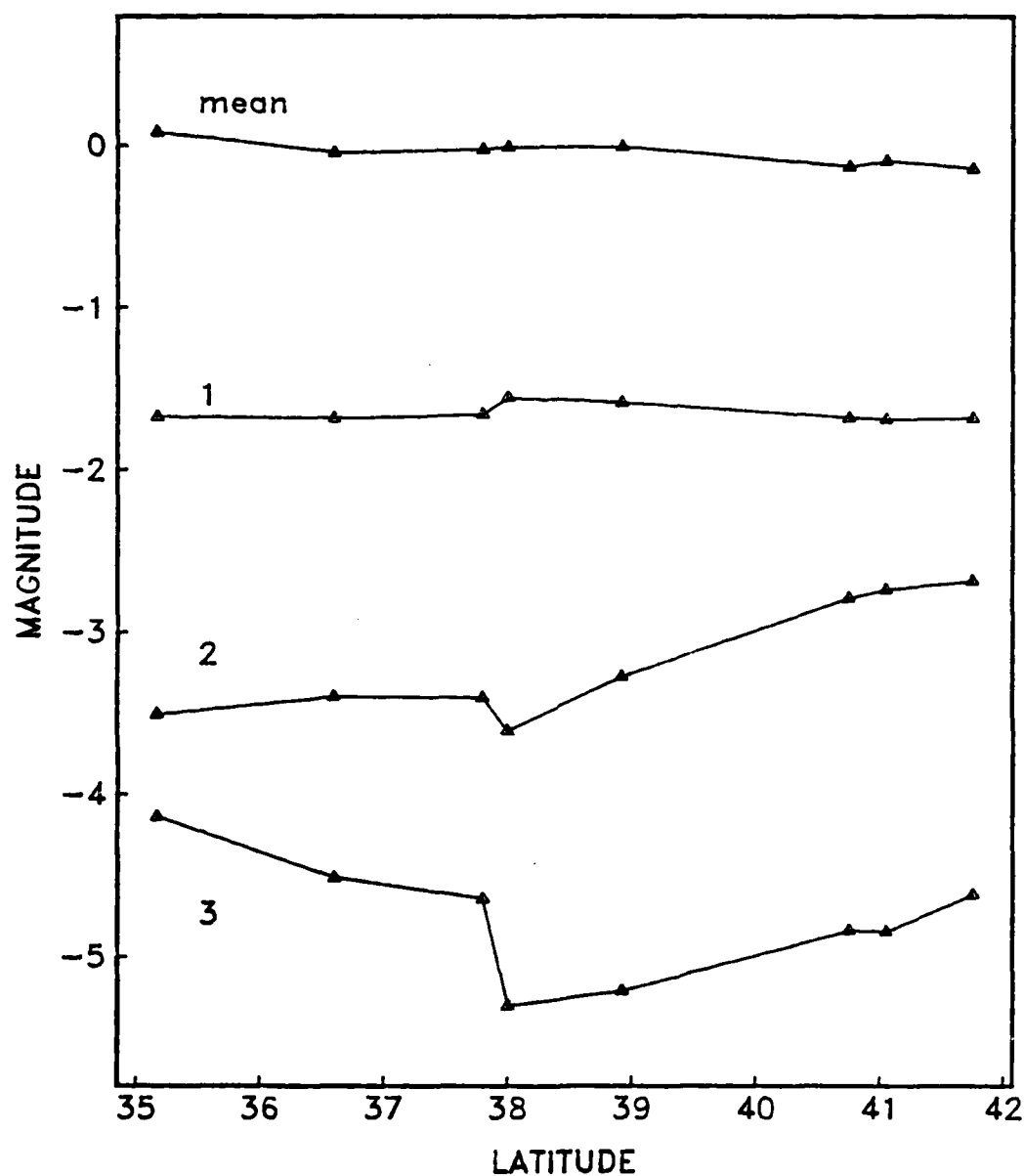


FIG. 7.8 SEA LEVEL HEIGHT, MEAN AND EOF'S 1-3

Mean and empirical orthogonal functions of coastal sea level from tide gauges at locations shown in Figure 7.1. The triangle marks the mean value or anomaly at the gauge location, which is identified by its latitude. The mean was removed before the EOF's were computed.

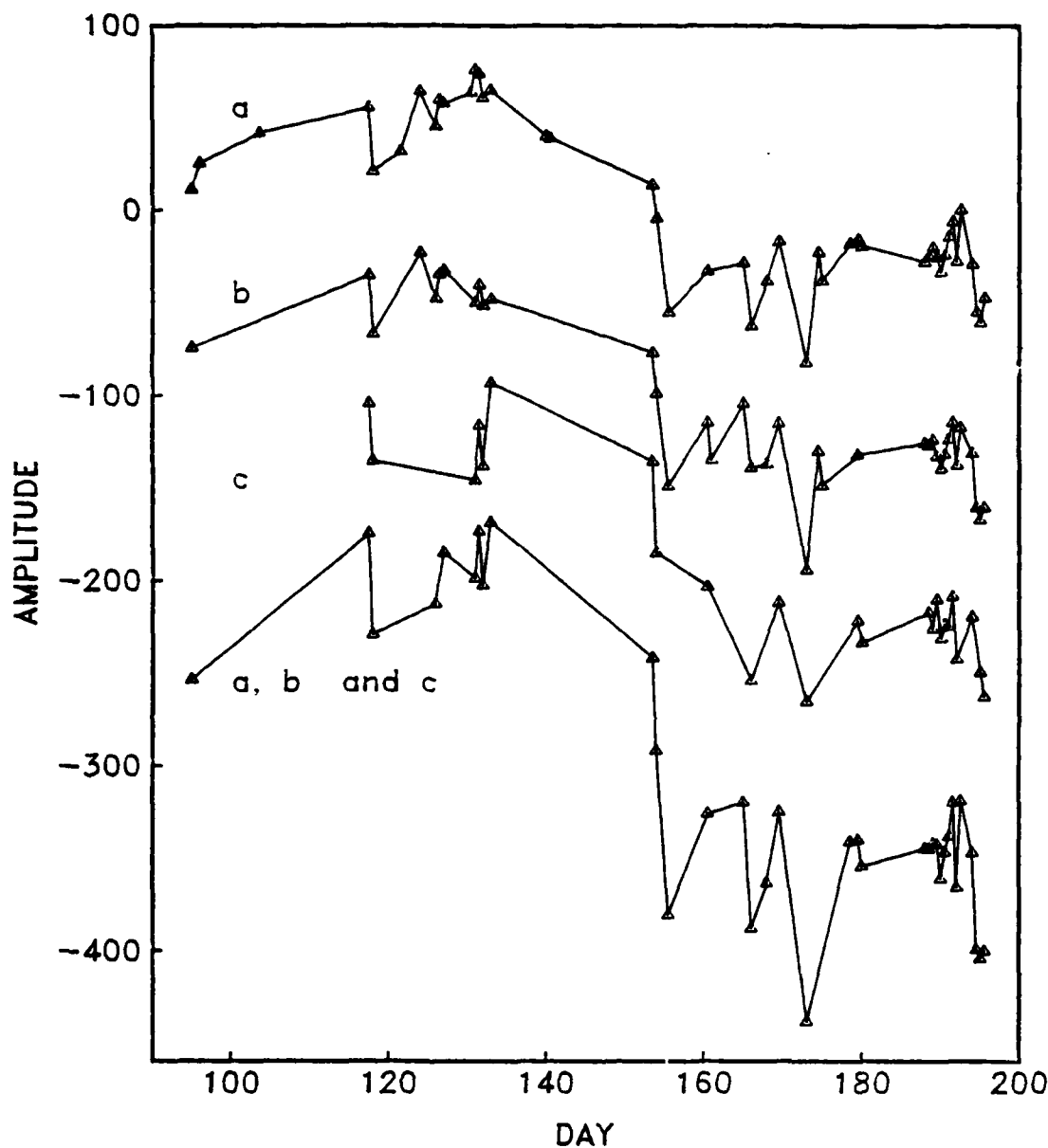


FIG. 7.9a AMPLITUDES FOR SST EOF 1

Time-varying amplitudes for the first sea-surface temperature EOF for each region and the combined regions. The triangles denote computed amplitudes for images which covered at least half of the region. Region A amplitudes are shown with the correct y-axis; other amplitudes are offset for clarity. Positive amplitudes give the positive and negative anomalies as described in Figure 7.6. Negative amplitudes reverse the signs of the anomalies.

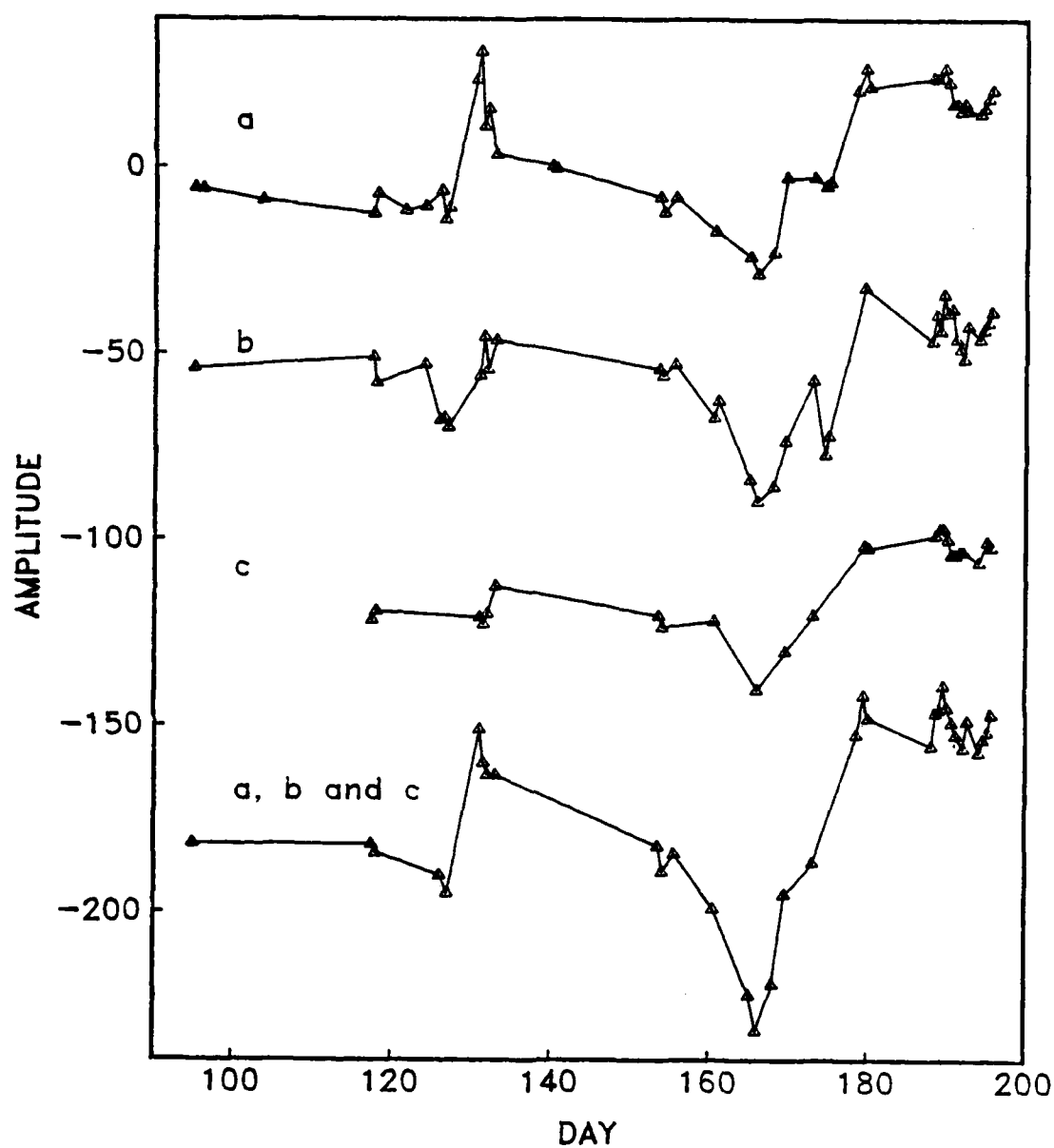


FIG. 7.9b AMPLITUDES FOR SST EOF 2

Same as Figure 7.9a, except for second EOF.

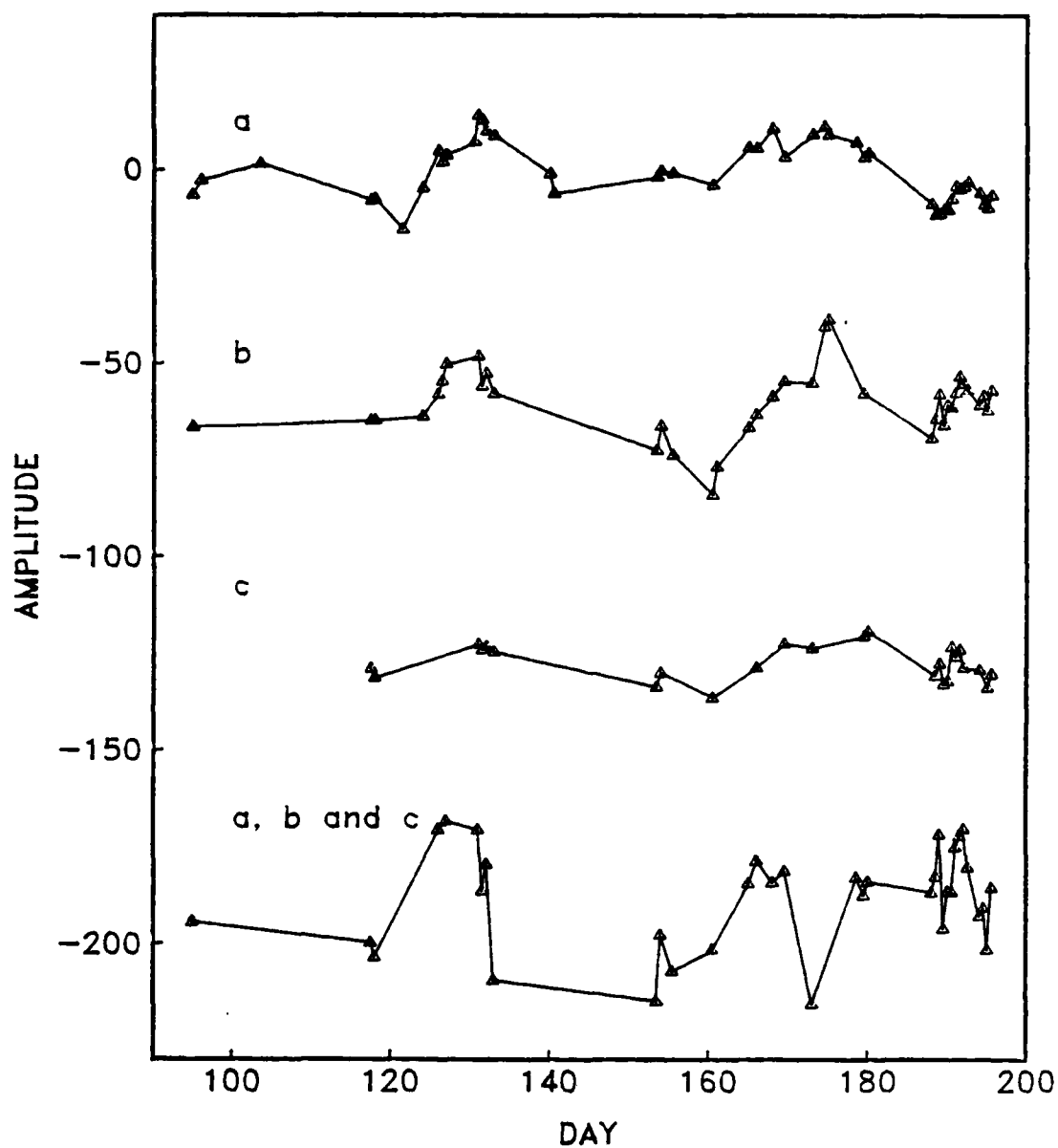


FIG. 7.9c AMPLITUDES FOR SST EOF 3

Same as Figure 7.9a, except for third EOF.

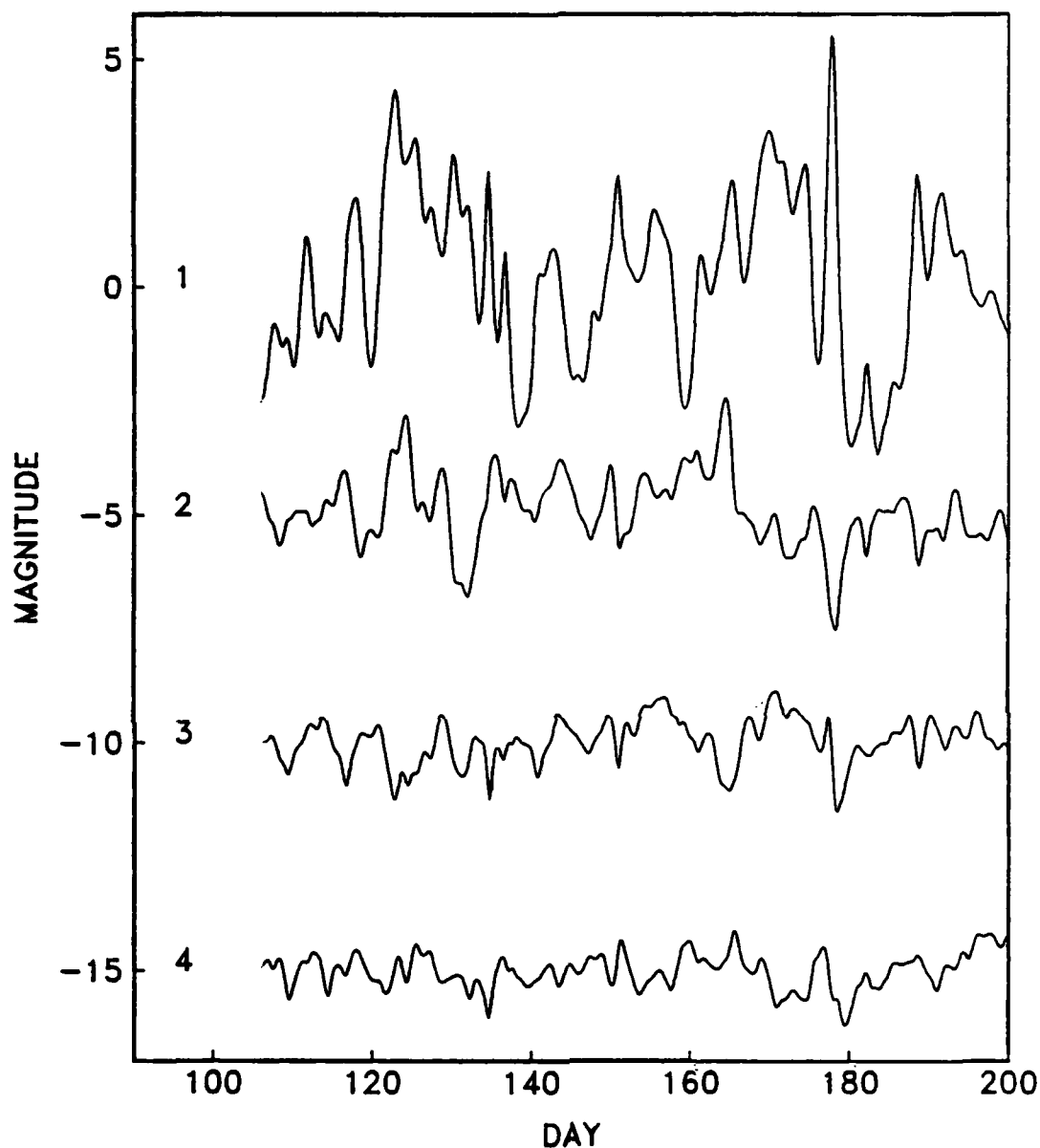


FIG. 7.10 AMPLITUDES FOR WIND EOF'S 1 - 4

Time-varying amplitudes for the wind stress EOF's. The first amplitudes are shown with the correct y-axis; other amplitudes are offset for clarity. Positive amplitudes give the wind stress anomalies as shown in Figure 7.7; negative amplitudes reverse the vectors. For example, a positive amplitude for the first EOF gives wind stress anomalies toward the southeast. A negative amplitude gives wind stress anomalies toward the northwest.

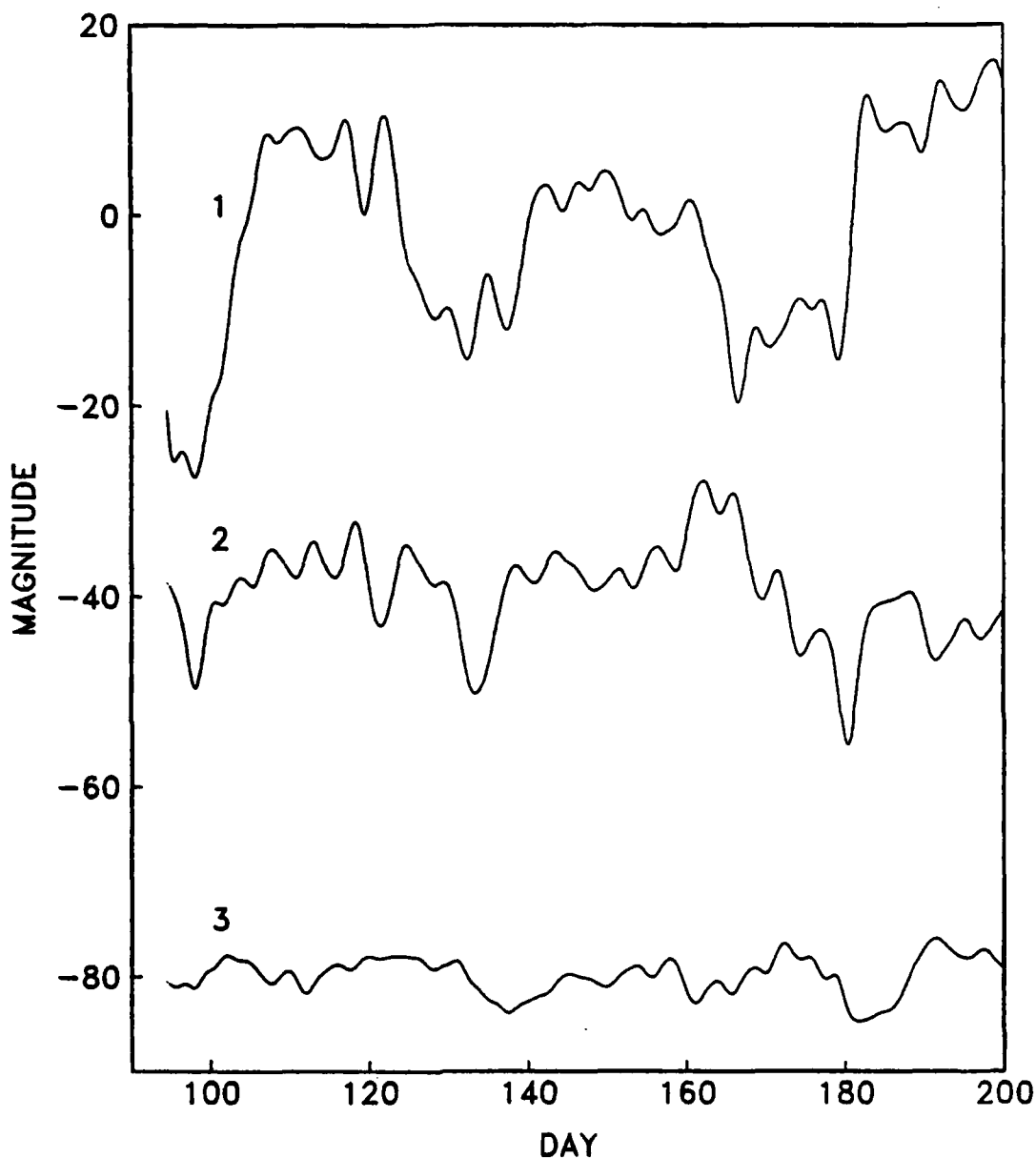


FIG. 7.11 AMPLITUDES FOR SLH EOF'S 1 - 3

Time-varying amplitudes for sea-level height EOF's. The amplitudes for the first function are plotted with the correct y-axis; others are offset for clarity. Positive amplitudes give the anomalies with the sense shown in Figure 7.8. Negative amplitudes reverse the sign of the anomaly.

Table 7.1 Wind Bias Statistics

category number	mean m s^{-1}	variance	percent in category	
			wind record	images (no. images)
1	≤ 6	≤ 4	15	12 (7)
2	all	> 4	17	18 (10)
3	6-10	≤ 4	37	14 (8)
4	> 10	≤ 4	31	56 (31)

Wind conditions for each day in representative wind records were defined by their mean and variance over the previous two days. A comparison of the percentage of days in each category with the percentage of images in each category shows that the images are biased toward categories 2 and 4. The number of images in each category is also shown.

Table 7.2 Statistics of Spatial Regions for EOF's

Region	No. of spatial pts.	Images from wind category				
		1	2	3	4	total
A	1382	3	4	4	8	19
B	1479	2	2	2	9	15
C	2124	1	3	2	7	13

The sea surface temperature EOF's were computed over three non-overlapping spatial regions. The number of points in each region and the number of images from each wind category (defined by Table 7.1) is shown for each region.

CHAPTER 8

VELOCITY ESTIMATION

The close relationship shown in Chapter 6 between the sea-surface temperature from satellite images and the surface velocity field suggests that velocities can be retrieved from a series of images. There are several types of information in a series of temperature maps; much of which is qualitative. The surface velocity is generally parallel to isotherms and its magnitude appears largest at the strong temperature fronts. Along these fronts small shear eddies indicate the relative flow of cold water to warm water by the sense in which they entrain cold water, i.e., cyclonic or anti-cyclonic. Larger eddies have an apparent direction of rotation also and an examination of numerous eddies reveals that the cyclonic eddies are generally colder than nearby anti-cyclonic eddies. This consistent relationship suggests a geostrophic balance where temperature represents density. From image to image one can see a drift of features, such as the motion of the cold eddy in Figure 6.5, which had a drift speed of about 10 km/day. Its rotation speed, estimated from the drifter tracks, was about three times as large (Davis, 1983).

The purpose of this chapter is to extract quantitative velocity estimates from the satellite data using no in situ data. Additional measurements could undoubtedly improve the estimates described here. This chapter demonstrates, at least for the CODE data, how much velocity information the satellite images alone contain.

8.1 The Inverse Problem

Computing a velocity field from the temperature maps can be viewed as an inverse problem where the forward problem is: given a velocity field and an initial temperature map, compute the temperature map at a later time. However, the SST maps cannot be inverted in general for the velocity field because the forward problem is not well-understood. Given only the surface velocity field one cannot uniquely determine the evolution of the SST field. Processes which are not specified by the surface velocity contribute to temperature changes: heat flux in and out of the surface, vertical mixing and diffusion. The velocity field, unlike the data, is three-dimensional with upwelling or downwelling creating heat sources or sinks.

But assume that under certain special conditions the forward problem is well-defined by the conservation of temperature, i.e., horizontal advection determines the evolution of the SST field,

$$\frac{\partial T}{\partial t} + \mathbf{u}_H \cdot \nabla_H T = 0 \quad (8.1)$$

where the velocity field is strictly two-dimensional in the horizontal plane. This forward problem, relating changes in temperature to known horizontal velocities and temperature gradients, is linear and the inverse problem of finding the velocities can be solved using the well-defined techniques of linear inverse theory (Parker, 1983). As in most inverse problems the solution will not be unique, but a serious problem with this inversion is that a good estimate of the actual velocity field is an annihilator. An annihilator is a solution which does not change

the data (Parker and Huestis, 1974). This can be seen by breaking the velocity into components

$$\underline{u}_H = \underline{u}_p + \underline{u}_c \quad (8.2)$$

where \underline{u}_p is locally parallel to the isotherms and \underline{u}_c is perpendicular to the isotherms. Then equation 8.1 becomes

$$\frac{\partial T}{\partial t} + \underline{u}_p \cdot \bar{\nabla}_H T + \underline{u}_c \cdot \bar{\nabla}_H T = 0 \quad (8.3)$$

where the second term is identically zero. Flow parallel to the isotherms moves fluid of a given temperature to an area of the same temperature without any effect on the SST map. As can be seen in the surface velocity measurements in Figures 6.2 to 6.5, the velocity parallel to the isotherms is the larger component. Deviations of the surface velocities from the annihilator are small because the cross-isotherm drift of features is small compared with typical measured velocities ($\sim 5 \text{ cm s}^{-1}$ compared with 40 cm s^{-1}). Therefore in this idealized case, although an inverse method can be used to compute a cross-isotherm velocity field, the larger problem of the along-isotherm velocity must be solved in some other way.

8.2 Estimation Using a Simple Model

There are some properties of the temperature field, particularly in the CODE region, which suggest that surface velocities can be estimated by assuming a simple model for the along-isotherm velocity.

The model requires that the surface temperature gradients extend deep into the water column and that there is a simple relationship between temperature and density. These assumptions were valid for a period in early July, 1981, when a hydrographic survey was conducted in the CODE area (Olivera, et al., 1982).

Temperature is not a passive tracer of the velocity field; it participates in the force balance through its relationship to density

$$\partial \rho = - \beta \partial T \quad (8.4)$$

where $\beta \approx 2 \times 10^{-4} \text{ deg}^{-1}$ when salinity effects are neglected. Density appears in the dynamical equations which govern velocity; thus, a model which relates density to velocity can be used to relate temperature to velocity.

On scales large enough to assume a geostrophic balance surface velocities may be proportional to $\bar{\nabla} T$ through the thermal wind equation. This equation can be obtained from the momentum equations 1.7 by neglecting time-dependence and stress, taking vertical derivatives of 1.7a and b, and substituting 1.7c for the pressure term. The resulting equation is

$$\frac{\partial u_H}{\partial z} = \frac{g}{\rho f} \mathbf{k} \times (\bar{\nabla} \rho)_p \quad (8.5)$$

where \mathbf{k} is the unit vector in the z-direction and where the gradient is taken along lines of constant pressure (Pedlosky, 1979). The thermal

wind relationship describes the vertical shear of the horizontal velocity in terms of horizontal density gradients, assuming the velocity to be geostrophic and non-divergent.

For the large scale we now have a relationship between the vertical derivative of horizontal velocity and the horizontal gradient of density. Some additional assumptions, which are not valid in general, are required to relate horizontal velocity directly to horizontal temperature gradients. The first assumption, which eliminates the need to measure density, is that either salinity effects are negligible, or that the T-S relationship is sufficiently constrained that equation 8.4 is the total derivative

$$dp = - \beta dT \quad (8.4')$$

As discussed in Chapter 6 in the CODE region salinity and temperature were always anti-correlated so that density gradients were larger than would be expected using the above value of β and the measured temperature gradients. Olivera (1982) found that temperature and salinity had a correlation of -0.73 at the surface, that temperature and density fronts generally coincided and that temperature was more important than salinity in determining density. These results suggest that 8.4' is a good approximation here. Using 8.4', where now β includes the effects of salinity and is larger than $2 \times 10^{-4} \text{ deg}^{-1}$, equation 8.5 becomes

$$\frac{\partial u_H}{\partial z} = - \frac{g\beta}{\rho_0 f} k \times (\nabla T)_p . \quad (8.6)$$

Because the satellite images give no information in the vertical, some assumptions about vertical structure must be made. Winds were strong during CODE and the surface layers were well-mixed in the vertical: from top-to-bottom on the shelf and to depths of 50 m over the slope. Olivera (1982) showed that temperature fronts were about 50 % weaker at depths of 50 m than at the surface, and that the strong gradients at these depths were in nearly the same location as those at the surface. Therefore, assume that the horizontal temperature gradient at depth z has the same location as at the surface, but it is weaker and is rotated through an angle, θ , with respect to the surface

$$\bar{\nabla} T(z) = |\bar{\nabla} T_s| f(z) (\cos(\gamma - \theta), \sin(\gamma - \theta)) \quad (8.7)$$

where

$$\bar{\nabla} T_s = |\bar{\nabla} T_s| (\cos \gamma, \sin \gamma)$$

is the gradient at the surface. Then from equation 8.6

$$u = -C |\bar{\nabla} T_s| \int_{-D(x,y)}^0 f(z) \sin(\gamma - \theta(z)) dz \quad (8.8a)$$

$$v = C |\bar{\nabla} T_s| \int_{-D(x,y)}^0 f(z) \cos(\gamma - \theta(z)) dz \quad (8.8b)$$

where

$$C = \frac{g\beta}{\rho_0 f}$$

D is the depth at which temperature and velocity gradients vanish, and

$$\underline{u}_H = (u, v)$$

If $f(z)$ is a strongly-decreasing function of depth, then the near-surface gradients make the largest contribution to the surface velocity. Therefore assuming $f(z)$ to be constant for the integration will not qualitatively change the results and will make D an equivalent depth. If θ is a small angle which can be parameterized as

$$\theta = -\alpha z \quad (8.10)$$

where α is a constant and, using the approximations,

$$\sin(\gamma - \theta) \approx \sin \gamma \left(1 - \frac{\theta^2}{2}\right) - \theta \cos \gamma, \quad (8.11a)$$

$$\cos(\gamma - \theta) \approx \cos \gamma \left(1 - \frac{\theta^2}{2}\right) + \theta \sin \gamma \quad (8.11b)$$

equations 8.8 can be integrated to give

$$u = C |\bar{\nabla} T_s| \left[-D \sin \gamma + \frac{\theta_D^3}{6\alpha} \sin \gamma + \frac{\theta_D^2}{2\alpha} \cos \gamma \right] \quad (8.12a)$$

$$v = C |\bar{\nabla} T_s| \left[D \cos \gamma + \frac{\theta_D^3}{6\alpha} \cos \gamma - \frac{\theta_D^2}{2\alpha} \sin \gamma \right] \quad (8.12b)$$

The first term is the surface velocity parallel to the isotherms assuming the surface gradients extend downward with no rotation, the second term is a correction to that flow and the third term is a velocity across the isotherms. The magnitude of the velocity is proportional to the surface temperature gradient everywhere and the constant of proportionality parameterizes the equivalent depth to the level of no motion, as well as β , the change in density with temperature.

8.3 A Two-Step Method for Velocity Estimation

A pair of images from early July were selected for the estimates. The first image of the pair is shown in Figure 8.1. The time derivative of temperature was approximated by a finite difference from the pair of images, which were 12 hours apart. Equations 8.12 suggest a formula for obtaining an estimate of the velocity:

- 1) determine the cross-isotherm flow using the conservation of temperature, equation 8.1
- 2) given the cross-isotherm flow, find the component of velocity parallel to the isotherms which makes the magnitude of the velocity equal to the constant, C , times the temperature gradient

The constant, $C(x,y)$, was obtained by comparing the displacement of small features with the local temperature gradient. On scales too small to be geostrophically balanced, features of about 5-10 km in diameter are advected by the large-scale geostrophic velocity. The displacement of small features from one image to the next gives a direct measurement of velocity for a few locations. The displacements of

features which could be followed from one image to the next image are shown in Figure 8.2. The X marks the original location of the feature and the other end of the line marks its location 12 hours later. A simple function for C was computed as a least-squares fit to the displacement of the small features

$$\frac{\text{displacement}}{\delta t} = C(x,y) |\bar{\nabla} T_s|$$

where the δt was 12 hours and the local temperature gradient, $\bar{\nabla} T_s$, was computed from the first image.

A stream function, $\bar{\psi}$, was used to represent the non-divergent horizontal velocity field where

$$\underline{u}_H = \underline{k} \times \bar{\nabla} \bar{\psi} \quad (8.13)$$

The velocity field was required to 1) conserve temperature, 2) be proportional to the temperature gradient, and 3) satisfy a boundary condition at the coast. Using $\bar{\psi}$, these constraints can be written

$$\delta T = - (\underline{k} \times \bar{\nabla} \bar{\psi}) \cdot \bar{\nabla} T \quad (8.14)$$

$$C(x,y) |\bar{\nabla} T| = |\bar{\nabla} \bar{\psi}| \quad (8.15)$$

$$\bar{\psi}_y = 0, \quad \text{at the coast} \quad (8.16)$$

where δT is the change in temperature from one image to the next and the

8.16 is the requirement that there be no flow through the coast.

Equation 8.15 is not a linear constraint; to make the problem linear the stream function was estimated in two steps. First, the cross-isotherm velocity, \underline{u}_c , was computed as a least-squares solution to equations 8.14 and 8.16. Then a new constant, $C'(x,y)$, was computed using this solution

$$C'^2 |\bar{\nabla} T|^2 + |\underline{u}_c|^2 = C^2 |\bar{\nabla} T|^2 \quad (8.17)$$

or

$$C'^2 = C^2 - \frac{|\underline{u}_c|^2}{|\bar{\nabla} T|^2} \quad (8.17')$$

The constant, C' , multiplied by the along-isotherm velocity, makes the total velocity proportional to C times the temperature gradient. Equation 8.15 then becomes

$$C' |\bar{\nabla} T| = \bar{\nabla} \psi \cdot \bar{\nabla} T \quad (8.18)$$

which is a linear constraint for ψ . The form chosen for ψ was a two-dimensional truncated Fourier series where the highest wavenumber corresponded to a wavelength of 64 km.

8.4 Velocity Estimates and Suggestions for Improving the Method

A solution for ψ was obtained by solving equations 8.14, 8.16, and 8.18 simultaneously. The equations were scaled in a manner similar to that discussed by Provost (1983) to selectively enforce any of the constraints more stringently. Solutions of the cross-isotherm stream function are shown in Figures 8.3 and 8.4 for different weighting of equations 8.14 and 8.16. The figures show the velocities at each location marked by an X, which is the tail of the velocity vector. The vectors are scaled so that the length of the line is the displacement in 12 hours. The largest velocities shown in the cross-isotherm fields are about 5 cm sec^{-1} . The weights in the figures, w_1 , w_2 , w_3 , correspond to equations 8.14, 8.18 and 8.16, respectively. Figure 8.3 shows the cross-isotherm flow for equal weighting of the conservation of temperature and the boundary condition. Figure 8.4 shows an increased weight given to the boundary condition. The increased weight for the boundary condition caused velocities near the coast (and also at the left edge of the figure) to turn parallel to the coast. Enforcing the boundary condition stringently may not be desirable for these estimates because in this two-dimensional model, flow through the boundary may represent coastal upwelling, which is a three-dimensional process.

The total velocity field is shown in Figure 8.5, in which the arrows represent the displacement in 6 hours. The maximum velocity shown is about 40 cm sec^{-1} . Figure 8.5 shows the total velocity for equal weighting of the three constraints; again the stronger boundary condition forced the velocity to be parallel to the boundaries (not shown). Increasing the weight for the conservation of temperature

relative to the thermal wind constraint (8.18) simply produced a field which looked like the cross-isotherm field; this result is not shown.

There was generally good correspondence between the computed fields and the velocity measurements from the doppler log and the surface drifters. The cold eddy at the top of the image near the coast is well-defined; this is the eddy shown in Figure 6.5 which entrained the surface drifters. A map of the doppler log velocities computed by Kosro is contained in Olivera (1982). The flow near the coast was strongly southward, although the region of maximum southward flow was too far offshore and did not extend far enough south. The region where the flow reversed abruptly from southward to northward agreed well with the location of the flow-reversal observed in the doppler velocities as did the region of strong offshore flow; however, the magnitudes of the velocity estimates were smaller than those computed by Kosro. Maximum speeds were too small by a factor of two; typical speeds were slightly better. The magnitudes of the velocity came directly from the apparent motion of small features. If these small features were shear eddies, for example, then the observed motion was a drift speed rather than the speed of a fluid particle. Shear eddies travel at a speed intermediate between the fluid speeds on either side of a front; the rotation rate of a small eddy, which cannot be measured from the images, corresponds to the speed of a fluid particle (L. Armi, personal communication). Thus one would systematically underestimate surface velocities by following small eddies.

The region near Pt. Reyes was poorly described by the estimated velocities; there was a breakdown in the model which was apparent as a

negative value for C'^2 . Another indication of a problem in this region was the difficulty in locating features which were recognizable from one image to the next. The drifters showed an offshore flow and the one feature in Figure 8.2 that could be followed in this region moved offshore also; however, the velocity estimates consistently showed onshore flow. The constant, $C(x,y)$, decreased in both the onshore and southward directions so that near Pt. Reyes it was only about one-fifth its maximum value. This is consistent with a decrease in the depth of the water column; however, the cross-isotherm velocity computed in the first step was larger than $C \sqrt{T}$. This may have been due to poor resolution of the temperature gradients: the gradient was estimated as a finite difference over 7 km. Or, the temperature change may have been due to local heating or a change in atmospheric conditions.

Another breakdown of this velocity estimate occurred at the boundaries where the solution must be periodic due to the choice of a Fourier decomposition for the stream function. The strong gradients on the left edge of the image in Figure 8.1 may cause the large velocities near the coast. A relatively simple solution to this problem is a non-periodic basis for the streamfunction: an appropriate basis would be the empirical orthogonal functions (EOF's) for the set of July images. The composite EOF's computed in Chapter 7 would not be adequate because too much of the variance was contained in the first two modes.

There is another velocity component which was neglected by this model: the flow field is divergent. Although horizontal non-divergence is frequently a good assumption for a velocity estimate on this scale, because this is an area of intense upwelling, there are sources of cold

water (or sinks for warm water), particularly near the coast. One area south of Cape Mendocino is usually colder than any area around it and is therefore probably a source of cold water from upwelling. The motion resulting from a source or sink would most likely be across isotherms because vertical fluid velocities are too small to form a jet at the surface and because the water near a source (sink) would have a consistently colder (warmer) temperature. One solution is to relax the non-divergence constraint on the cross-isotherm velocity, or to add a divergent correction term to the velocity to better satisfy the conservation of temperature.

A related question, which can be answered using linear inverse theory, is how divergent the velocity field must be to satisfy conservation of temperature. Using equation 8.1 one could solve for the cross-isotherm velocity with the smallest horizontal divergence which satisfied the equation within a given misfit. One could then begin to answer the question of where upwelling occurs: near the boundary as coastal upwelling or offshore as Ekman suction.

The qualitative agreement between these first velocity estimates using only satellite data and the surface velocity measurements suggests some optimistic conclusions. If the assumptions of the model used in the estimate are valid for a given region, velocity maps with the right features can be made from satellite data alone. Those assumptions include 1) a simple T-S relationship and 2) temperature gradients which extend deep into the ocean. Velocity maps from satellite data will probably underestimate the magnitudes of the velocities and may not be accurate near the coast. The model used to compute velocities parallel

AD-A135 462

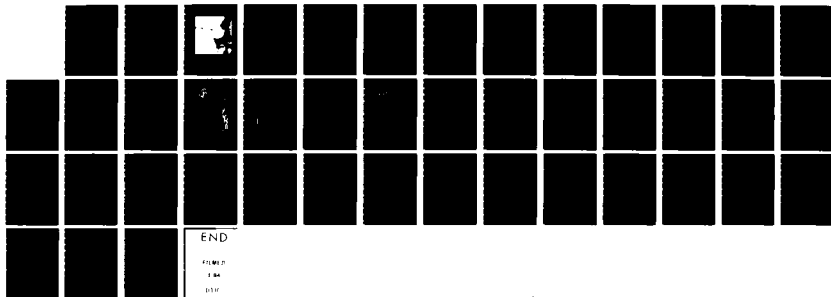
SWIRLS AND PLUMES OR APPLICATION OF STATISTICAL METHODS 3/3
TO SATELLITE-DERIVED (U) SCRIPPS INSTITUTION OF
OCEANOGRAPHY LA JOLLA CA K A KELLY AUG 83

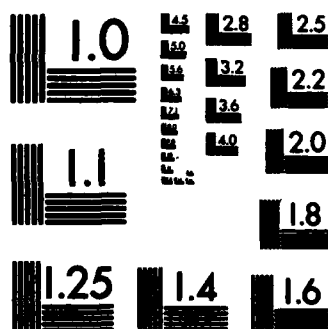
UNCLASSIFIED

SIO-REF-83-15 N00014-80-C-0440

F/G 8/10

NL





MICROCOPY RESOLUTION TEST CHART
NATIONAL BUREAU OF STANDARDS-1963-A

to isotherms assumes a geostrophic balance, where temperature is proportional to density; one would expect this model to break down near a boundary. A combination of satellite data and in situ measurements would undoubtedly improve the estimates: the velocity measurements could calibrate the satellite estimates and the maps could interpolate between velocity measurements. Because the velocity maps have the right features, although the magnitudes may be too low, they could be used to test models of the surface velocity field, such as the assumption of horizontal non-divergence or upwelling along a front.

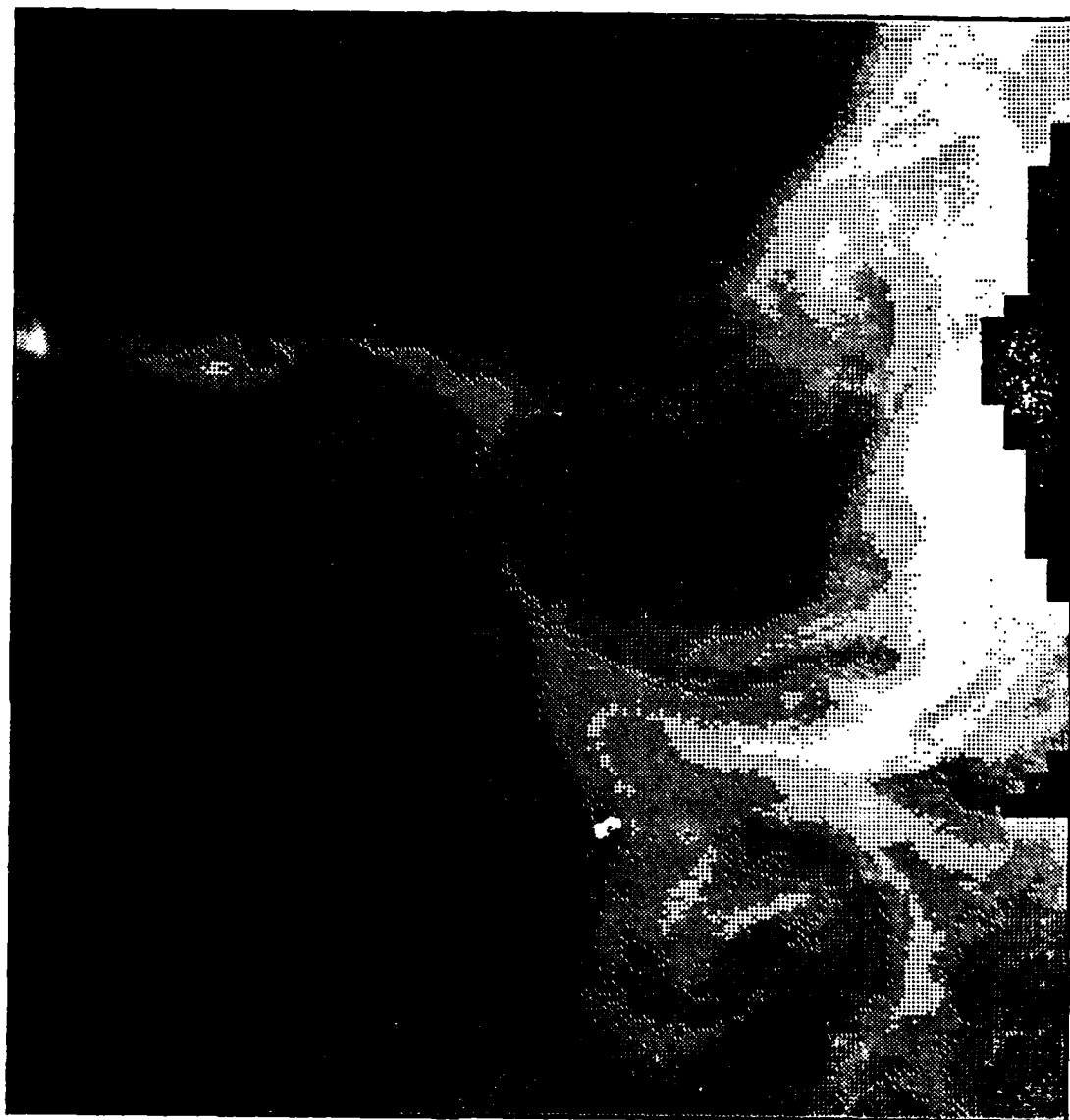


FIG. 8.1 IMAGE USED FOR VELOCITY ESTIMATE

The SST map for day 189 from which the gradient of temperature was computed. The difference between this map and a map for 12 hours later was used to approximate the derivative of temperature with respect to time.

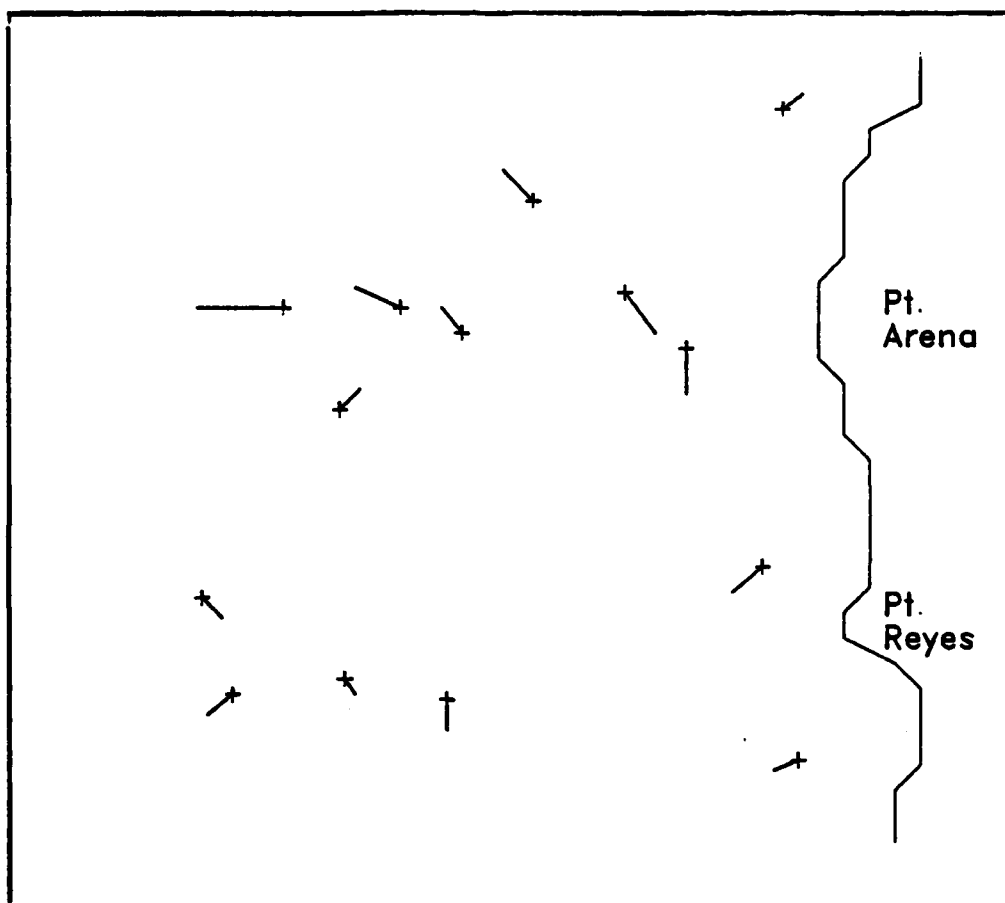


FIG. 8.2 DISPLACEMENT OF SMALL FEATURES

Several small features could be followed from the first image to the second image. The "+" marks the location of a feature in the first image and is the tail of the displacement vector.

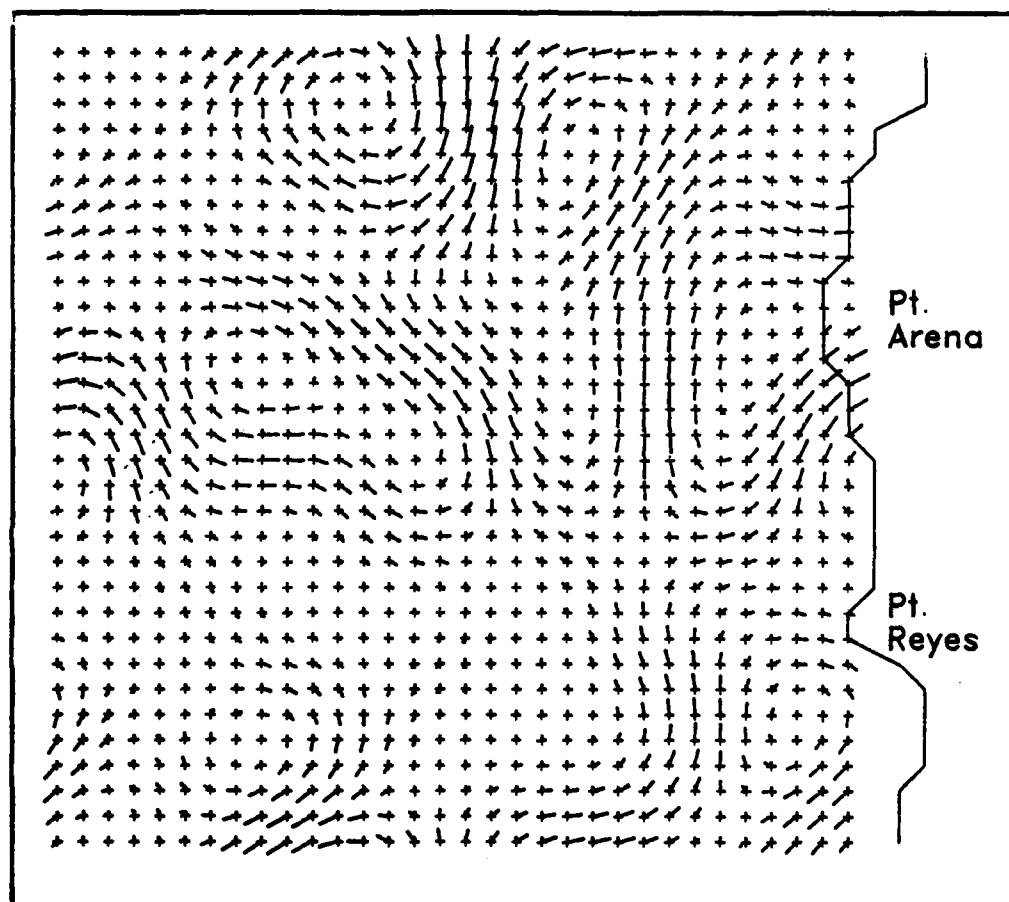


FIG. 8.3 CROSS-ISOTHERM VELOCITY

From the conservation of temperature equation, cross-isotherm velocities were computed. The "+" marks the location of the computed velocity and the tail of the velocity vector. Maximum velocities were about 5 cm/s. The weights for the equations, as described in the text, were $w_1=1$ and $w_3=1$.

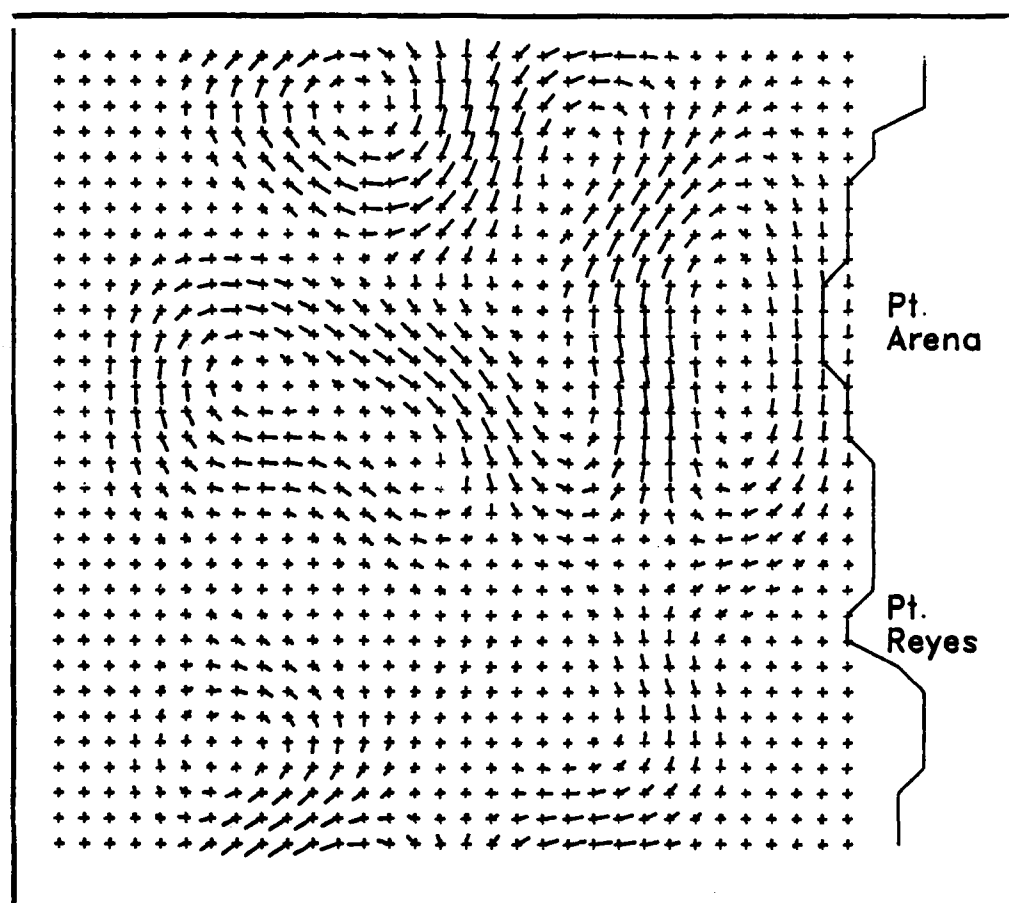


FIG. 8.4 EFFECT OF STRONGER BOUNDARY CONDITION

Same as Figure 8.3, except with larger weight for the boundary condition ($w_3=100$). Note that the velocities at the coastline are either zero or parallel to the edge.

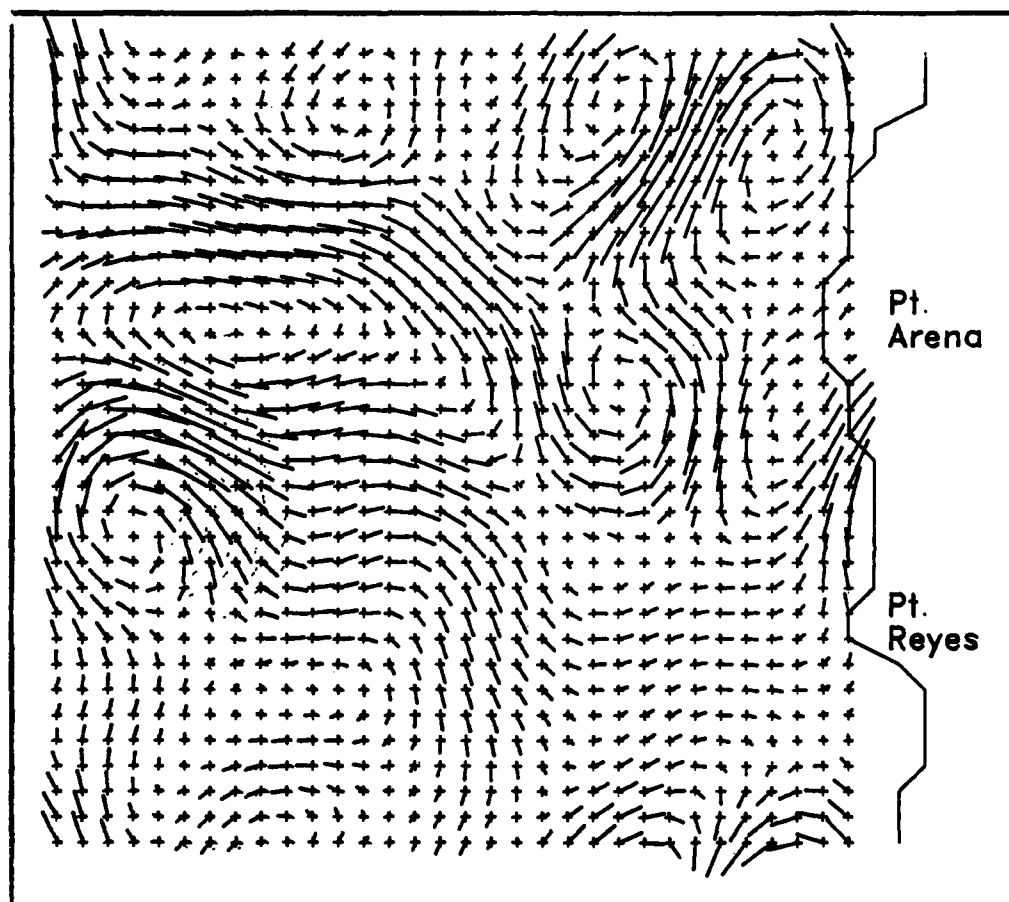


FIG. 8.5 TOTAL VELOCITY FIELD

Velocity estimate which includes components both parallel and perpendicular to the isotherms. The three equations used to compute the estimate were equally-weighted: $w_1=1$, $w_2=1$, $w_3=1$, as described in the text. Maximum velocities were about 40 cm/s. Agreement with doppler-log velocities was good except near the coast.

REFERENCES

- Allen, J. S., 1980. Models of wind-driven currents on the continental shelf, Ann. Rev. Fluid Mech., 12, 389-433.
- Allen, J. S. and G. R. Halliwell, Jr., 1983. Large-scale wind and sea-level observations. In CODE-1 Moored Data Report, edited by L. K. Rosenfeld, WHOI Tech. Rept., (in press).
- Arthur, R. S., 1965. On the calculation of vertical motion in eastern boundary currents from determinations of horizontal motion, J. Geophys. Res., 70, 2799-2802.
- Bakun, A., 1975. Daily and weekly upwelling indices, west coast of North America, 1967-73, NOAA Tech. Rept. NMFS SSRF-693.
- Bernstein, R. L., Larry Breaker and Robert Whritner, 1977. California Current eddy formation: ship, air and satellite results, Science, 195(4276), 353-359.
- Bernstein, R. L., 1982. Sea surface temperature estimation using NOAA 6 satellite advanced very high resolution radiometer, J. Geophys. Res., 87, 9455-9465.
- Breaker, L. C., 1981. The application of satellite remote sensing to west-coast fisheries, Mar. Tech. S. J., 15, 32-40.
- Bretherton, F. P., R. E. Davis and C. B. Fandry, 1976. A technique for objective analysis and design of oceanographic experiments applied to MODE-73, Deep Sea Res., 23, 559-582.
- Brown, W. S., J. D. Irish and A. D. Bratkovich, 1983. Moored temperature and conductivity observations. In CODE-1 Moored Data Report, edited by L. K. Rosenfeld, WHOI Tech. Rept., (in press).

- Chahine, M. T., 1981. Remote sensing of sea surface temperature in the $3.7 \mu\text{m CO}_2$ band, Oceanography from Space, edited by J. F. R. Gower, Plenum, New York, 87-95.
- Chelton, D. B., Jr., 1980. Low frequency sea level variability along the west coast of North America, Ph. D. thesis, Scripps Inst. of Oceanogr., La Jolla, Ca.
- Coakley, J. A. and F. P. Bretherton, 1982. Cloud cover from high-resolution scanner data: detecting and allowing for partially filled fields of view, J. Geophys. Res., 87, 4917-4932.
- Davis, R. E., 1976. Predictability of sea surface temperature and sea level pressure anomalies of the North Pacific, J. Phys. Oceanogr., 6, 249-266.
- Davis, R. E., 1977. Techniques for statistical analysis and prediction of geophysical fluid systems, Geophys. Astrophys. Fluid Dynamics, 8, 245-277.
- Davis, R. E., 1983. Current-Following Drifters in CODE, CODE Tech. Rept. No. 10, Scripps Inst. of Oceanogr., Ref. 83-4, La Jolla, Ca.
- Deschamps, P. Y. and T. Phulpin, 1980. Atmospheric correction of infrared measurements of sea surface temperature using channels 3.7, 11, and 12 μm , Boundary Layer Meteorol., 18, 131-143.
- Fleischbein, J., Gilbert, W. E., and Huyer, A., 1982. Hydrographic data from the first Coastal Ocean Dynamics Experiment: leg 4, 25 April-7 May 1981, Oregon State Univ., Ref. 82-2, Corvallis, Or.
- Franklin, J. N., 1968. Matrix Theory, Prentice-Hall, 292 pp..
- Friehe, C. A. and C. D. Winant, 1982. Observations of wind and sea surface temperature structure of the northern California coast, First International Conference of Meteorology and Air-Sea Interaction of

- the Coastal Zone, 10-14 May 1982, The Hague, Netherlands.
- Head, M. R., 1982. Flow Visualization II, edited by W. Merzkirch, Washington: Hemisphere, as seen in An Album of Fluid Motion, edited by M. Van Dyke, The Parabolic Press, Stanford, California, 399-403.
- Hendershott, M. C. and P. Rizzoli, 1976. The winter circulation of the Adriatic Sea, Deep-Sea Res., 23, 353-370.
- Hickey, B. M., 1979. The California Current System - hypotheses and facts, Progress in Oceanography, 8(4).
- Hua, B. L., 1981. Modélisation numérique d'upwellings côtiers à l'aide d'une méthode d'éléments finis. Application au golfe du Lion. Thèse doctorat d'état es Sciences Physiques, Université Pierre et Marie Curie et Muséum National Histoire Naturelle, Paris, 214 pp.
- Huyer, A., E. J. C. Sobey and R. L. Smith, 1979. The spring transition in currents over the Oregon continental shelf, J. Geophys. Res., 84, 6995-7011.
- Katsaros, K., 1980. Radiative sensing of sea surface temperature, in Air-sea Interaction: Instruments and Methods, edited by F. Dobson, L. Hasse, and R. Davis, 801 pp., Plenum, New York.
- Kelly, K. A., 1982. Infrared satellite data from the first Coastal Ocean Dynamics Experiment: March-July 1981, Scripps Inst. of Oceanogr., Ref. 82-15, La Jolla, Ca.
- Lawson, C. L. and R. J. Hanson, 1974. Solving Least Squares Problems, Prentice-Hall, 340 pp.
- Large, W. G. and S. Pond, 1981. Open ocean momentum flux measurements in moderate and strong winds, J. Phys. Oceanogr., 11, p. 324.
- Leggeekis, R. V., 1975. Application of synchronous meteorological satellite data to the study of time dependent sea surface temperature

- changes along the Gulf Stream, Geophys. Res. Letters, 2,(10), 435-438.
- Legeckis, R. V. and J. Pritchard, 1976. Algorithm for correcting the VHR imagery for geometric distortions due to earth curvature, earth rotation, and spacecraft roll attitude, NOAA Technical Memorandum NESS 77.
- Legeckis, R. V., 1979. Satellite observations of the influence of bottom topography on the seaward deflection of the Gulf Stream off Charleston, South Carolina, J. Phys. Oceanogr., 9, 483-497.
- McClain, E. P., 1981. Multiple atmospheric-window techniques for satellite sea surface temperatures, in Oceanography From Space, edited by J. F. R. Gower, Plenum, New York, 73-85.
- Mills, C. A. and R. C. Deardsley, 1983. Coastal and moored meteorological observations. In CODE-1 Moored Data Report, edited by L. K. Rosenfeld, WHOI Tech. Rept., (in press).
- Olivera, M., W. E. Gilbert, J. Fleischbein, A. Huyer, and R. Schramm, 1982. Hydrographic Data from the First Coastal Ocean Dynamics Experiment: R/V Wecoma, Leg 7, 1-14 July 1981, Oregon State Univ., Ref. 82-8, Corvallis, Or.
- Olivera, R. M., 1982. A complex distribution of water masses and related circulation off northern California in July 1981, Master's thesis, Oregon State Univ., Corvallis, Or.
- Oppenheim, A. V. and J. S. Lim, 1981. The importance of phase in signals, Proceedings of the IEEE, 69(5), 529-541.
- Pedlosky, J., 1979. Geophysical Fluid Dynamics, Springer-Verlag, p. 54.
- Peffley, M. B. and J. J. O'Brien, 1976. A three-dimensional simulation of coastal upwelling off Oregon, J. Phys. Oceanogr., 6, 164-180.

- Parker, R. L. and S. P. Huestis, 1974. The inversion of magnetic anomalies in the presence of topography, *J. Geophys. Res.*, 79(11), 1587-1593.
- Parker, R. L., 1983. Unpublished manuscript.
- Parlett, B. N., 1980. The Symmetric Eigenvalue Problem, Prentice-Hall, 349 pp.
- Provost, C., 1983. A variational method for estimating the general circulation in the ocean, Ph.D. thesis, Scripps Inst. of Oceanogr., La Jolla, Ca.
- Schwalb, A., 1978. The TIROS-N/NOAA A-G satellite series, Tech. Memo., NESS 95, 75 pp., Natl. Oceanic and Atmos. Admin., Boulder, Co.
- Stewart, R. H., 1983. Methods of Satellite Oceanography, unpublished manuscript.
- Van Woert, M., 1982. The Subtropical Front: Satellite Observations During FRONTS 80, *J. Geophys. Res.*, 87, 9523-9536.
- Winant, C. D., 1980. Coastal circulation and wind-induced currents, Ann. Rev. Fluid Mech., 12, 271-301.
- Winant, C. D. and A. W. Bratkovich, 1983. CODE-1 moored current observations. In CODE-1 Moored Data Report, edited by L. K. Rosenfeld, WHOI Tech. Rept., (in press).
- Wyllie, J. G., 1966. Geostrophic flow of the California Current at the surface and at 200 meters, California Cooperative Oceanic Fisheries Investigations Atlas No. 4, 288 pp.
- Young, T. L. and J. H. Fahle, 1981. User's manual for preliminary satellite image processing: extraction, calibration, and location, Scripps Inst. of Oceanogr., Ref. 81-36, La Jolla, Ca.

APPENDIX A

EXAMPLE OF CLOUD FLAGGING PROCEDURE

The flagging of cloud-contaminated data was a tedious, but necessary empirical procedure. Two fundamental concepts were used to recognize clouds:

- i) subtracting channel 4 from channel 3 removes most of the sea surface signal and therefore enhances clouds relative to SST (see Appendix B)
- ii) clouds have higher local variability than SST's

These concepts were used to design two algorithms which created a mask for each image. A flow chart for the procedure is shown in Figure 3.4. The purpose of this appendix is to clarify the procedure by showing the input and output of each algorithm and the operator decisions which were made for a sample image.

The entire procedure could be automated to eliminate the operator decisions; however, a more sophisticated pattern-recognition scheme would be needed to maintain data quality. The point at which I stopped automating the procedure was when it became more difficult to teach the computer how to make a decision than to make it myself. Some of the input parameters were constant for the entire series of images and some varied from image to image. The input parameters required by each algorithm are shown in Table A.1 along with a designation of fixed or variable. All parameters could be fixed to eliminate operator intervention; however, any fixed value for a threshold, for example, would result in either too few or too many data being designated clouds. A clever pattern-recognition scheme could probably select the proper threshold

for each image.

The first algorithm required the difference of channels 3 and 4, so the channel 4 image was first subtracted from the channel 3 image. The land mask was also required for the first algorithm. This mask was created from these same algorithms with a series of clear images. Land has some of the same characteristics as clouds; however, it does not move from image to image. For each 5 x 5 non-overlapping subset of this difference image, two quantities were computed:

- 1) the mean value for the 25 pixels, MEAN
- 2) the maximum difference between adjacent pixels (along a row only), MAXDIF

Those subsets whose MAXDIF did not exceed NDIFF1 and whose means were within the interval (MIN,MAX) were sorted into seven bins. The subsets were each assigned an integer code according to the following system:

- 0, MAXDIF > NDIFF2 or MEAN is not in (MIN,MAX)
- 9, NDIFF1 < MAXDIF < NDIFF2
- 2-8, $\max(\text{MIN}, \text{smallest MEAN}) < \text{MEAN} < \min(\text{MAX}, \text{largest MEAN})$

where the limits for the codes 2-8 were the maximum of the variable MIN and the smallest subset mean, and the minimum of the variable MAX and the largest subset mean. The parameters MAX and MIN assured that the coding interval of the means was within reasonable limits, i.e., $\pm 3^{\circ}$ C. The coded output of algorithm 1 is shown in Figure A.1. The 0's on the right-hand side of the image are primarily from the land mask which contains 0's for land and 1's for ocean subsets. These subsets were not examined by the algorithm. The range of mean values for this image was (-258,1680); the actual interval used for codes 2-8 was (-258,300).

Mean values from about 220 to 300 ($2.20 - 3.00^{\circ}$ C.) correspond to code 8, from 140 to 220 correspond to code 7, etc. By comparing the coded output in Figure A.1 with the image in Figure 3.2, I decided that codes 2,3,7,8 and 9 were clouds and changed the codes to 0's, and that codes 4,5 and 6 were ocean and changed them to 1's. The result of this sorting decision is shown as Figure A.2, the rough mask from algorithm 1. This mask was needed for algorithm 2 and for the next step.

Algorithm 2 required a minimum temperature threshold and a maximum temperature threshold for channel 4. These values were obtained by computing the mean values of those subsets in the channel 4 image which corresponded to 1's in Figure A.2. These images were registered with the coastline nearly vertical so that left-to-right in the image corresponded to the onshore direction. The sea surface was nearly always coldest near the coast so that a useful minimum threshold was defined as a function of its distance from the coast. Therefore the means were plotted against the subset distance from the left side of the image as shown in Figure A.3. The dense locus of mean values generally had a parabolic shape so a parabola was used to define the bottom boundary of the cluster. Values at distances 0, 40 and 80 were selected by eye to define the parabola and were input parameters for algorithm 2. The values used for this image are shown in Table A.1.

In algorithm 2 each subset in the channel 4 image which corresponded to a 1 (ocean) in the rough mask was examined and assigned an integer code according to the following system:

- 1, ocean (met none of the following tests)
- 2, at least two pixels were less than subset mean by NDIFF

- 3, at least two pixels exceeded subset mean by NDIFF
- 4, at least NJUMP positive and NJUMP negative jumps occurred in the subset
- 5, subset average was outside (MIN,MAX)
- 6, combination of 2 and 4
- 7, combination of 3 and 4
- 8, at least one positive and one negative jump of size NDIFF occurred on each of NJUMP lines
- 9, combination of 2 and 8

The coded mask containing integers 0-9 was edited automatically by the second part of algorithm 2. Essentially all subsets with the highest rank, 9, were classified as clouds. The other subsets were classified according to how many nearby subsets were already classified as clouds (0) or had high ranks (7,8,9). For example, a subset with a rank of 2 or 3, surrounded by 1's, would be reclassified as ocean (1). A subset with rank 7 surrounded by 0's and 9's would be classified as cloud. This process is arbitrary and certain cases were left undetermined to be decided by the operator. The output from algorithm 2 is shown in Figure A.4. The subsets marked 9 are those which were classified clouds by the editing procedure. Subsets marked 2-8 are those which the editing procedure could not classify. In this example 421 additional subsets were classified as clouds, 134 were indeterminate, and 37 were ranked higher than 1 and were reclassified as ocean. Based on a comparison with the image, I changed all the indeterminate subsets to 0 (cloud). The final mask is shown as applied to the image in Figure 3.5. The white areas have been masked with a large negative number. The remaining areas are the original channel 4 image.



FIG. A.2 ROUGH MASK FROM ALGORITHM 1

The clear ocean codes (4, 5 and 6) in Figure A.1 were changed to 1's. All other codes, which were not already 0, were changed to 0. Only subsets corresponding to 1's were examined by Algorithm 2.

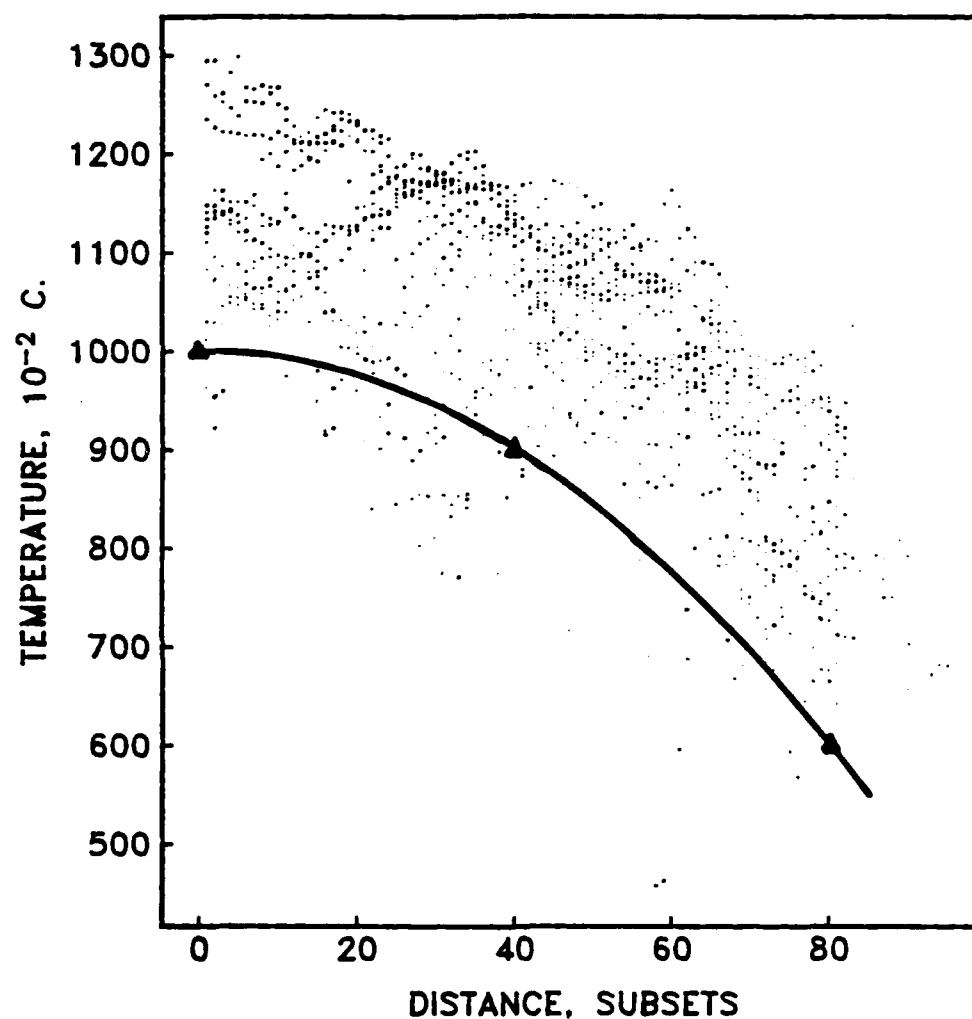


FIG. A.3 MEAN CHANNEL 4 TEMPERATURES

Subset mean temperature as a function of distance from the left side of the mask. The temperatures for the three triangles, which define a parabola just below the cluster of mean values, were input variables for Algorithm 2.



FIG. A.4 EDITED MASK FROM ALGORITHM 2

The code 9 indicates subsets which were classified as clouds by Algorithm 2. Codes 2-8 are subsets which could not be classified automatically; their validity must be determined by the operator. The codes are described in the text.

Table A.1 Input Variables for Cloud Detection Algorithms

algorithm	name	varying or fixed	value	description
1	NDIFF1	F	150	jump between adjacent pixels
	NDIFF2	F	250	jump between adjacent pixels
	MAX	F	-300	minimum value for means
	MIN	F	300	maximum value for means
2	MAX	V	1300	maximum threshold for means
	M0	V	1000	minimum value at 0
	M1	V	900	minimum value at 40
	M2	V	600	minimum value at 80
	NDIFF	F	80	jump between adjacent pixels
	NJUMP	F	2	number of jumps

Variable names and definitions for the two cloud-detection algorithms. Those variables designated fixed (F) retained the same value for all the images; those which varied (V) had different values for each image. The values listed are those used in the example described in the text and in the figures. All values and data were in hundredths of a degree C. because the data were stored as integers.

APPENDIX B

REMOVING NOISE FROM CHANNEL 3

The noise is removed from the channel 3 image using a Gaussian filter in the Fourier domain. To retain the small scale ocean features in the data while removing noise which has comparable length scales, the noise is enhanced relative to the sea-surface signal. This is done by subtracting the channel 4 image from the channel 3 image.

To understand why this technique decreases the signal-to-noise ratio let us look at the radiative transfer equation from Chapter 4 :

$$I_{\lambda} = B_{\lambda}(T_0) t_{\lambda}(0, p_0) - \int_0^{p_0} B_{\lambda}(T(p)) dt_{\lambda}(0, p) \quad (B.1)$$

where I_{λ} is the radiance measured at the satellite, T_0 is the temperature at p_0 , $t_{\lambda}(0, p)$ is the optical depth of the atmosphere between pressure levels 0 and p , and B_{λ} is the Planck function which defines the relationship between any radiance value and the temperature of a blackbody that would give the same radiance

$$B_{\lambda}(T) = I_{\lambda}.$$

The temperatures used in equation B.1 are for a blackbody. To convert to actual sea-surface temperatures (SST's), one needs to know the emissivity, ϵ , which is a function of the radiation wavelength, λ , and the composition of the radiator. The emissivity is defined as

$$\epsilon_{\lambda} = \frac{I_{\lambda} \text{ observed}}{B_{\lambda}(T)}$$

When the observed radiance is simply converted to a temperature using the inverse of the Planck function, that temperature is called the brightness temperature; it is not the temperature of the actual radiator because the emissivity is less than one for non-blackbodies.

The channel 3 image consists of the actual channel 3 brightness temperatures plus some noise

$$T_3' = T_3 + \text{noise}$$

The quantity $\frac{\partial T_3}{\partial x}$ is used as a measure of the sea-surface signal because the temperature patterns are recognizable, as is the noise, by their spatial fluctuations. Then the ratio of the signal in the difference of channels 3 and 4 to the signal in the channel 3 image is

$$\frac{\frac{\partial}{\partial x}(T_3 - T_4)}{\frac{\partial}{\partial x} T_3}$$

where T_j is the brightness temperature

$$T_j = B_j^{-1}(I_j), \quad j = 3, 4.$$

Taking the spatial derivative of the brightness temperature gives, in terms of the Planck function,

$$\begin{aligned} \frac{\partial}{\partial x} T_j &= \frac{\partial B_i^{-1}(I_j)}{\partial I_j} \frac{\partial I_j}{\partial x} \\ &= \left[\frac{\partial B_i(T)}{\partial T} \right]^{-1} \frac{\partial I_j}{\partial x} \end{aligned} \quad (B.2)$$

and substituting it into the spatial derivative of B.1 gives

$$\frac{\partial I_j}{\partial x} = \frac{\partial}{\partial x} [B_j(T_0) t_j] - \frac{\partial}{\partial x} \left[\int_0^{p_0} B_j(T) dt_j \right] \quad (B.3)$$

Assuming that the atmospheric spatial scales are much larger than the sea-surface temperature scales in areas which are apparently cloudless, the second term is much smaller than the first and

$$\frac{\partial I_j}{\partial x} \approx t_j \frac{\partial B_i(T)}{\partial T} \frac{\partial T_i}{\partial x} \quad (B.4)$$

Substituting B.4 into B.2 gives

$$\frac{\partial T_i}{\partial x} = \left[\frac{\partial B_i(T)}{\partial T} \right]^{-1} t_j \frac{\partial B_i(T)}{\partial T} \frac{\partial T_i}{\partial x} \quad (B.5)$$

$$= t_j \frac{\partial T_i}{\partial x} \quad j = 3, 4.$$

The spatial derivative for the actual sea-surface temperature, T_s , includes the emissivity of sea water

$$\begin{aligned}
\frac{\partial T_s}{\partial x} &= \frac{\partial}{\partial x} [B_j^{-1} (\epsilon_j^{-1} I_j)] \\
&= \epsilon_j^{-1} \left[\frac{\partial B_j}{\partial T} \right]^{-1} \frac{\partial I_j}{\partial x} \\
&= \epsilon_j^{-1} \frac{\partial T_j}{\partial x}.
\end{aligned}
\tag{B.6}$$

Substituting B.6 into B.5 gives

$$\frac{\partial T_i}{\partial x} = t_j \epsilon_j \frac{\partial T_s}{\partial x}
\tag{B.7}$$

and using B.7 to determine the change in the temperature signal gives for the ratio of the signals

$$\frac{\frac{\partial}{\partial x} (T_3 - T_4)}{\frac{\partial}{\partial x} T_3} = 1 - \frac{t_4 \epsilon_4}{t_3 \epsilon_3}
\tag{B.8}$$

Assuming the optical depth for the two channels is approximately the same, i.e., $t_3 \approx t_4$, and using for ϵ_3 and ϵ_4 values of 0.975 and 0.993 respectively, which were found by Katsaros (1980), the ratio in B.8 is

$$\frac{\text{signal in difference}}{\text{signal in channel 3}} \approx 2 \%$$

Thus the signal is reduced to 2 % of its original value while noise in channel 3 is unchanged by the subtraction of the noise-free channel 4.

For an area of the image which contains scattered clouds or the edges of clouds, the second term in B.3 becomes important. This term will be large so it is not possible to remove the noise in channel 3 from cloudy areas. However, if the noise is not too large, then this term will be the dominant term and the difference image becomes an effective cloud detector.

The method used to remove noise in channel 3 is shown schematically in Figure B.1. For simplicity the process is shown in one dimension only, using the values along a vertical line of the image shown in Figure 3.1. In order to prevent the large signal from clouds from contributing to the Fourier magnitudes, the difference image is clipped before it is transformed, so that only values in cloud-free areas are filtered for noise. Maximum and minimum values for clipping are obtained by examining the image on a digital display and selecting the maximum and minimum values corresponding to the clear ocean area. The maximum value for the image shown is 2.0° C. and the minimum value is -1.5° C. The clipping is illustrated in Figure B.1: all values greater than 2.0° C. are set to 2.0 and similarly for values less than -1.5. The mean of the clipped image is computed and subtracted and the image is padded with zeroes to an even power of two. The clipped and demeaned difference image is digitally Fourier transformed in two dimensions.

To isolate the noise pattern, the difference image is high-passed using a two-dimensional Gaussian filter, i.e.,

$$F(k, l) = F(k, l) [1 - \exp(-\beta(k^2 + l^2))] \quad (B.9)$$

where $\beta = 0.01$. This corresponds to a half-power wavelength of 87 pixels. The high-passed version is then inverse Fourier transformed to produce an image which is the noise to be removed from channel 3. The areas which were clipped have values of zero in the noise image and the noise has a zero mean. No noise is removed from cloud and land portions of the image, but this is not a problem because cloud and land are screened in the cloud-detection procedure. The noise is subtracted from the channel 3 image. A comparison of a section of the channel 3 image before and after the noise removal is shown in Figure 4.1.

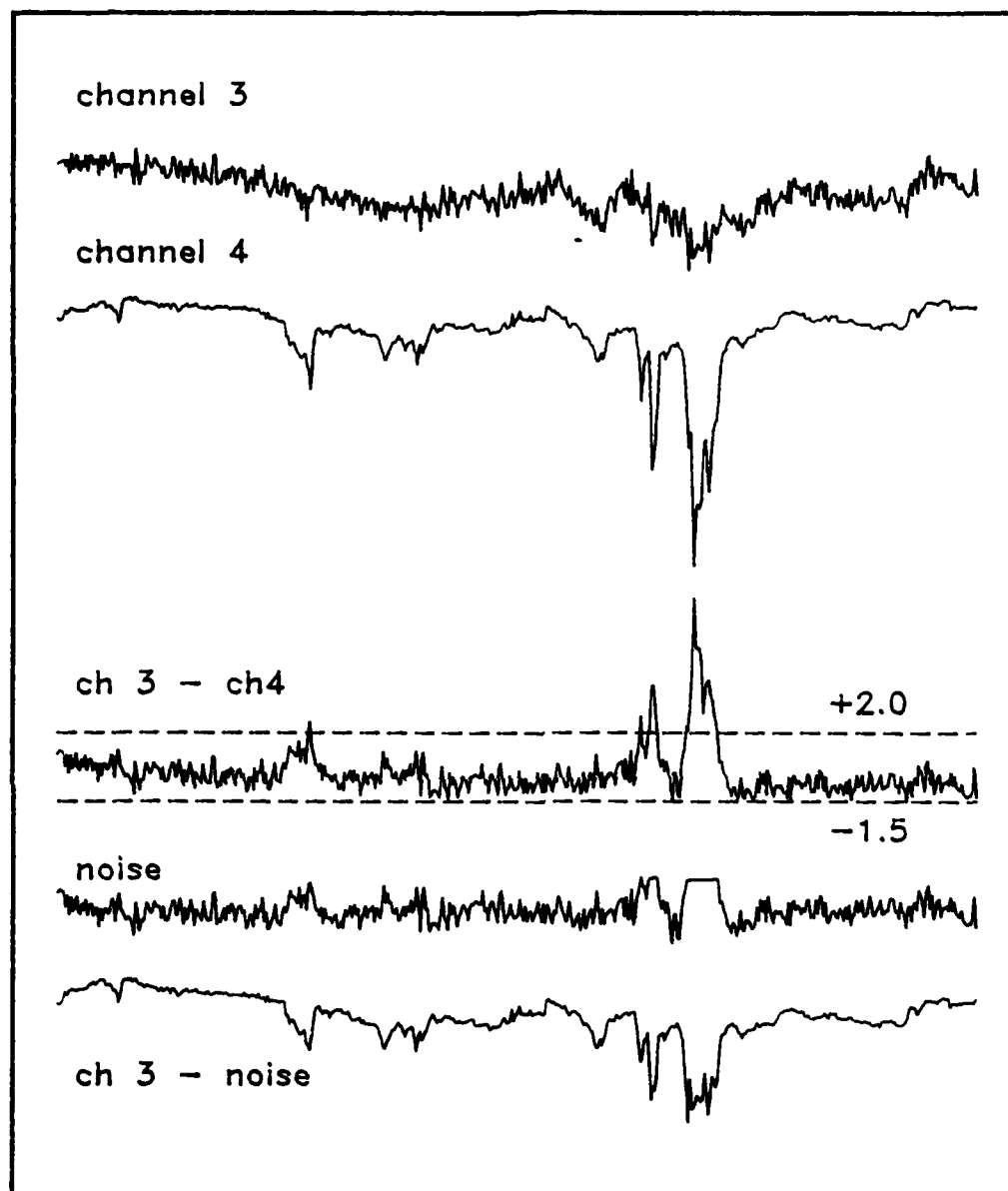


FIG. B.1 CHANNEL 3 NOISE REMOVAL

One dimensional illustration of the noise removal technique discussed in the text. The difference of the channels is clipped to reduce contributions from clouds before it is high-passed to isolate the noise signal.

APPENDIX C

LEAST SQUARES ESTIMATION

This appendix contains a review of the basic equations for computing a linear estimator using a least-squares measure of fit. It is essentially a rewriting of Davis (1977) using vector notation. The following notation is used here:

\underline{x} , a vector

X , a matrix

$\tilde{\underline{x}}$, the estimate of a (vector) quantity

Before computing the linear estimator the means of all variables have been subtracted so that their expected value is zero, i.e.,

$$\langle x(t) \rangle = 0$$

where the expected value is defined as

$$\langle x(t) \rangle = \frac{1}{N} \sum_{i=1}^N x(t_i).$$

The means are removed in order to suppress the artificially-high correlations that result from variables with large mean values. Removing the means does not ultimately change the coefficients in the estimator, but it does aid in evaluating the contribution of each variable to estimation skill.

Let $x_m(t_n)$ be the value of the m th variable sampled at time t_n and let X be the matrix of all M variables at all N sample times, t_n ,

$$X = \begin{bmatrix} x_1(t_1) & \dots & x_M(t_1) \\ x_1(t_2) & & x_M(t_2) \\ \vdots & & \vdots \\ x_1(t_N) & \dots & x_M(t_N) \end{bmatrix}$$

where X is an $N \times M$ matrix. Let \underline{z} be a quantity which is to be estimated as a linear combination of the variables, x_m . The sample variance of \underline{z} is defined as

$$\frac{1}{N} \underline{z}^T \underline{z}$$

where \underline{z} is the N vector of $p(t_n)$ values and \underline{z}^T is the transpose of \underline{z} . Let $\tilde{\underline{z}}$ be an estimate of \underline{z} which is a linear combination of the data such that

$$\tilde{\underline{z}} = X \underline{a} \quad (C.1)$$

This equation can be written out in components as

$$\begin{bmatrix} \tilde{z}_1 \\ \tilde{z}_2 \\ \vdots \\ \tilde{z}_N \end{bmatrix} = \begin{bmatrix} x_1(t_1) & \dots & x_M(t_1) \\ x_1(t_2) & & x_M(t_2) \\ \vdots & & \vdots \\ x_1(t_N) & \dots & x_M(t_N) \end{bmatrix} \begin{bmatrix} a_1 \\ a_2 \\ \vdots \\ a_M \end{bmatrix}$$

The vector \underline{a} contains the constant coefficients for each of the M variables used in the estimate.

For $\tilde{\mathbf{z}}$ to be a good estimate in the least-squares sense, the length of the error vector

$$\mathbf{e} = \mathbf{z} - \tilde{\mathbf{z}} \quad (\text{C.2})$$

must be a minimum, or equivalently, \mathbf{e} must have no projection on the plane of the data variables, i.e.,

$$\langle \mathbf{x}_m(t) \mathbf{e}(t) \rangle = 0 \quad m = 1, M$$

or

$$\mathbf{X}^T \mathbf{e} = \mathbf{0} \quad (\text{C.3})$$

Substituting C.1 and C.2 into C.3 gives

$$\mathbf{X}^T (\mathbf{z} - \mathbf{X} \mathbf{a}) = \mathbf{0} \quad (\text{C.4})$$

and solving for \mathbf{a} gives

$$\mathbf{a} = \mathbf{C}^{-1} \mathbf{X}^T \mathbf{z} \quad (\text{C.4}')$$

where

$$\mathbf{C} = \mathbf{X}^T \mathbf{X}.$$

The error, \underline{e}_0 , for this value of \underline{g} has the minimum length, or the minimum 2-norm error, where the 2-norm is defined as

$$||\underline{e}||_2 = \left[\frac{1}{N} \underline{e}^T \underline{e} \right]^{1/2} \quad (\text{C.5})$$

The squared error for the estimate $\tilde{\underline{z}}$ is

$$\frac{1}{N} \underline{e}_0^T \underline{e}_0 = \frac{1}{N} \left[\underline{z}^T \underline{z} - \underline{z}^T \underline{X} \underline{C}^{-1} \underline{X}^T \underline{z} \right] \quad (\text{C.6})$$

Substituting C.4' into C.6 gives

$$\frac{1}{N} \underline{e}_0^T \underline{e}_0 = \frac{1}{N} \left[\underline{z}^T \underline{z} - \underline{z}^T \underline{X} \underline{C}^{-1} \underline{X}^T \underline{z} \right] \quad (\text{C.6}')$$

The skill for an estimate is defined as

$$S = \frac{\text{variance estimated}}{\text{total variance}}$$

In this case the variance estimated is computed as the total variance minus the squared error. For the estimate, $\tilde{\underline{z}}$, the skill is given by

$$S = \frac{\underline{z}^T \underline{z} - \underline{e}_0^T \underline{e}_0}{\underline{z}^T \underline{z}} \quad (\text{C.7})$$

or substituting C.6' into C.7

$$S = \frac{\mathbf{z}^T \mathbf{X} \mathbf{C}^{-1} \mathbf{X}^T \mathbf{z}}{\mathbf{z}^T \mathbf{z}}$$

In practice \mathbf{g} was not found by inverting the matrix \mathbf{C} , but rather by solving the overdetermined system

$$\mathbf{z} = \mathbf{X}\mathbf{g}$$

using QR, a matrix factorization algorithm (Lawson and Hanson, 1974). The QR algorithm factors \mathbf{X} and finds \mathbf{g} such that $\mathbf{z} = \mathbf{X}\mathbf{g} + \mathbf{r}$ and returns the squared error, $\mathbf{r}^T \mathbf{r}$, as a measure of the misfit. The advantage of QR over matrix inversion is that it is numerically stable, especially for large systems of equations.

In general the skill obtained in fitting a given set of data is less than that which one would obtain in applying the same coefficients \mathbf{g} to a new set of data. The extra skill, called artificial skill, comes from the finite size of the original data set and from an inevitable reduction in variance from adding more variables. The artificial skill, S_A , for a variable not well correlated with the quantity to be estimated is

$$S_A = \frac{M}{N^*}$$

where M is the number of variables and N^* is the equivalent number of degrees of freedom of each variable (and where all variables are assumed to have the same value for N^*). Thus to obtain the best possible

estimator to predict \underline{z} , it is necessary to limit the number of variables, M , (or equivalently, to increase the number of independent samples, N^*). This is best done by choosing the most likely variables for the estimator a priori. If this is not practical, a less effective way of preventing artificial skill is to screen the variables by selecting those which contribute most to the skill. If an additional variable contributes only $\approx \frac{1}{N^*}$ to the skill, then the increase in skill is probably artificial and using this variable in the estimator will degrade the prediction.

APPENDIX D

INTERPOLATION OF IMAGES

This appendix describes the method used to interpolate images in both space and time as discussed in Chapter 7. The interpolation scheme is a variant of objective mapping as described in Bretherton, Davis and Fandry (1976) and the discussion here follows that paper, using matrix notation.

Starting with an image which has some data missing due to clouds, data which are nearby in space and in time are used to interpolate into the holes. Each missing datum is filled with the linear combination of the nearby data and which is the best estimate in the least-squares sense.

Let $T(x,t)$ be the value to be estimated and let

$$T = \begin{bmatrix} T(t_1) \\ T(t_2) \\ \vdots \\ \vdots \\ \vdots \end{bmatrix}$$

be the hypothetical ensemble of N estimates for T . Let J be a vector of 1's

$$J = \begin{bmatrix} 1 \\ 1 \\ \vdots \\ \vdots \\ \vdots \end{bmatrix}$$

so that an ensemble mean can be defined as

$$\langle T \rangle = \frac{1}{N} J^T J \quad (D.1)$$

Let \mathbf{b} be the matrix of nearby data for the ensemble

$$\mathbf{b} = \begin{bmatrix} \phi_1(t_1) & \phi_1(t_2) & \cdot & \cdot & \cdot \\ \phi_2(t_1) & \phi_2(t_2) & \cdot & \cdot & \cdot \\ \vdots & \vdots & & & \\ \phi_N(t_1) & \phi_N(t_2) & \cdot & \cdot & \cdot \end{bmatrix}$$

where each function $\phi_i(t_j)$ represents a nearby location in time and space and the value of ϕ_i is the datum at that location at time t_j .

Then a linear estimate for T is defined as

$$T = \mathbf{b}^T \mathbf{a} \quad (D.2)$$

subject to the constraint

$$J^T \mathbf{a} = 1 \quad (D.3)$$

where \mathbf{a} is the vector of coefficients. To find the vector \mathbf{a} which corresponds to the minimum squared error define

$$U = \frac{1}{N} (T - \mathbf{b}^T \mathbf{a})^T (T - \mathbf{b}^T \mathbf{a}) + \lambda (J^T \mathbf{a} - 1) \quad (D.4)$$

where the first term is the mean square error and λ is a Lagrange multiplier and vary U with respect to a . To find a stationary point of U the perturbation must be $O(\delta a^2)$ where

$$\delta U = -\frac{2}{N} (T - \frac{1}{N} \sum a)^T \frac{1}{N} \sum \delta a + \lambda J^T \delta a + O(\delta a^2) \quad (D.5)$$

For this to be true for arbitrary variations, δa , then

$$-\frac{2}{N} T^T \frac{1}{N} \sum + \frac{2}{N} a^T \frac{1}{N} \sum + \lambda J^T = 0 \quad (D.6)$$

and

$$a = A^{-1} C - \frac{\lambda}{2} A^{-1} J \quad (D.7)$$

where

$$A = \frac{1}{N} \sum \frac{1}{N} \sum^T$$

is the covariance matrix of the nearby data with each other and

$$C = \frac{1}{N} \sum T$$

is the vector of covariances between the missing datum and the nearby data. Following Bretherton, et al., to obtain an unbiased estimate when the local spatial mean has not been removed from the data, define a spatial mean \bar{T} as

$$\bar{\mathbf{y}}^T \mathbf{A}^{-1} \mathbf{J} = \bar{\mathbf{T}}^T \mathbf{J}^T \mathbf{A}^{-1} \mathbf{J} \quad (\text{D.8})$$

To see that this is a sensible definition of the mean, look at the simple case where all nearby data have the same variance and have the same covariance with each other and with the missing datum. Then equation D.8 reduces to

$$\frac{1}{M} \bar{\mathbf{y}}^T \mathbf{J} = \bar{\mathbf{T}} \quad (\text{D.8'})$$

which is a simple mean.

Substituting D.8 and D.7 into D.2 gives

$$\bar{\mathbf{T}} = \bar{\mathbf{y}}^T \mathbf{A}^{-1} \mathbf{C} = \frac{\lambda}{2} \bar{\mathbf{T}}^T \mathbf{J}^T \mathbf{A}^{-1} \mathbf{J} \quad (\text{D.9})$$

and eliminating λ using D.6 and D.3 gives

$$\bar{\mathbf{T}} = \bar{\mathbf{T}} + (\bar{\mathbf{y}} - \bar{\mathbf{T}} \mathbf{J})^T \mathbf{A}^{-1} \mathbf{C} \quad (\text{D.10})$$

An expression for the expected square error can be found for this estimate, $\bar{\mathbf{T}}$

$$\text{MSE} = \frac{1}{N} \bar{\mathbf{T}}^T \bar{\mathbf{T}} - \bar{\mathbf{C}}^T \mathbf{A}^{-1} \bar{\mathbf{C}} + \beta^{-1} (1 - \mathbf{J}^T \mathbf{A}^{-1} \mathbf{C})^2 \quad (\text{D.11})$$

where

$$\beta = \mathbf{J}^T \mathbf{A}^{-1} \mathbf{J}$$

and $\frac{1}{N} \bar{\mathbf{T}}^T \bar{\mathbf{T}}$ is simply the variance of $\bar{\mathbf{T}}$.

The image is subdivided into about 10 areas and the covariance matrix A is estimated for all of the functions, ϕ_i , using images from which $\langle T(x) \rangle$ has been removed. The functions are defined by

$$\phi_i = T(x + \delta x, t + \delta t)$$

where

$$\delta x, \delta y = \pm 1 \quad \text{for } \delta t = 0, \pm 0.5 \text{ day}$$

$$\delta x, \delta y = 0 \quad \text{for } \delta t = \pm 1.0 \text{ day}$$

so that nearby data are defined as those data within a 3×3 pixel box centered on the missing datum in the original image or an image within 12 hours of the original, or at the location of the missing datum in an image separated from the original by 24 hours. In practice images at one-day separations were rarely used and the maximum separation for all images used in the composite of an image never exceeded one day. The maximum MSE was set at 30 % of the variance so that even if there were data in any of the allowed locations, the missing datum was not necessarily assigned an interpolated value.

As noted by Bretherton, et al., the stationary point of U will be a maximum under certain conditions and this will be indicated by a negative MSE. This occurs in practice as the limiting case when there are many data very near the missing datum, i.e., when many of the elements of A are nearly identical. This is not a serious problem because then a good estimate of T is simply

$$T = \bar{T}$$

and equation D.8' is used instead. If the 3 x 3 box around the missing datum contains three or more data or contains the only nearby data, the simple mean is computed. Thus equation D.10 is used only when nearby data are scattered in space and time.

APPENDIX E COMPUTING EOF'S USING SVD

Empirical orthogonal functions (EOF's) are a compact way of describing a large or complex data set. Their primary purpose is to reduce the number of degrees of freedom of the data variable so that it can be compared with another variable to determine correlations (Davis, 1976). The variable $D(x,t)$ can be written as a linear combination of functions, $f_i(x)$, $i = 1, N$, where N is the number of spatial points,

$$D = F a \quad (E.1)$$

or

$$\begin{bmatrix} D(x_1, t_j) \\ D(x_2, t_j) \\ \vdots \\ D(x_N, t_j) \end{bmatrix} = \begin{bmatrix} f_1(x_1) & \cdot & \cdot & \cdot & f_N(x_1) \\ f_1(x_2) & & & & f_N(x_2) \\ \vdots & & & & \vdots \\ f_1(x_N) & \cdot & \cdot & \cdot & f_N(x_N) \end{bmatrix} \begin{bmatrix} a_1(t_j) \\ a_2(t_j) \\ \vdots \\ a_N(t_j) \end{bmatrix}$$

where the coefficients, a , are functions only of time. If the functions are chosen to satisfy the orthogonality relationship

$$F^T F = I \quad (E.2)$$

where F^T is the transpose of F , then the variance in the data, D , is divided into modes, i.e.,

$$DD^T = F\alpha\alpha^T F^T = FLF^T \quad (E.3)$$

where L is a diagonal matrix. The separation of the modes arises from the diagonality of L ; this decomposition is possible because DD^T is real and symmetric and F is unitary (see, e.g., Franklin, 1968). To reduce noise in D one wants to describe it with fewer than N functions. If D is approximated by \bar{D} , which uses only M functions ($M < N$), then the M functions which best describe D in the sense that

$$(\bar{D} - D)^T (\bar{D} - D) \text{ is a minimum}$$

are the empirical orthogonal functions which correspond to the largest elements of L (Davis, 1976).

The functions, F , are usually found by solving the eigenvalue problem

$$CF = FL \quad (E.4)$$

where C is the covariance matrix for the data. When the data are uniformly sampled in space and in time the covariance matrix is simply the mean product matrix of the data, D

$$C = DD^T \quad (E.5)$$

and E.4 can be obtained from E.3 by multiplying on the right by F . Alternatively, if E.5 is valid, one can decompose D instead of C using

singular value decomposition (SVD)

$$D = F S H^T \quad (E.6)$$

where

$$H^T H = I \quad (E.7)$$

(Lawson and Hanson, 1974) The matrix, S , is not square if D is not square; in the case $N > T$, where D is an $N \times T$ matrix

$$S = \begin{bmatrix} S' & \\ - & - \\ 0 & \end{bmatrix} \quad (E.8)$$

and S' is diagonal.

The relationship between the SVD and the eigenvalue problem, E.4, can be seen by multiplying E.6 on the right by D^T

$$D D^T = F S H^T H S^T F^T = F S^2 F^T \quad (E.9)$$

which is identical to E.3 if

$$L = S^2 \quad (E.10)$$

so that the relationship between the singular values, s_i , on the diagonal of S and the eigenvalues is

$$f_i = s_i^2 \quad (\text{E.11})$$

The matrix, H , which contains the right singular vectors of D , contains the eigenvectors of a closely-related problem

$$D^T D = H S^2 H^T \quad (\text{E.12})$$

which has the same eigenvectors.

The advantage of SVD is in the number of computations required. The covariance matrix, C , need not be computed and the decomposition takes $O(NT^2)$ operations as compared to the $O(N^3)$ operations for the eigenvalue decomposition. Clearly this is only an advantage if $N > T$.

A drawback of the SVD method is its inability to handle missing data. The covariance matrix can be estimated from the data by averaging data products over all available pairs. No corresponding procedure can be defined for missing data in D . The missing elements must be replaced by an estimate. The data vector at a given time, t_j , can be weighted with the integral weight, n , by simply including it n times in the data matrix, D .

END

FILMED

1-84

DTIC